

UNIVERSITÉ DE GENÈVE
Département de Physique Appliquée

FACULTÉ DES SCIENCES
Professeur Jean-Pierre Wolf

COHERENT CONTROL OF THE VISION PROCESS IN LIVING
ANIMALS

THÈSE

Présentée à la Faculté des sciences de l'Université de Genève
Pour obtenir le grade de Docteur ès science, mention Physique

par
Geoffrey Gaulier

de
France

Thèse N° 5561

GENÈVE
Centre d'Impression de l'Université de Genève
2021

Remerciements

J'écris ces lignes quelques semaines après la soutenance, le stress étant donc déjà bien retombé. Je remercie ainsi d'abord les professeurs Giulio Cerullo et Ursula Roethlisberger, pour avoir évaluer mon travail, et agit en tant qu'expert dans le domaine de du contrôle de l'isomérisation de la rhodopsine.

J'aimerais remercier évidemment Jean-Pierre pour m'avoir accueilli dans le groupe en Master, puis en PhD, cumulant ainsi 6 ans au sein du GAP. Merci d'avoir de m'avoir fait confiance, et d'avoir guider tous ces projets, y inclus ceux qui ne sont pas dans ce manuscript. Tu as toujours su expliquer la physique avec une facilité étonnante.

J'aimerais ensuite remercier Luigi, qui a guidé les expériences au jour le jour, en venant toujours avec une solution innovante. Ce projet n'aurait jamais pu être réalisé sans tes connaissances et ton savoir-faire. Merci également d'avoir su me garder motivé à tout moment, car ce ne fut pas toujours facile.

J'aimerais ensuite remercier toutes les personnes avec qui j'ai interagi au sein du groupe, et particulièrement Michel, qui a su trouver les solutions autre que le scotch ou la méthode rapide. Évidemment Quentin, avec qui j'ai passé des jours, et des jours, et des soirées, en labo. Merci pour le miel aussi ! Aleksa, Luca, qui sont actuellement au labo en train de m'attendre alors que j'écris ces lignes, pour les longues heures passées que l'on y a passé tous ensemble. Une petite pensée pour le filament qui a traversé la table optique ! Cédric et Julien, qui m'ont, chacun à leur tour, appris à aligner, coder, et travailler avec les lasers correctement, au début de ma thèse. Gabriel, avec qui j'ai travaillé mais aussi passé beaucoup de soirée ! Je ne le remercie pas pour m'avoir initié au son de qualité ceci dit, ça couté cher. Les voisins ne te remercient pas non plus. Dmitry, avec qui j'ai travaillé sur les photons intriqués. Thomas également, qui a commencé sa thèse en même temps. Et tous les autres, Malte, Yi-Ping, Tadas, Tessa, Michael, Ugo, Victor et Doyoung !

Merci également aux secrétaires, Isabel, Dragana et Corinne, qui ont géré

la partie administrative. Merci aussi à Jérôme, pour ta disponibilité. Merci aussi à Claudio pour la partie électronique. Merci également à tous ceux qui ne font plus parties du groupe, mais dont j'ai également pu apprendre, en particulier Matteo, Adrien, Denis, Gustavo et Sylvain.

J'aimerais enfin remercier tous les collaborateurs de ce projet, et il y a en a beaucoup ! D'abord Ivan Rodriguez, et Véronique, pour la partie biologique puis Swarnendu, pour les simulations, et Florence, pour son expertise en electroretinogramme. Également Jean-Marc Matter, Pedro Herreira, Hugo Zbinden et Rob Thew, qui font parti du projet Quantum Vision, ainsi que Tania et Marie pour la partie ex-vivo.

Finalement, j'aimerais remercier ma famille, qui a cru en moi depuis le début. Merci aussi à Matthieu, Guillaume, Hellena et Nathalie, qui ont dû compter les femtosecondes pendant que j'expliquais ce projet, et qui m'ont toujours appuyé. Finalement, merci à toi Cleo, for everything.

Résumé

La vision est habituellement considérée comme étant sensible au nombre de photons, mais pas à leur phase respective. Cependant, les expériences réalisées sur le retinal en solution ont montré que la première étape de la vision consiste en une isomérisation très rapide (de l'ordre de 200 fs), qui peut être contrôlée en modifiant la phase des impulsions femtosecondes, et plus spécifiquement dans un régime d'interaction à plusieurs photons. Le lien entre les expériences en solution et les processus biologiques permettant la vision ne sont pas triviaux et n'ont pas été démontrés. Dans le but de réunir ces deux points de vue, j'ai réalisé un système permettant de mesurer les signaux électriques émis par la rétine à partir de l'absorption de lumière femtoseconde. Les expériences ont été réalisées en partie *ex-vivo* (c'est-à-dire sur des rétines extraites de l'oeil), et en partie *in-vivo* (sur des souris anesthésiées).

Sur les rétines *ex-vivo*, j'ai étudié le signal physiologique produit par l'absorption de deux photons dans la rhodopsin, et en particulier l'effet de la durée d'impulsion de l'impulsion femtoseconde, le diamètre du faisceau et son énergie. J'ai mesuré la réponse rétinienne émise à partir d'une expérience du type pompe-sonde, en utilisant une pompe d'excitation visible et une sonde infrarouge.

Dans les souris vivantes, j'ai investigué l'effet d'une impulsion femtoseconde infrarouge, dans laquelle a été introduite une phase en forme de marche d'amplitude pi. La réponse caractéristique obtenue est en bon agrément avec les calculs. Finalement, j'ai mesuré la réponse rétinienne provenant des souris vivantes dans deux expériences: une première dans laquelle j'utilise une impulsion femtoseconde dont la forme temporelle a été modifiée, et une seconde expérience de type pompe-sonde/re-pompe. Les résultats montrent que le signal électrophysiologique est en effet sensible à la phase spectrale, c'est-à-dire à la manipulation de la lumière à l'échelle femtoseconde. Le mécanisme de contrôle repose sur de multiples interactions avec la lumière autour de l'intersection conique, comme le pompe-sonde (interruption de

l’isomérisation) ou pompe-repompe (isomerisation inverse). Cette interprétation des résultats experimentaux est appuyée par des simulations quantiques.

Ensemble, ces observations constituent une démonstration de contrôle cohérent d’une fonction biologique dans un animal vivant, à des niveaux de lumières physiologiques.

Abstract

Vision is usually assumed to be sensitive to the light intensity and spectrum but not to its spectral phase. However, experiments performed on retinal proteins in solution showed that the first step of vision consists in an ultrafast photo-isomerization of the retinal moiety that can be coherently controlled by shaping the phase of femtosecond laser pulses, especially in the multi-photon interaction regime. The link between these experiments in solution and the complex biological process allowing vision is not trivial, and has not been demonstrated. In order to unify the two points of view, I used a system to measure the electrical signals emitted by retina, which was probed using several femtosecond beams.

The experimental part was carried out partly *ex-vivo* (*i.e.*, on extracted retinas), and partly *in-vivo* (*i.e.*, on anesthetized mice).

On *ex-vivo* retinas, I studied the physiological signal produced by the absorption of two infrared photons in rhodopsin, in particular the effect of the pulse duration of the femtosecond pulse, the diameter of the beam and its energy.

In living mice, I investigated the effect of a pi-step in the spectral phase of an infrared femtosecond pulse. The characteristic response is qualitatively in good agreement with the calculations. Finally, I measured the retinal response from living mice upon femtosecond pulse-shaped light excitation and pump-dump/re-pump stimulation. The results show that the electrophysiological signaling is indeed sensitive to the spectral phase, *i.e.*, to the manipulation of the light excitation on a femtosecond time scale. The mechanism relies on multiple interactions with the light pulses close to the conical intersection along the retinal isomerization coordinate, like pump-dump (photo-isomerization interruption) and pump re-pump (reverse isomerization) processes. This interpretation of the experimental results is supported by dynamics simulations.

Combined, our observations constitute a demonstration of coherent control of a biological function in a living animal at physiological light excitation levels.

Contents

Introduction	11
1 General concepts	15
1.1 Non-linear optics	15
1.1.1 Femtosecond laser pulses	15
1.1.2 Time bandwidth product	16
1.1.3 Temporal and spectral phase	18
1.1.4 Pulse shaping	19
1.1.5 Characterization techniques	20
1.1.5.1 Autocorrelation	20
1.1.5.2 Frequency resolved optical gating	22
1.1.6 Compression of pulse duration	23
1.1.6.1 Chromatic dispersion and chirped mirrors . .	23
1.1.6.2 Filament-based pulse compression	23
1.2 The eye and the vision process	24
1.2.1 Anatomy of the eye	25
1.2.2 Difference between human and murine eye	27
1.2.3 The photophysics of vision	30
1.2.4 Electrotoretinogram	36
1.2.5 Genetic modifications of vision photo-receptors	38
2 Experimental techniques and data analysis	40
2.1 Laser Sources	40
2.1.1 Non collinear parametric amplifier	41
2.2 Two-photon vision control set-up	41
2.3 Intra-pulse coherent control	43
2.3.1 Set-up	44
2.3.2 Energy correction	45
2.4 Multipulse coherent control	45
2.4.1 50 fs-pulse pump probe set-up	46
2.4.2 25 fs-pulse pump probe set-up	47

2.5	Detection System	49
2.5.1	Illumination method	49
2.5.2	Animal handling techniques	50
2.5.2.1	<i>Ex-vivo</i> acquisition of electroretinogram	50
2.5.2.2	<i>In-vivo</i> acquisition of electroretinogram	51
2.6	Data analysis	55
3	<i>Ex-vivo</i> experiments	57
3.1	Characterization of two-photon vision	57
3.2	ERG energy, pulse duration and beam diameter dependence upon two-photon absorption	60
4	<i>In-vivo</i> experiments	65
4.1	Light energy response of the retina using an ERG	65
4.2	Two-photon absorption control	69
4.2.1	Two-photon energy dependence	69
4.2.2	Influence of a π -phase step in the spectral phase on the response of rhodopsin	71
4.2.3	Calculation of the influence of the π -phase step upon two-photon absorption	76
4.3	Intra-pulse coherent control of vision	79
4.3.1	Measurement of the pulses used in the experiment	80
4.3.2	Pulse duration dependence	81
4.3.3	Rate equations	84
4.3.4	Results of ab initio simulation	92
4.4	Multi-pulse coherent control of rhodopsin	97
4.4.1	ERG power dependence	98
4.4.2	Multi-pulse coherent control using long pulse on rhodopsin	99
4.4.3	Results of <i>ab initio</i> simulation	100
4.4.4	Multi-pulse coherent control using short pulse on rhodopsin	102
4.5	Coherent control of medium opsin	104
4.5.1	Intra-pulse coherent control	104
Conclusion		106
Appendix		109
References		117

Introduction

The eye is a wonderful organ, designed to see the world, and communicate with the others. The most prominent part of the eye is the retina, where the receptors turns photons into an electrical signal, which, after being processed by the brain, defines the vision process.

The understanding of the visual system has tremendously advanced since the work of Kepler¹. He demonstrated that, unlike previous theory, the eye was receiving light, instead of emitting it to scan the object surrounding us. He explained the formation of the image on the light-sensor at the back of the eye called the retina. Later on, it was discovered that the retina encompasses multiple layers of cells, from the light-sensitive, called rods and cones, to the ganglion cells, which compose the optical nerve, transmitting information to the brain. Rods are the detectors of the retina optimized for dim light, while the vision in bright and colorful daylight requires cones.

The key-component of this thesis lies in the sensitive part of the rods and cones. Inside these photoreceptors are proteins called opsins, and embedded in the middle of them, lies the retinal. This protein, a form of vitamin A, initiates the first step of a long biological chain which results in vision. The measurement of the speed of this first step is directly associated with the advent of femtosecond lasers.

The theory for laser, such as absorption, spontaneous and stimulated emission, was set by A. Einstein in 1917². However, it was only in 1960 that the first laser was invented, using a ruby crystal as the gain medium, and pumped by a high power flash lamp.

Since its introduction sixty years ago, the laser has been developed and perfected for reaching high energy and femtosecond pulse duration. In the mid-1980s, the CPA (Chirped Pulse Amplification) technique was invented by G. Mourou and D. Strickland³, for which they won the Nobel Prize in 2018. As a result, they obtain short (<100 fs), high energy pulses (mJ per pulses), suitable for non-linear effects. The latter allows for wavelength-tuning, pulse duration reduction, and white-light generation among others, which are use-

ful for probing vision.

It was demonstrated twenty years ago that the absorption of a photon by the retinal changes its conformation in less than 200 femtoseconds⁴. More recently, the complete isomerization of the retinal was time-resolved⁵. Both these experiments, among others, were based on the transient absorption of rhodopsin, the opsin located inside rods. In these experiments, a first femtosecond laser pumps the rhodopsin from its ground state to an excited state, and a broadband light pulse probes the absorption in the visible at several delays after the pump pulse. The study of the transient spectrum of the broadband pulse at different delays makes it possible to collect information on the energy states of the rhodopsin. It was also demonstrated during the last decade that it is possible to modulate the isomerization efficiency with one temporally shaped femtosecond pulse only⁶. These measurements were performed on molecules in solution.

One study⁷ revealed that channelrhodopsin, a specific type of opsin and a key tool in optogenetics, could be controlled by two-photon absorption in a living brain tissue. This extremely interesting result on channelrhodopsin however bears some difference with the case of vision. In fact, rhodopsin needs to be coupled to a G-protein⁸. Channelrhodopsin is a direct light-gated channel, and is therefore more robust for optogenetics, but still far from a vision study.

My work reports the achievement of the first coherent control of the vision process in living mice. The manuscript is structures in fours chapters.

In the first chapter, I give a general introduction of the background concepts of non-linear optics and of the vision process. I pay a particular attention to the characterization of femtosecond pulses, including the measurement of its spectrum and spectral phase and their relationship with the pulse duration. I also explain how to modify them, using different techniques, such as pulse shaping. In the second part, I describe the anatomy of the eye and the photophysics of vision. In particular, I explain the potential energy surfaces of rhodopsin (Figure 1), and the associated wavepacket dynamics. This explanation naturally leads to the description of the electroretinogram, the main experimental observable used in this work.

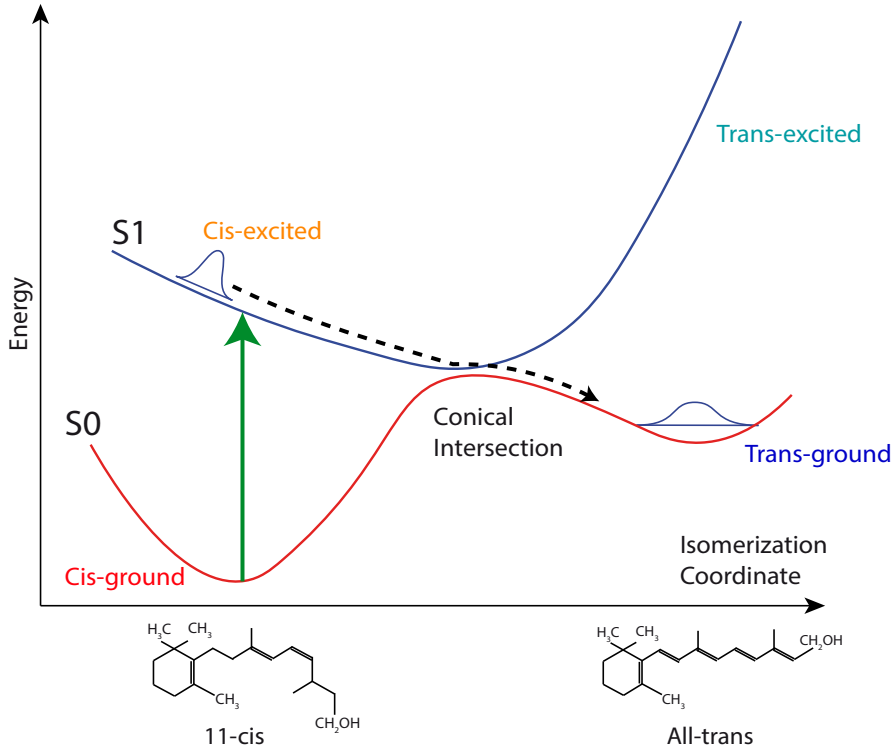


Figure 1: Sketch of the energy level of rhodopsin.

In the second chapter, I present the laser system used during this study, and describe the experimental set-up and detail the different experiments I set-up and performed. The first experiment is a two-photon absorption experiment with photons outside the linear absorption band of rhodopsin. For this, I assessed the electroretinogram measured upon two-photon absorption. Then, the spectral phase of the pulse leading to two-photon absorption was modified and the effect on vision monitored via the same pulse shaping system used in the intra-pulse coherent control measurements. The second experiment consists in an intra-pulse coherent control approach, where a 535 nm femtosecond pulse illuminates the retina of anaesthetized mice. The pulse is chirped both positively and negatively, using a pulse shaper in a zero-dispersion 4f-line, while keeping the energy of each pulse constant. The last experiment is a pump-dump/re-pump experiment, where a quasi Fourier transformed 535 nm

pulse excites the rhodopsin, and an 800 nm pulse interacts on an ultrafast time-scale with the molecule in its excited state by dumping the rhodopsin, via different processes, to avoid the landing on the isomerized configuration and hence the vision process. Finally, the complete procedure regarding the anaesthesia of the mice, the detection of the retinal signal, both *ex-vivo* (*i.e.*, on extracted retinas) and *in-vivo* (*i.e.*, on anesthetized mice) is explained.

I present in the third chapter the results obtained *ex-vivo*, while the results obtained *in-vivo* are displayed in the last chapter.

In *ex-vivo* experiments, I addressed infrared vision using two-photon absorption, more precisely using a 960 nm femtosecond pulse. I could demonstrate that the vision from the retina can indeed be triggered upon two-photon absorption and that no damage was induced at these intensity levels. I specifically studied the influence of energy, pulse duration and beam size on the electroretinogram upon infrared femtosecond pulse.

In living mice, I went a step further compared to the experiments carried out *ex-vivo*. In the first part of the chapter, I investigated the effect of a pi-step in the spectral phase of an infrared femtosecond pulse, and observed the characteristic response that is observed in molecular dyes. This is also in agreement with calculations. In the second set of experiments, I observed that a longer pulse decreases the retinal response, despite constant pulse energy, in the single photon absorption regime. The mechanism underlying these observations is explained as follows. After excitation to the S₁ state, the rhodopsin either undergoes through a stimulated emission process or absorbs a photon after crossing the conical intersection and returns to its fundamental state. I developed an *ad hoc* rate equation model to study the effect of intensity, the quantum yield and the dynamics of the system. This interpretation used a pump-dump/re-pump experiment, with a 535 nm pump and a 800 nm pulse, using long and short pulses (compared to the dynamic of the isomerization). This experiment demonstrates that excited rhodopsin can indeed be forced back to the ground state via stimulated emission or re-absorption in the trans-ground state (reverse isomerization). Both intra-pulse and multi-pulse experiments have been confirmed by *ab-initio* calculations from the group of U. Roethlisberger at EPFL. I also applied the experimental protocol to the medium opsin, demonstrating that control is possible in multiple photoreceptors.

Chapter 1

General concepts

In this chapter, we introduce concepts useful to understand the work performed during this thesis. In the first section, dedicated to optics, we will introduce the femtosecond laser and how its temporal profile is tailored to control the isomerization of the rhodopsin, by pulse shaping or modification of pulse duration by filamentation processes. We describe the characteristics of the pulses amplitude and phase in time and frequency space, as well as optical parametric amplification, both subjects being widely used along this work. The second section, which is focused on biology, describes how the vision process works, and how, from the light being transmitted and focused through the eye, it is absorbed by retina photoreceptors and generates a measurable electrical signal.

1.1 Non-linear optics

The only light-dependent step of the vision process is the ultrafast isomerization of rhodopsin, happening at the femtosecond scale⁵. The most adapted tool for studying this process is therefore time-resolved spectroscopy with femtosecond resolution. We will describe in this section basic concepts of ultrafast laser pulses, from their generation to their measurement, and how to tailor them to our needs to study the vision process.

1.1.1 Femtosecond laser pulses

We use a chirped pulse amplified (CPA) system composed of an oscillator, a pulse stretcher, a regenerative amplifier and a pulse compressor (Coherent Astrella). The oscillator uses a Titanium doped Sapphire crystal (Ti:Sa), with a Kerr-lens mode-locked cavity. 800 nm pulses are generated with a repetition

rate in the 100 MHz range, with less than 20 femtosecond pulse duration. To amplify these pulses, a regenerative amplifier is used: a nanosecond pump laser creates the population inversion inside a second Titanium:Sapphire crystal in a cavity. The oscillator pulses are directed through the cavity and are amplified by stimulated emission. However, at these peak intensities and repetition rate, the crystal would get damaged instantaneously. Therefore, a stretcher elongates the pulses to the nanosecond scale, and Pockel cells are used to control the number of round trips a pulse can do inside the regenerative amplifier cavity (Figure 1.1). Each passage in the crystal corresponds to an amplification of the pulse. This in turn entails a decrease of the repetition rate to the KHz level. When the energy is high enough, the pulse is directed through a compressor, to obtain a high energy, low pulse duration beam. However, the repetition rate is reduced to the kHz regime.

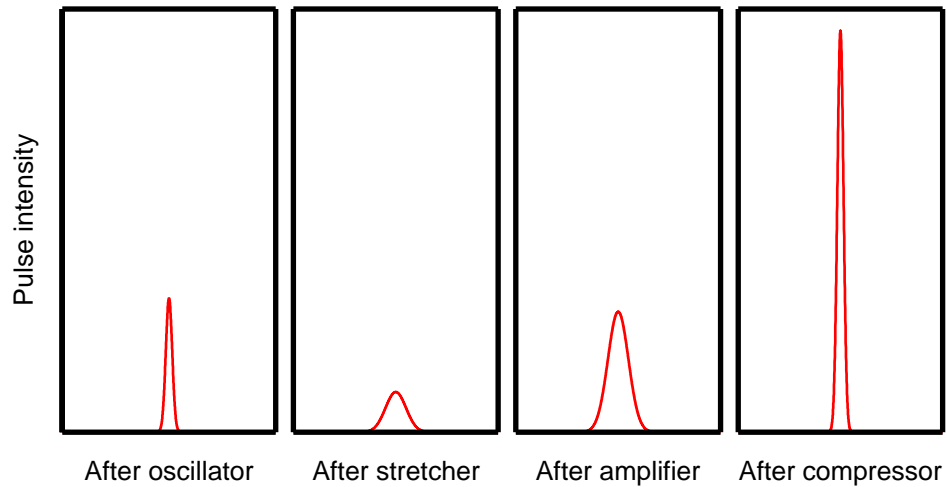


Figure 1.1: Sketch of the pulse as a function of time after different component of the CPA system

1.1.2 Time bandwidth product

To obtain a femtosecond pulse duration, the beam must support a certain bandwidth. A laser pulse of a fixed duration is characterized by a minimum frequency bandwidth due to the fact that these quantities are related via a Fourier transform. We derive here the relationship between bandwidth and pulse duration for Gaussian pulses.

The intensity of the simplest Gaussian pulse is defined with respect to time is:

$$I(t) = I_0 e^{-\alpha t^2} \quad (1.1)$$

Therefore, the time for any value of the Gaussian is defined as:

$$t = \sqrt{\frac{1}{\alpha} \ln \left(\frac{I_0}{I(t)} \right)} \quad (1.2)$$

As the Gaussian is symmetric, and the FWHM is taken at half the value of the maximum (i.e., $I(t) = 0.5I_0$), we obtain:

$$\Delta t = \text{FWHM}_t = 2\sqrt{\frac{1}{\alpha} \ln(2)} \quad (1.3)$$

The Fourier transform of the Gaussian pulse is:

$$I(\omega) = \frac{1}{2\pi} \int_{-\infty}^{\infty} I(t) e^{-i\omega t} dt = \frac{I_0}{\sqrt{2\alpha}} e^{-\frac{\omega^2}{4\alpha}} \quad (1.4)$$

The same calculations gives

$$\omega = \sqrt{\frac{1}{4\alpha} \ln \left(\frac{I_0}{\sqrt{2\alpha} I(\omega)} \right)} \quad (1.5)$$

At FWHM (i.e. $I(\omega) = 0.5 \frac{I_0}{\sqrt{2\alpha}}$), we obtain:

$$\Delta\omega = \text{FWHM}_w = 2\sqrt{4\alpha \ln(2)} \quad (1.6)$$

As $\omega = 2\pi\nu$, $\Delta\omega = 2\pi\Delta\nu$. Therefore:

$$\Delta t \Delta \nu = 2\sqrt{\frac{1}{\alpha} \ln(2)} \cdot \frac{1}{2\pi} \cdot \sqrt{4\alpha \ln(2)} \quad (1.7)$$

$$\Delta t \Delta \nu = \frac{2 \ln(2)}{\pi} = 0.441 \quad (1.8)$$

The last equation is the time bandwidth product for a Gaussian pulse. To obtain the same relationship as a function of the wavelength $\Delta t \Delta \lambda$, we use the relation $\lambda\nu = c$, which gives $\frac{d\nu}{d\lambda} = \frac{-c}{\lambda^2}$. Therefore:

$$\Delta t \Delta \lambda = \frac{2 \ln(2) \lambda^2}{\pi c} \quad (1.9)$$

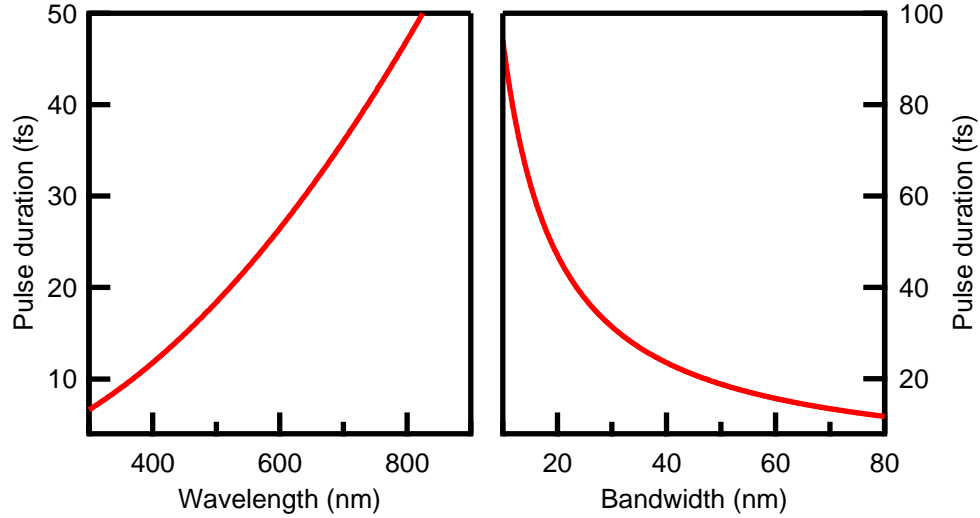


Figure 1.2: Left: Pulse duration vs wavelength, for a bandwidth of 20 nm. Right: Pulse duration vs bandwidth, for a central wavelength of 800 nm.

1.1.3 Temporal and spectral phase

The Equation 1.9 sets the lower limit of the pulse duration corresponding to the Fourier transform-limited pulse. The different frequency components arrive at the same time, and have zero relative phase. By applying chromatic dispersion, the pulse duration increases, and this effect is represented in the electric field by the spectral phase.

The electric field can be defined in either time-domain or frequency domain:

$$E(t) = \int_{-\infty}^{\infty} E(\omega) e^{i\omega t} d\omega = A(t) e^{i\phi(t)} \quad (1.10)$$

$$E(\omega) = \frac{1}{2\pi} \int_{-\infty}^{\infty} E(t) e^{-i\omega t} dt = A(\omega) e^{i\psi(\omega)} \quad (1.11)$$

Where $\phi(t)$ and $\psi(\omega)$ are respectively the temporal and spectral phase of the electric field.

The instantaneous frequency is defined as:

$$\omega(t) = \omega_0 - \frac{d\phi(t)}{dt} \quad (1.12)$$

Where $\omega(t)$ is the instantaneous frequency, and ω_0 the central frequency of the pulse, leading to new frequencies in the spectrum if the phase varies with t.

The spectral phase is often expressed with its corresponding Taylor expansion:

$$\psi(\omega) = \psi_0 + \psi_1 \frac{(\omega - \omega_0)}{1!} + \psi_2 \frac{(\omega - \omega_0)^2}{2!} + \dots = \sum_{n=0}^{\infty} \psi_n \frac{(\omega - \omega_0)^n}{n!} \quad (1.13)$$

Where

- The first term, $\psi_0 = \psi(\omega_0)$ is the absolute phase between the carrier and the envelope of the electric field. As in this work we consider pulses of several optical cycles, this term is not relevant.
- The second term, $\psi_1 = \left. \frac{d\psi(\omega)}{d\omega} \right|_{\omega_0}$, is the group delay. It's measured in femtosecond, and correspond to the displacement of the pulse in time.
- The third term, $\psi_2 = \left. \frac{d^2\psi(\omega)}{d\omega^2} \right|_{\omega_0}$, is the derivative of the group delay. It is the group delay dispersion (GDD). It is measured in fs^2/rad .

This last term can be associated with a linear "chirp", meaning the rate of change of the instantaneous frequency is linear.

1.1.4 Pulse shaping

Pulse shaping is a technique used to modify the spectral amplitude and phase of an electric field, changing its profile in the time-domain.

As the response time of any electronic device is hardly below the nanosecond regime, an optical modulator intensity cannot modify electric fields in the time-domain. Pulse shaping consists of applying a time-delay to the different frequency components of the beam⁹.

The standard 4f optical setup of pulse shaping is displayed in the Figure 1.3. The wavelength components of the pulse are dispersed spatially by a diffraction grating, and collimated using cylindrical optics. The recombination is performed by the symmetric reverse optical system, first the cylindrical optic and last the diffraction grating.

A spatial light modulator (SLM) is aligned in a 4f-line at the Fourier Plane (FP), i.e. at the focal plane of the cylindrical optics. Different technology exists to build a SLM, such as liquid crystal modulators, or MEMS mirror

arrays^{10;11}.

Liquids crystals used in SLM use anisotropic elongated crystals. The orientation of the crystals can be controlled by an electric field. Therefore, the phase acquired by the frequency component of the pulse are controlled using transparent electrode in Indium Tin Oxide.

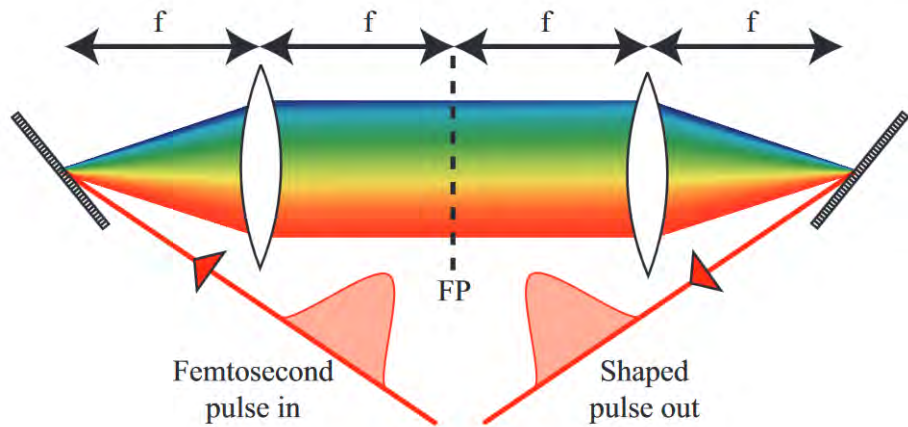


Figure 1.3: Spatial light modulator inside a 4f-line, from Monmayrant et al.¹²

1.1.5 Characterization techniques

The autocorrelation is based on a non-linear interaction between the pulse and itself. It is used daily to retrieve the intensity profile in the time domain. Other techniques, such as the FROG (Frequency Resolved Optical Gating), developed by Trebino's group¹³ measures the phase and the spectrum of the pulse, which cannot be retrieved by autocorrelation, due to different temporal shapes inducing the same autocorrelation traces.

1.1.5.1 Autocorrelation

The simplest device used to measure a femtosecond pulse is a second harmonic generation (SHG) autocorrelator. The pulse is split in two parts, and recombined on a non-linear crystal in a non-collinear way. A mechanical delay changes the arm length difference. SHG is performed for both pulses, but the process of sum frequency generation generates a third pulse in the middle for momentum conservation (Figure 1.4) at zero optical delay between the two arms.

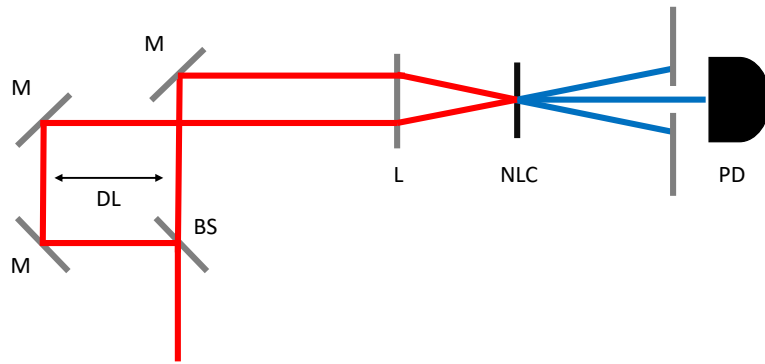


Figure 1.4: Schematic of an second harmonic generation autocorrelator.
BS: Beamsplitter, M: Mirror, L: Lens, DL: Delay Line, NLC: Non-Linear Crystal, PD: Photodiode.

The measure of the sum frequency generation (SFG) pulse as a function of the optical delay between the arms is a convolution of two Gaussian, and is given by the Equation 1.14.

$$S_{PD}(\tau) \propto \int_{-\infty}^{\infty} I(t)I(t - \tau)dt \quad (1.14)$$

Let's consider a Gaussian input pulse with a FWHM τ . The convolution of a Gaussian with itself is a Gaussian with a FWHM $\sqrt{2}\tau$. Therefore, the pulse duration of a Gaussian input pulse is easily retrieved.

This technique has a few drawbacks:

- Different temporal shapes may result in the same autocorrelation curve. Therefore, some assumptions have to be made on the input temporal shape, i.e. using Gaussian beams.
- For very short pulse ($\Delta t < 50$ fs), the GDD induced by the crystal itself is becoming non negligible, and elongates the pulses, increasing the actual pulse duration of the input pulse.
- It is not suitable for UV pulses, as direct second harmonic generation of UV pulses is experimentally hard because of the lack of suitable materials. One should therefore use other second non-linear order processes like difference frequency generation.
- The direction of time cannot be retrieved. Indeed, a change of variable $t' = t + \tau$ show that $S_{PD}(\tau) = S_{PD}(-\tau)$. Therefore, this technique cannot distinguish for instance between a positive and a negative chirp.

- The spectral phase and the spectrum of the input pulse cannot be retrieved.

1.1.5.2 Frequency resolved optical gating

The FROG technique is an extension of the autocorrelation. The FROG uses the autocorrelation scheme of the Figure 1.4. However, the measurement is performed by a spectrometer. Therefore, a three-dimensional graph of the signal as a function of the wavelength and the optical delay is obtained. An algorithm¹³ is used to retrieve the spectral phase and the corresponding spectrum. These are sufficient to calculate the electric field. Any arbitrary temporal input shape can be used.

However, the inherent drawbacks of the SHG process, such as the complexity of generating SHG of UV pulses, and the lack of time direction cannot be avoided. One would require either to interact with an already known pulse using a χ^2 process, or one would require a χ^3 process, such as third harmonic generation, self diffraction, or polarization gating process, which would decrease the sensitivity of the measurement.

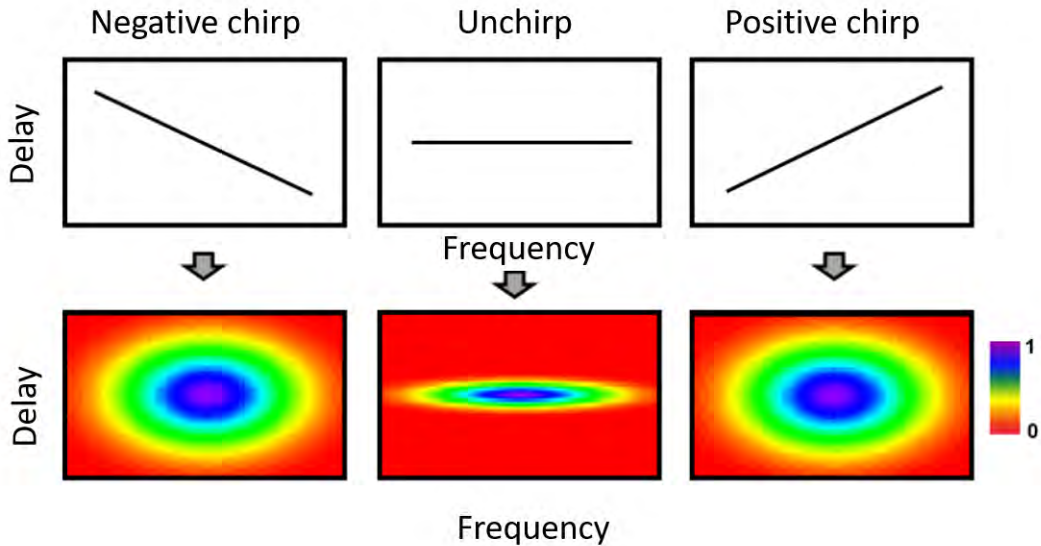


Figure 1.5: Second Harmonic Generation FROG. Phase and spectrum are retrieved, but positive and negative chirp are identical. Figure adapted from Trebino's course¹⁴.

For sufficiently chirped pulses, it is possible to retrieve the direction of time by using any transparent media which add a positive GDD. Indeed, a negatively

chirped input pulse would see its pulse duration decreased, while a positively chirped pulse would see its pulse duration increased.

1.1.6 Compression of pulse duration

1.1.6.1 Chromatic dispersion and chirped mirrors

Pulses acquire positive chirp (longer wavelengths come first) in most transparent media, due to chromatic dispersion (*i.e.*, refractive index is wavelength dependent), and therefore increase their pulse duration.

However it is possible to apply negative GDD, to compensate a positive chirp, with either pulse shaping technique, compressors or chirped mirror. The latter use a spatial variation of different thickness dielectric reflective layer. The interference pattern resulting of the mixture between the two can result in negative GDD, and can force the pulse to return to its transform limited pulse duration.

1.1.6.2 Filament-based pulse compression

The isomerization of rhodopsin is achieved under 200 fs (see subsection 1.2.3). Therefore shorter pulses are needed to measure and study it. As described in the subsection 1.1.2 and subsection 1.1.4, a decrease of a pulse duration can be achieved if three basic principles are followed:

1. The GDD of the pulse is compensated.
2. The bandwidth is increased.
3. The whole spectrum is coherent.

The first requirement can easily be reached with either chirped mirror for positive GDD, or by any transparent media for negative GDD. The second requirement often relies on non-linear interaction. Self phase modulation (a $\chi^{(3)}$ process) generates, via the temporal Kerr-effect, more optical bandwidth. The third requirement is fulfilled if the broadening process is coherent.

The filamentation technique can be used to generate the intensity required for self phase modulation.

The non-linear refractive index of a medium is proportional to the intensity of light:

$$n(I) = n_0 + n_2 I(t) \quad (1.15)$$

Where $n(I)$ is the refractive index, n_0 the refractive index for linear propagation, and n_2 the non-linear refractive index.

Self-focusing is obtained for pulses with high intensity. As the refractive index increases with intensity it becomes larger in the center of the beam than on the edges. This distorts the wavefront, and acts like a lens (Figure 1.6). This effect competes with the natural diffraction. If the pulse power is larger than a critical power (about 6 GW in air¹⁵), self-focusing overcomes the diffraction and the beam size drastically reduces, until the intensity is high enough to ionize the air by multi-photon or tunnel ionization. The latter process generates plasma, which has a defocusing effect. Therefore, self-focusing and plasma generation enter a balance which creates a filament (Figure 1.6). The intensity reached during the filamentation process allows self phase modulation, which creates more optical bandwidth.

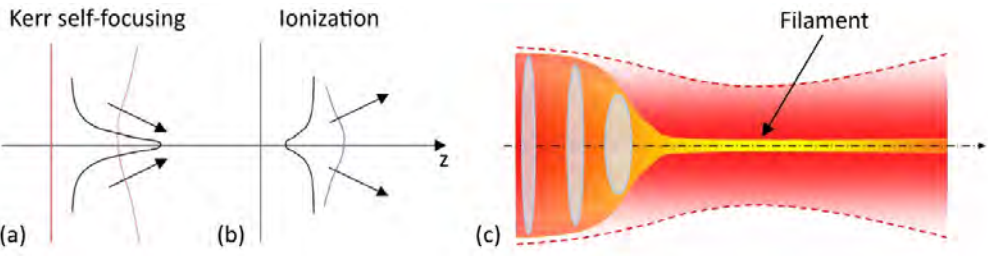


Figure 1.6: (a)- Kerr self focusing, increasing the intensity. (b)- Defocusing from the plasma generated from multi-photon ionization. (c)- The dynamic between plasma generation and Kerr effect generates a filament. Figure from Mitryukovskiy¹⁶.

Pulse compression is needed after the spectral broadening by filamentation. Chirp mirrors assisted by a SHG frog measurement allows for recompression of the pulse, as low as sub-10 fs¹⁷. This technique was used in this work for an easy way of obtaining 10 fs pulses (see subsection 2.4.2).

1.2 The eye and the vision process

We describe in this section how the eye, and more specifically how a mouse eye, focuses light and absorbs a photon, generating a nerve impulse to the brain.

1.2.1 Anatomy of the eye

An eye is composed of a cornea, a pupil, a crystalline lens, a vitreous humour and a retina (Figure 1.7).

The cornea-crystalline lens form a two-lens system. The light is first focused by the cornea, and then by the crystalline lens. It propagates in the vitreous humour, and forms an image on the retina.

The iris is an aperture that can be changed, which blocks the light from illuminating the retina. This is one of the features that allows the eye to work in completely different regimes of light intensity.

To focus the light correctly on the retina, the crystalline's curvature can be modified by the ciliary muscle.

The retina itself consists of a set of cells which generate an electrical impulse encoding the visual information which travels through the optical nerve. The nervous signal is then decoded through a complex series of steps by the brain to form the time series of images we associate with the vision process.

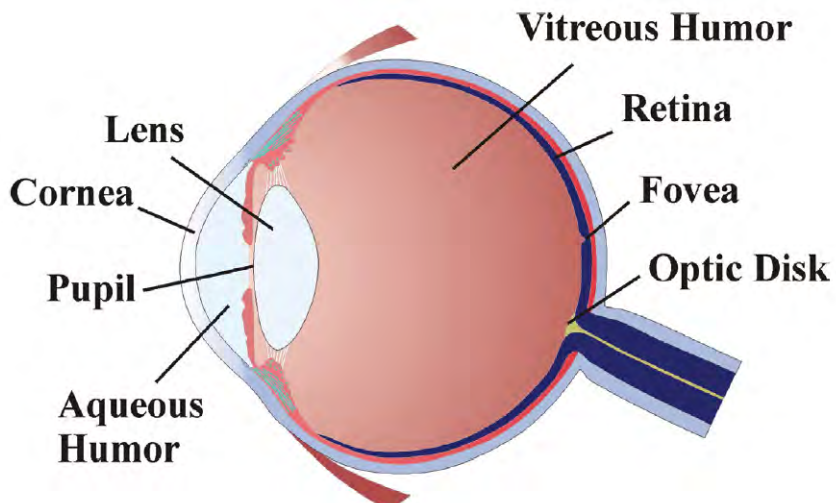


Figure 1.7: Anatomy of an human eye, from Mauser¹⁸.

The retina is organized in three cellular layers: the photoreceptor cells, the bipolar cells and the ganglion cells (Figure 1.8). Photoreceptor cells are classified in two categories: rods and cones. Rods are very sensitive to visible light, and are mainly used for night or dim light vision (scotopic vision). The cones have different absorption spectra, and are used for day vision (photopic vision). In human, three types of cones co-exist: S-, M-, and L-cones, in which the absorption is centred respectively at 420, 530 and 560 nm. Rods are

instead sensible mostly around 500 nm due to the presence of a high density concentration of a single photosensitive membrane complex, rhodopsin. Cones are mostly concentrated in the center of the retina (called the fovea), while rods are more or less homogeneously spread out in the retina, except in the fovea (Figure 1.9). This configuration improves acuity in the fovea (*i.e.*, the capacity to distinguish between two objects) and sensitivity elsewhere.

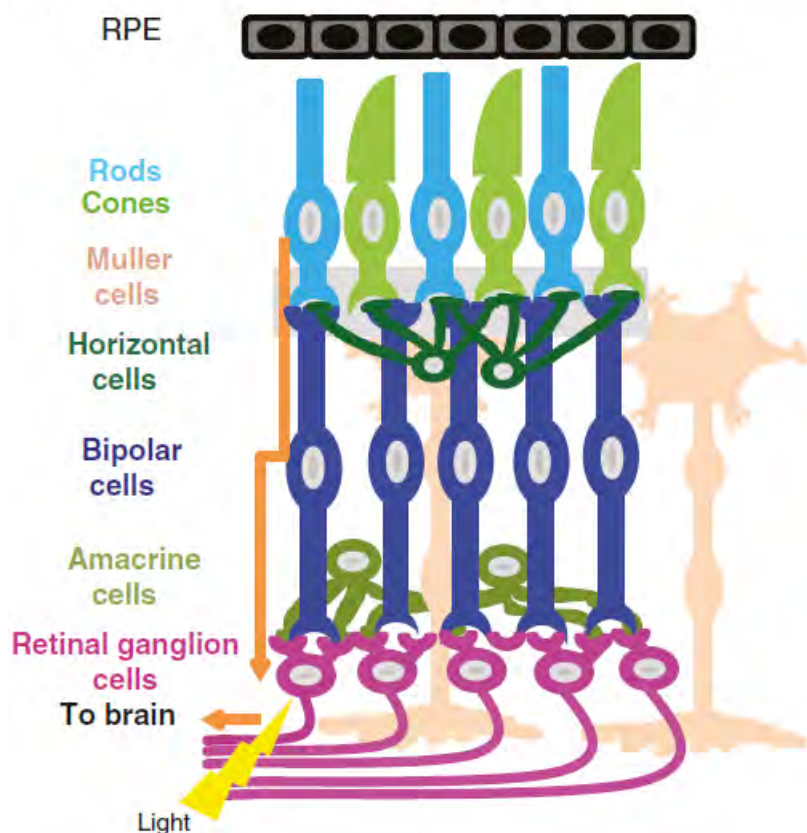


Figure 1.8: Layer of the retina, adapted from Van Gelder et al.¹⁹. RPE: Retinal pigment epithelium

Photoreceptors are connected to the bipolar cells. To increase sensitivity, multiple photoreceptors can be connected to one bipolar cell via the horizontal cells. However, to increase acuity (*i.e.*, in the fovea), the photoreceptors are often connected to one single bipolar cell. The bipolar cells are themselves connected to the ganglion cells²⁰. Together, the ganglion cells form the optical nerves.

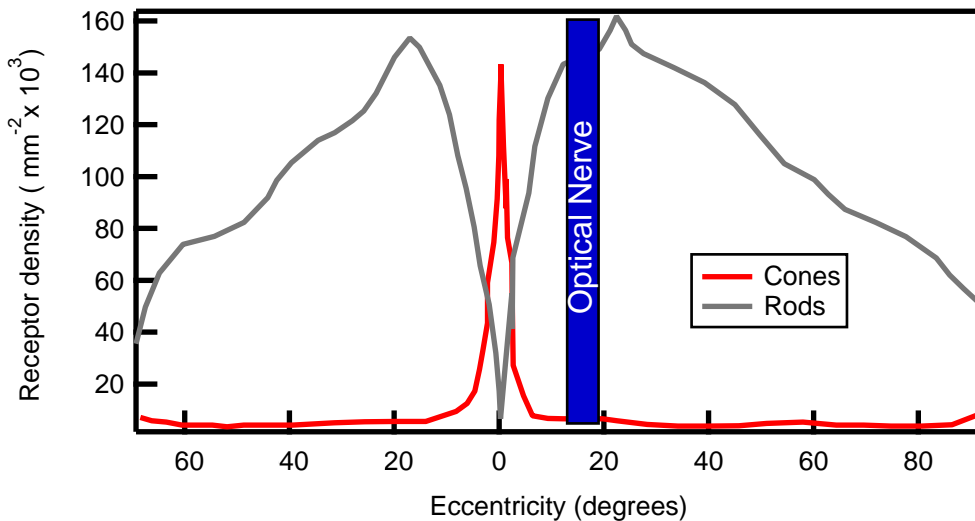


Figure 1.9: Photoreceptor density as a function of the eccentricity, data from Purves et al.²¹. The density of cones is high in the fovea, but is almost null in the rest of the retina, while the rods have the highest concentration at non-zero eccentricity. The density of photoreceptors drops to zero at the optical nerve position.

The retinal pigment epithelium (RPE), located at the back of the eye, between the choroid and the retina, has multiple functions. Its blackness helps avoiding light reflection back to the photoreceptors. The RPE also nourishes the retina, giving access to ions (necessary to the signal firing described in subsection 1.2.4) and regeneration of the retinal for the visual cycle²².

1.2.2 Difference between human and murine eye

The eye of a mouse is smaller (approximatively 3 mm diameter) compared to a human eye (approximatively 24 mm diameter)²³. The lens occupies a larger fraction of the eye of a mouse than a human (Figure 1.10).

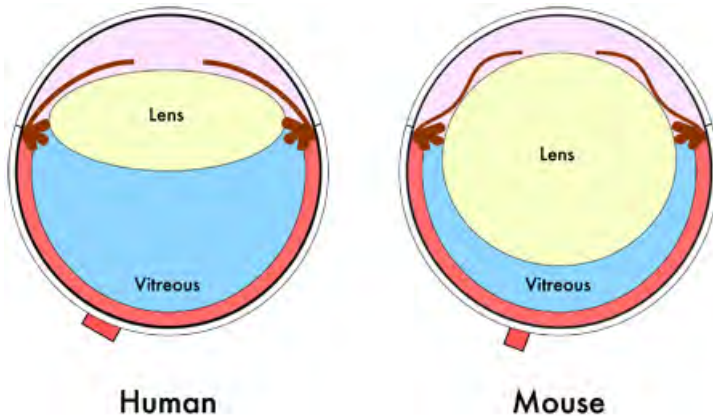


Figure 1.10: Left: Schematic of a human eye, right: schematic of a mouse eye, from Skeie et al.²⁴.

Regarding the composition of the retina, the mouse photoreceptor cells are mainly rods²² with the absorption spectrum centred at 500 nm, and two types of cones, namely S- and M-cones, which absorb at 370 nm and 535 nm, respectively (Figure 1.11).

Contrary to the human, the mouse does not have a fovea, where all the cones are specifically concentrated²⁵. The mouse retina is similar to the peripheral part of the human eye, where one can easily distinguish motion, but without perception of details.

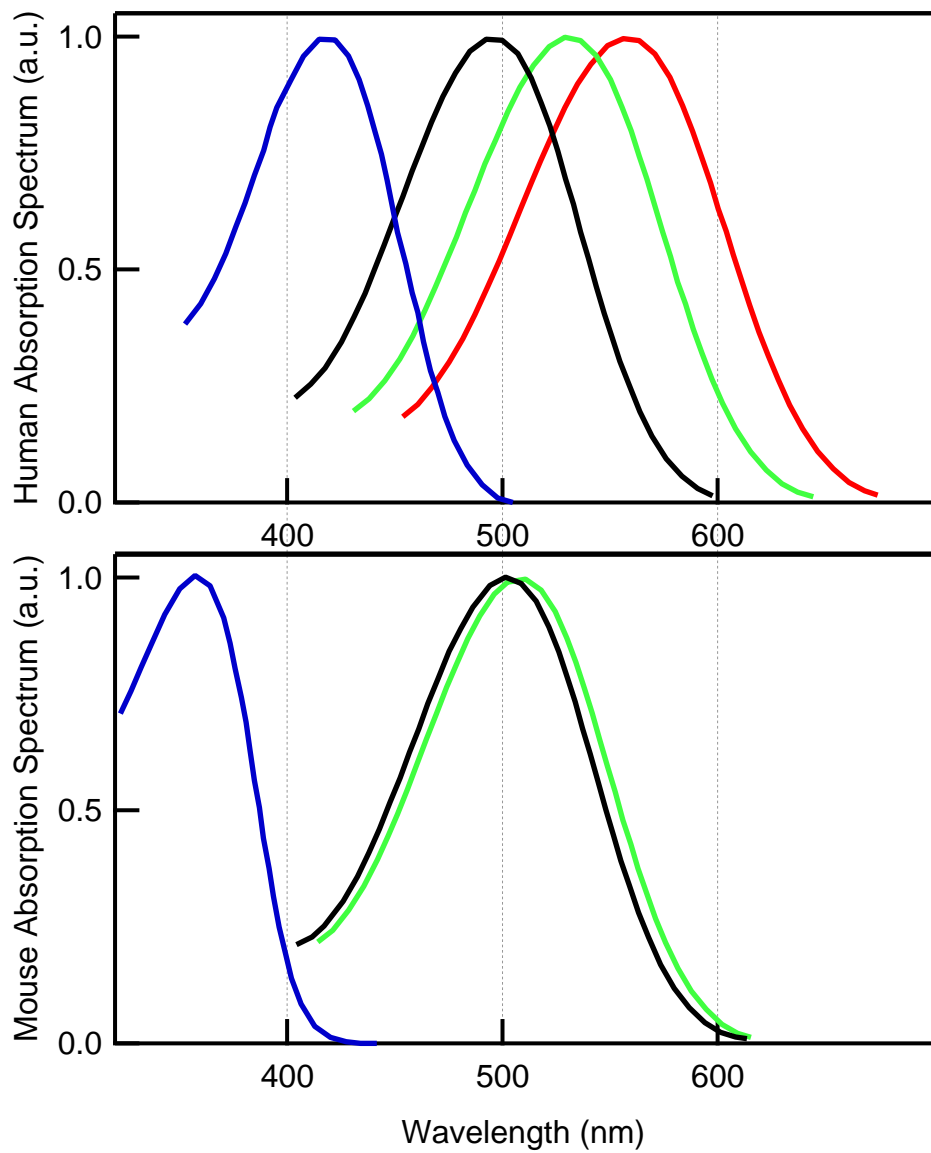


Figure 1.11: Top: Absorption spectrum of photoreceptors in a human eye, bottom: Absorption spectrum of photoreceptors in a mouse eye, data from Kojima et al.²⁶. The S-, M- and L-cones absorption spectra correspond respectively to the blue, red and green curve. The rhodopsin absorption spectrum is represented by the black curve.

1.2.3 The photophysics of vision

We will concentrate here on the rod signalling, as it is the most studied (due to the fragility and rarity of the cones in mouse retina²²). However, the cones pathway is similar²⁷. A schematic view of a rod is shown in Figure 1.12. The outer segment part of the rod contains many disks, which themselves contain the embedded rhodopsin proteins. The rest of the rod cell contains the nucleus and other organelles necessary for its survivability. The synaptic region fires neurotransmitters. This process is discussed in the subsection 1.2.4.

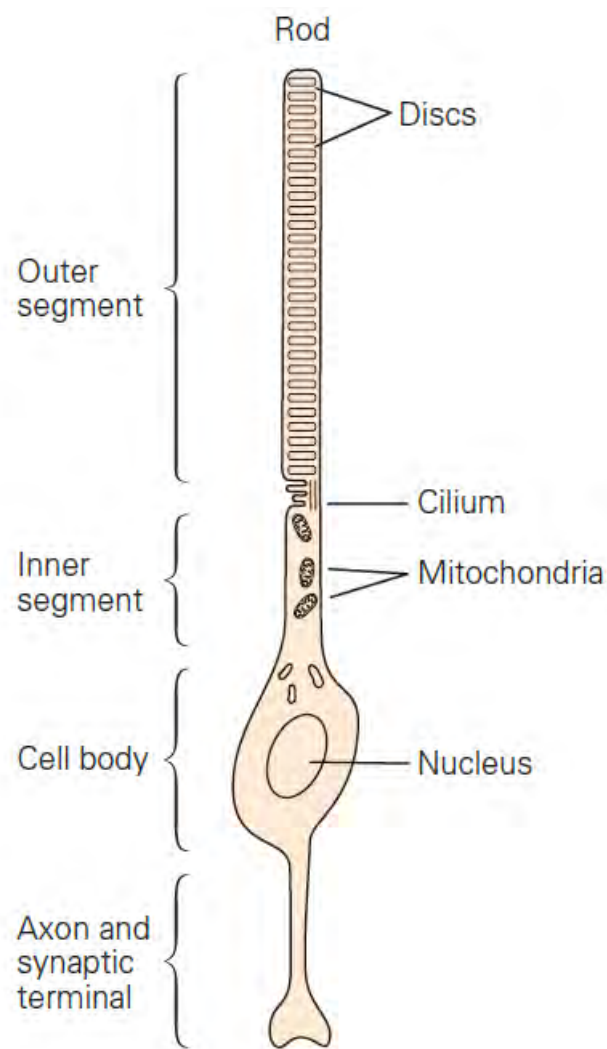


Figure 1.12: Structure of a rod, adapted from Meister et al.²⁸

Inside rhodopsin is located the retinal moiety, the photo-sensitive part of the protein. A photon is absorbed by the retinal. It undergoes a conformation change: from an 11-cis to an all-trans configuration, meaning the elbow at the 11th carbon unfolds in a straight line. We define here the energy levels of the retinal as follow:

- Cis-ground corresponds to the S₀ ground state, the retinal being in the 11-cis-state (initial conformation).
- Cis-excited corresponds to the S₁ excited state, the retinal being in the 11-cis-state (initial conformation).
- Trans-ground corresponds to the S₀ ground state, the retinal being in the all-trans state (final conformation).
- Trans-excited corresponds to the S₁ excited state, the retinal being in the all-trans state (final conformation).

The retinal follows then the following pathway, after photon absorption:

1. Retinal is promoted from cis-ground to-cis excited
2. The dihedral angle changes progressively at the femtosecond scale, until it reaches the conical intersection, in 80 fs.
3. With a yield of 37% , the retinal returns to the cis-ground²⁹.
4. For the other 63 %, the retinal isomerizes into the all-trans ground state in 200 fs (from the cis-excited state).

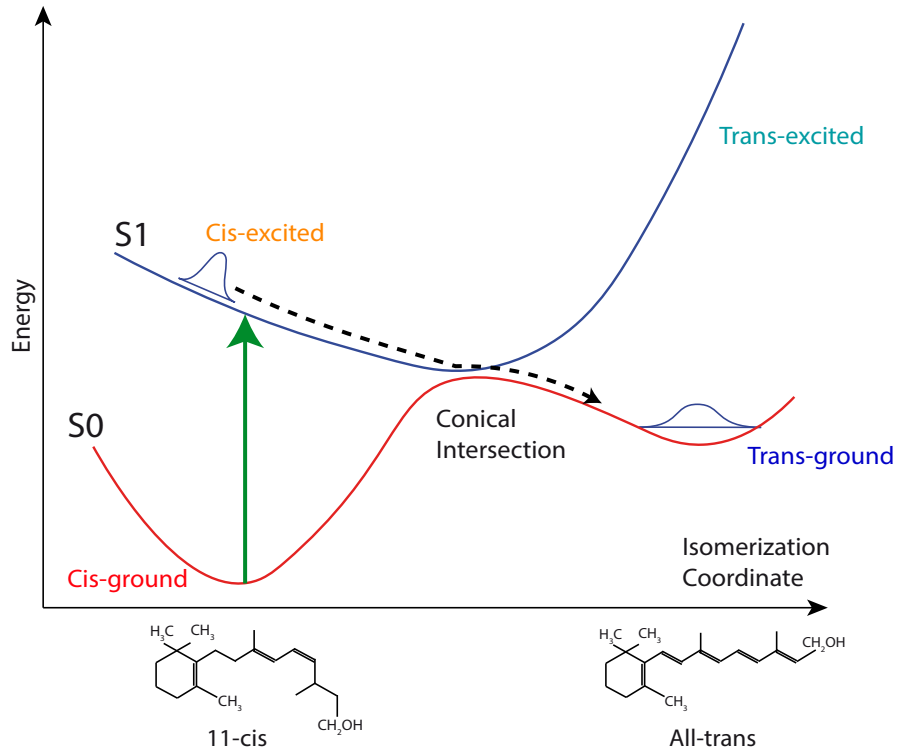


Figure 1.13: Sketch of the energy level of the retinal in rhodopsin.

This pathway, described in the Figure 1.13, has been first demonstrated *in vitro* by Schoenlein et al.^{4;30;31} using transient absorption spectroscopy. More recently Polli et al.⁵ and Schnedermann et al.³² brought more evidence regarding the dynamics at the conical intersection, which is crossed after 80 fs, and the retinal reaching the all-trans ground state after approximatively 200 fs (Figure 1.14). Briefly, they excite the retinal with a 500 nm pump beam. A white-light is delayed and illuminates the sample after the pump. The spectrum of the white light is analyzed at varying delay, with and without pump. During the first 80 fs, the white light stimulates the emission (stimulated emission in Figure 1.15). After 80 fs, the white light is absorbed to the trans-excited state (photoinduced absorption in Figure 1.15). Furthermore, the blue and red traces are tilted, giving a strong evidence of the conical intersection.

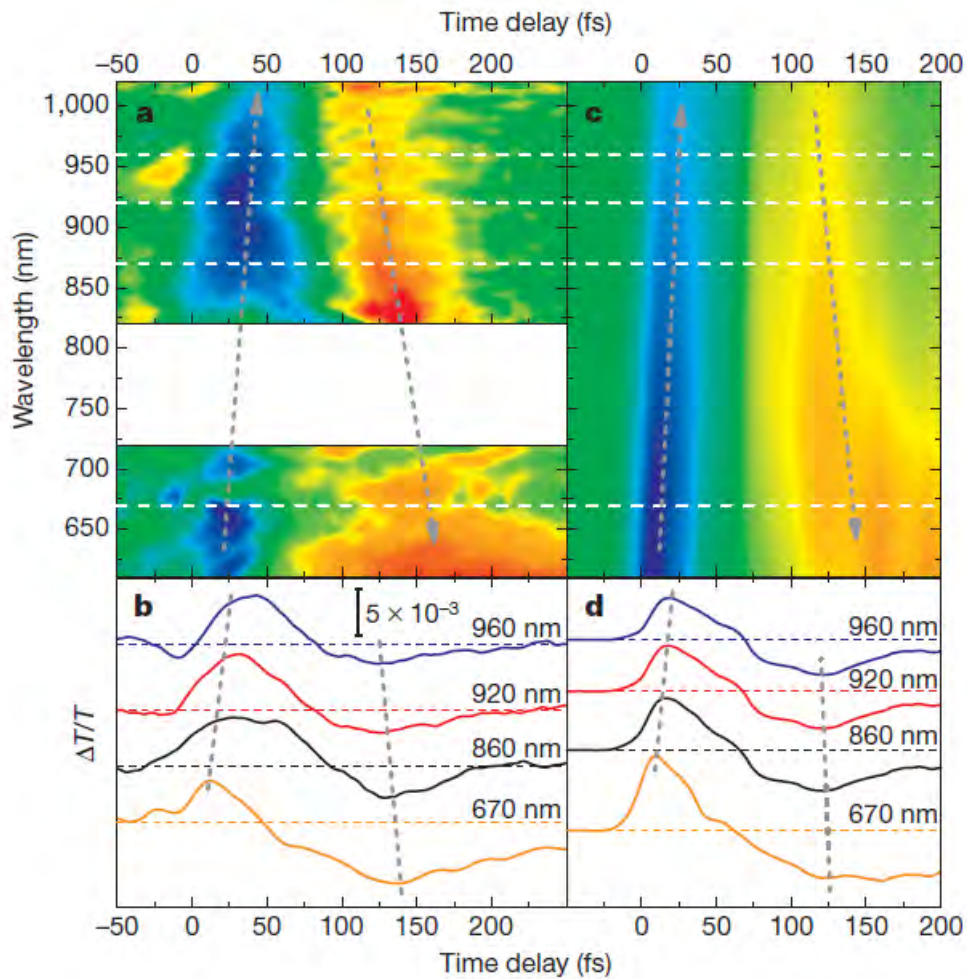


Figure 1.14: Transient absorption results from Polli et al.⁵. a-c: Experimental data ,b-d: Simulation. the blue part corresponds to stimulated emission, while the red part corresponds to absorption.

Smitienko et al.³³ have demonstrated a scheme for reversing the isomerization of rhodopsin (from bathorhodopsin to rhodopsin, see Figure 1.16 and Figure 1.17). Once the rhodopsin is in the trans-excited state, it returns through the conical intersection, and therefore, ending either in the cis-ground state (reverse photo switch) or in the trans-ground state. The possible pathway described by this two experiment is depicted in the Figure 1.15.

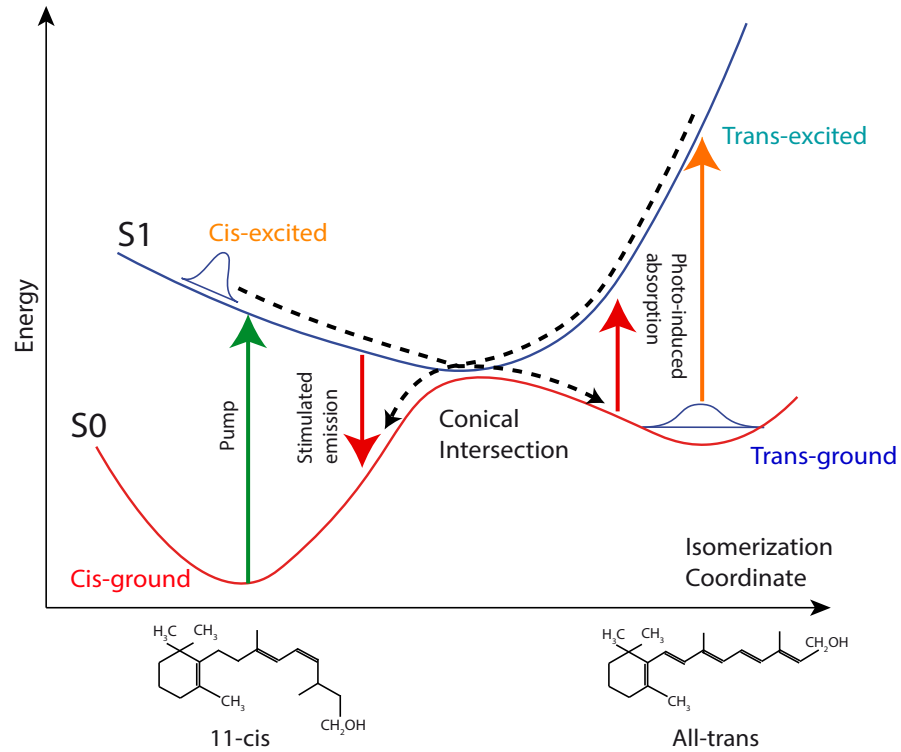


Figure 1.15: Sketch of the rhodopsin energy level, with corresponding pathway.

The trans-ground state is also called photorhodopsin. After several ps, it relaxes in bathorhodopsin, lumirhodopsin and metarhodopsin-I. (Figure 1.17). These are all thermal conversion products³⁴. They differ mainly from one another by their absorption spectrum, shown in Figure 1.16. The complete rhodopsin cycle is showed in Figure 1.17.

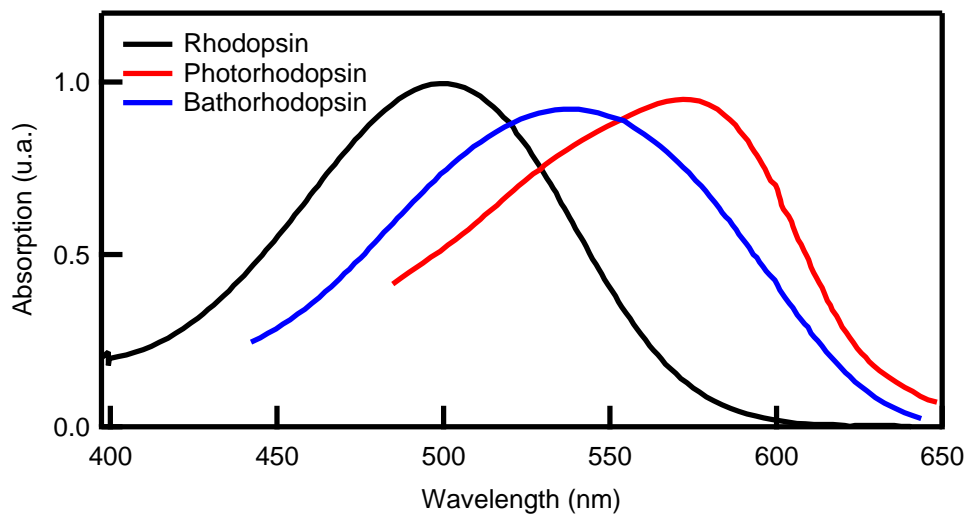


Figure 1.16: Rhodopsin (black), photorhodopsin (red) and bathorhodopsin (blue) absorption spectrum. Data from Kandori et al.³⁵

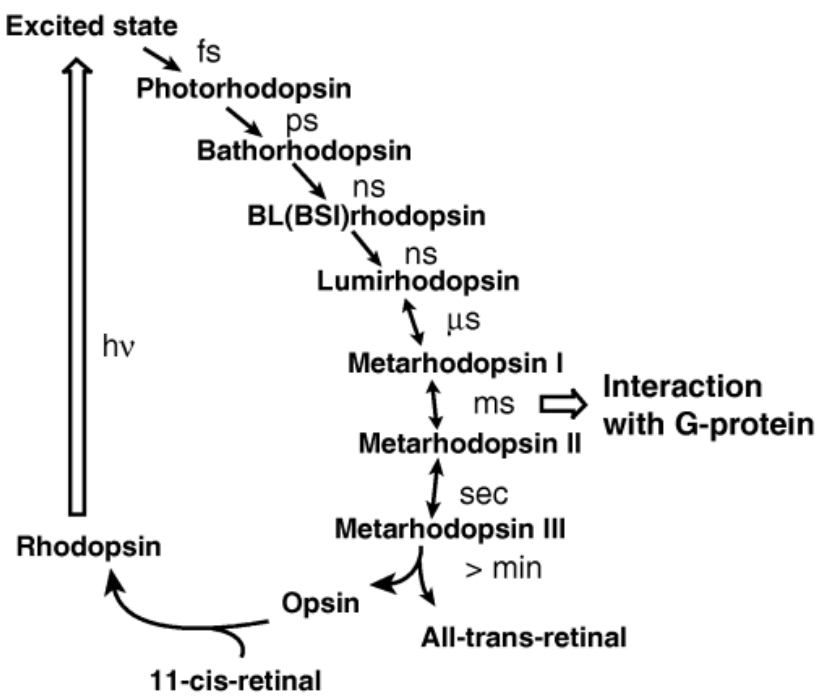


Figure 1.17: Rhodopsin cycle, from Shichida et al.³⁶

1.2.4 Electroretinogram

We describe in this section a way to measure the electric signal generated from the isomerization described in the subsection 1.2.3.

As long as no light is absorbed by the retinal, the channels between the inside of the outer segment and the outside of the cell are constantly open, allowing the influx of sodium ions. The depolarization due to the incoming of positive ions let the synaptical part of the rhodopsin fire glutamate, a neurotransmitter, to the bipolar cells.

However, when photons isomerizes the retinal inside the rhodopsin, a cascade of biological processes closes channels of the outer segment, decreasing the neurotransmitters firing to the bipolar cells. Interestingly, the lack of neurotransmitter acts as a light detector for the brain.

The isomerization from 11-cis to all-trans is the only light dependent process during the whole visual pathway. A few milliseconds after isomerization, after the all-trans ground state, the rhodopsin is promoted to a conformational state called metarhodopsin II, which can activate a G-protein called transducin ($T_{\alpha\beta\gamma}$, where $\alpha\beta\gamma$ are subunit of the transducin). The activation consists in a conformational change once the metarhodopsins binds to a receptor on the G-protein³⁷. In its inactive form, the transducin binds to GDP (guanosine diphosphate). However, once activated, the transducin exchanges its GDP to GTP (guanosine triphosphate) and loses the two subunits $\beta\gamma$. The metarhodopsin II can activates hundreds of transducin, therefore amplifying the signal.

The GTP- T_α binds to and activates the phosphodiesterase (PDE) enzyme. This latter catalyses the hydrolysis of cGMP (Cyclic Guanosine MonoPhosphate). Inside the cell, cGMP maintain open the channels between the outer segment and the outside of the cell. The hydrolysis of cGMP reduces the number of channels opened, inducing an hyperpolarization^{20;22;38}. This biological cascade decreases the number of glutamate transmitted to the bipolar cell, as shown in Figure 1.18. Bipolar cells respond to graduated potentials from the photoreceptor cell, instead of the traditional action potential. The decrease of neurotransmitters depolarises retina bipolar cells, which let it transmit the signal to the retinal ganglion cells, which form the optical nerve. The ganglion cells turn the signal into action potential, instead of the graduated potential the rods and the bipolar cells use. This action potential is later interpreted by the brain.

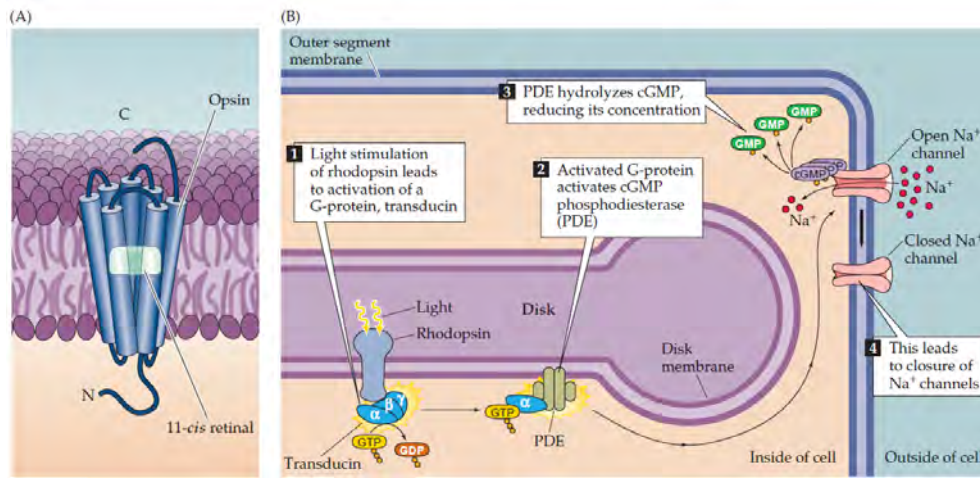


Figure 1.18: Schematic of the rods visual phototransduction, from Purves et al.²⁰. A. Structure of rhodopsin embedded inside the disk of the rods of Figure 1.12. B. Phototransduction pathway.

It is possible to measure the changes of electrical potentials the retina undergoes. The hyperpolarization caused by the closure of channels in rods is measured at the level of the cornea, and its expression is measured as the A-wave in Figure 1.19. The depolarization of the ganglion cells is associated with the B-wave origin. Together, they form an electroretinogram (ERG). This electroretinogram is the main observable used in this work to correlate the visual response to specific photo-excitation conditions.

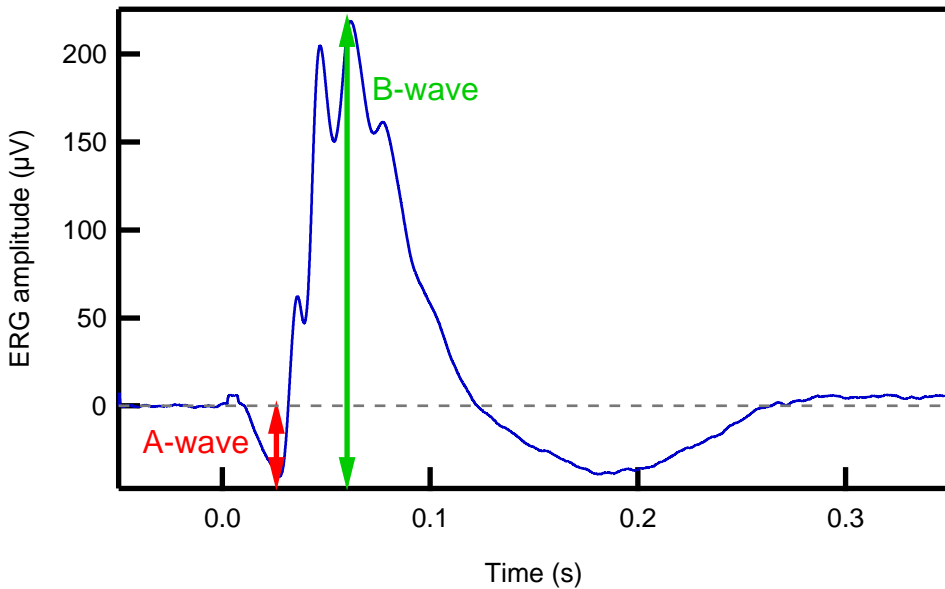


Figure 1.19: Electroretinogram of a mouse, in dark conditions. The A-wave is the hyperpolarization in the red curve. The B-wave is the depolarization measured in the green curve.

1.2.5 Genetic modifications of vision photo-receptors

For the experiments discussed in the chapter 2, one of the main concerns is the possible overlap of the excitation with different types of photo-receptors. For specific cases, it is possible to reduce the signal coming from cones and increase the one coming from rods by measuring under scotopic conditions (*i.e.*, the threshold below which cones do not participate to the visual process). However, for other experiments, it is useful to modify genetically the mouse, *i.e.* to selectively prevent S-, M- cones or rods.

The CRISPR-Cas9 technique^{39;40} has been used in this study by our colleagues at the biology department (Prof. I. Rodriguez) to produce mice with specific modifications in the receptor population. Specifically, we used four genomes: $\text{Rho}^{\text{del}/\text{del}}$, $\text{Rho}^{\text{del}/\text{wt}}$, $\text{Opn1mw}^{\text{del}/Y}$ and $\text{Opn1mw}^{\text{wt}/Y}$:

- $\text{Rho}^{\text{del}/\text{del}}$: Rhodopsin deletion/deletion, the gene that codes the rhodopsin phenotype is removed from both alleles. The mouse shows no rhodopsin phenotype. Both S- and M-cones are present.
- $\text{Rho}^{\text{del}/\text{wt}}$: Rhodopsin deletion/wild type, the gene is recessive. Therefore, the mouse's retina is the same as the wild type mouse.

- $\text{Opn1mw}^{del/Y}$: Opsin 1 medium wavelength: deletion/Y: the gene coding for the M-cones is present only on the X chromosome. As the mouse used in this work are only male, deleting its gene from the only X chromosome is enough to delete the corresponding phenotype. The retina displays functional rhodopsin and S-opsin proteins only.
- $\text{Opn1mw}^{wt/Y}$: Opsin 1 medium wavelength: wild type/Y: the mouse's retina is the same as the wild type mouse.

$\text{Rho}^{del/wt}$ and $\text{Opn1mw}^{wt/Y}$ genotypes exhibit the same genotype, containing both rods and cones.

Chapter 2

Experimental techniques and data analysis

In this chapter, we discuss the experimental setups used in this work. We first detail the lasers characteristics, such as the Ti:Sapphire regenerative amplifier system and the non-collinear parametric amplifier. In a second part, we discuss the experimental setup designed to investigate the retina response, whether using an intra-pulse or multi pulse approach. Finally, we'll discuss the procedure and tools used to perform measurements on living mice.

2.1 Laser Sources

The laser used for this work is a femtosecond amplified system coupled with an optical parametric amplifier⁴¹. The basic principle of chirped-pulse amplification system is detailed in the subsection 1.1.1.

The *Astrella* laser system, manufactured by *Coherent*, is the chirped pulse amplification system used in this work. It consists of a Ti:Sa oscillator, amplified by a regenerative amplifier. Its mains characteristics are displayed in Table 2.1.

Central wavelength	800 nm
Bandwidth	25 nm
Pulse duration	35 fs
Pulse energy	7 mJ
Repetition rate	1 KHz

Table 2.1: *Astrella*'s characteristics

2.1.1 Non collinear parametric amplifier

We use the non-collinear parametric amplification (NOPA) system *TOPAS-White* produced by *Light Conversion*. Its mains characteristics are displayed in Table 2.2.

Tuning range	500-700 nm, 850-1000nm
Pulse duration	between 30 and 80 fs
Pulse bandwidth	~ 1.8 transform limit
Pulse energy	10-60 μJ

Table 2.2: *TOPAS*'s characteristics

The beam adaptation to pump the TOPAS consists in a beamsplitter to reduce the pulse energy to 1 mJ, and a reflective beam size reducer ($f_1 = 1$ m and $f_2 = -33$ cm) to obtain a 9 mm diameter beam.

The TOPAS-white is a two-stage non-collinear parametric amplifier, pumped by pulses of 1mJ and central wavelength 800 nm. A small fraction is used to generate white-light via self-phase modulation. The white light is compressed via a grating compressor and focused in a non-linear crystal. The main part of the 800 nm pulse energy is doubled via SHG, split in two, and pumps the same non-linear crystal twice. By controlling two delay stages, the white light is amplified twice, and the wavelength is tuned by controlling the phase-matching and the delays between the pumps and the white light. The pulse is compressed by controlling two wedged windows before the output of the system. A more theoretical explanation of the optical parametric amplification process is detailed in the Appendix, section 4.5.1.

2.2 Two-photon vision control set-up

In this experiment, we performed a spectral phase control of an infrared pulse, to probe the two photon absorption of the rhodopsin.

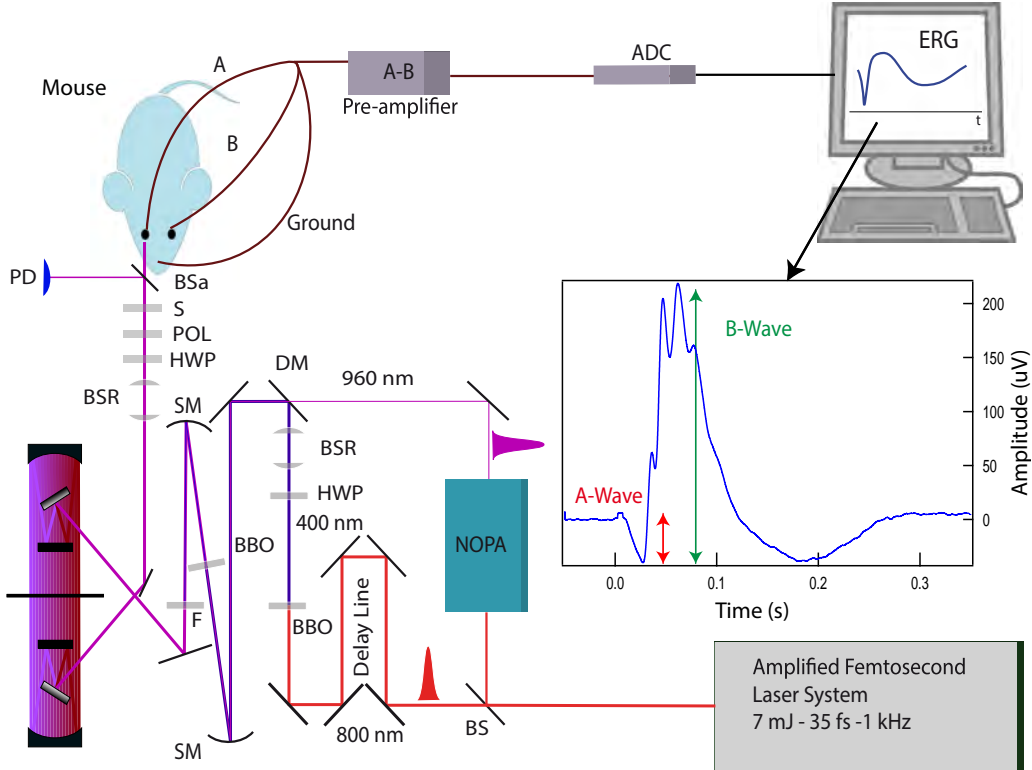


Figure 2.1: Experimental setup for two-photon vision control set-up. BS: Beamsplitter, NOPA: Non Collinear Optical Parametric Amplification, SM: Spherical Mirror $f = 2m$, BBO: Beta Barium Borate non-linear crystal (Cutting angle for both: 29.2° , Thickness 2 mm, Eksma), F: Longpass 800 (FELH800 - Thorlabs), DM: Dichroic Mirror, HWP: Half Wave Plate, POL: Polarizer, S: Shutter, BSR: Transmissive Beam Size Reducer ($f_1 = 50$ cm and $f_2 = -20$ cm), ADC: Analog to Digital Convertor, PD: Photodiode, ERG: Electroretinogram

The output from the Ti:Sapphire amplifier is split in two pulse trains. The first one pumps the NOPA producing output pulses of 80 fs at 960 nm, with a corresponding energy of 7 μ J. The pulse shaper induces significant loss of energy, due to the grating efficiency, and no ERG could be measured at this energy level. To circumvent this problem, we mounted an additional home-made OPA stage to increase the final output, which is pumped by the second part of the amplified system (Figure 2.1). With this configuration, the output reaches 40 μ J, 120 fs pulse duration.

The beam is spectrally shaped by the pulse shaper, using a spatial light modulation (SLM-S640, by Jenoptik) in a 4f-line. The 4f-line is wrapped

under a X-geometry, as shown in Figure 2.2. Its configuration allows for easier alignment and less aberration from the beam, such as spatial chirp⁴². The grating disperses the spectrum on a flat mirror, directed to a cylindrical mirror ($f = 55$ cm). The beam path is reversed after the passage through the SLM.

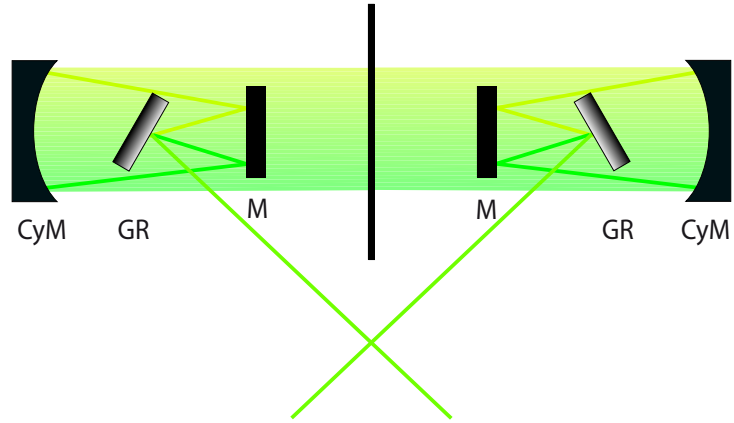


Figure 2.2: Pulse shaper in X-Geometry. CyM: Cylindrical Mirror, M: Plane mirror, GR: Grating. The pulse shaper is placed in the middle. This corresponds to the more convenient alignment⁴².

After being spectrally shaped by the pulse shaper, the divergence of the beam is modified using the beam reducer (by optimizing the position of the last lens with the ERG signal). A fast silicon photodiode (SM05PD28) combined to a gated integrator (SR280 - Stanford Research Systems) measures the energy of each pulse, and a combination of a half wave plate and a polarizer mounted on a computer-controlled motorized rotational stage (PRM1/MZ8 - Thorlabs) are used to modify the pulse energy. Five pulses of $5\mu\text{J}$ illuminates the eye every two seconds.

For this experiments we first compressed temporally the pulse to its transform-limit via a genetic algorithm⁴³, and then applied a step of amplitude π on the spectral phase, and scan the position of the pi-step inside the spectrum.

2.3 Intra-pulse coherent control

2.3.1 Set-up

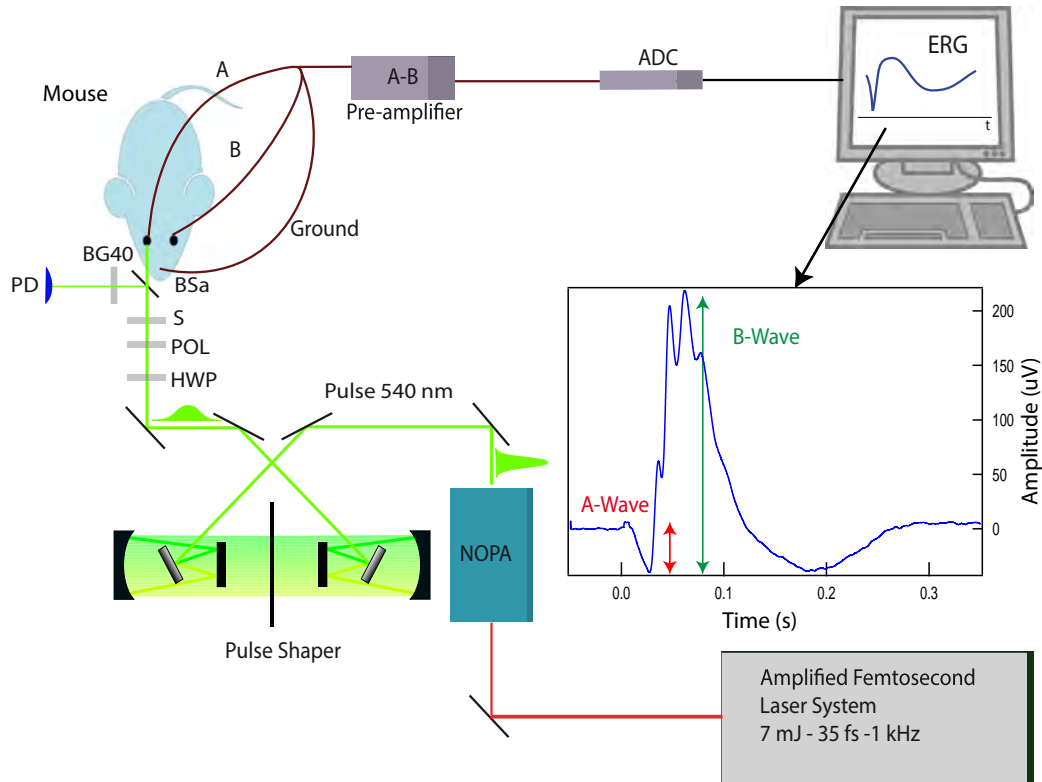


Figure 2.3: Experimental setup for intra-pulse coherent control. NOPA: Non Collinear Optical Parametric Amplification, HWP: Half Wave Plate, POL: Polarizer, BSa: Beam Sampler, BG40: Color glass bandpass filter (FGB37M - Thorlabs), S: Shutter, PD: Photodiode, ADC: Analog to Digital Convertor, ERG: Electroretinogram

The NOPA output (50 fs, 535 nm central wavelength $\Delta\lambda = 30$ nm FWHM) is temporally shaped by a spatial light modulator (SLM-S640 by Jenoptik) in a 4f-line. A fast silicon photodiode (SM05PD28 - Thorlabs) combined to a gated integrator (SR 280 - Stanford Research Systems) measures the energy of each pulse, and a combination of a half wave plate and a polarizer mounted on a computer-controlled motorized rotational stage (PRM1/MZ8 - Thorlabs) allows maintaining a constant average pulse energy while varying the SLM settings. For each setting, the chirp is measured by taking a SHG FROG (APE PulseCheck). A fast electronic shutter (Newport model 76992) allows five pulses of 3 nJ each to illuminate one eye of the mouse under study

with a two seconds dark period in each cycle.

2.3.2 Energy correction

The pulse shaper is calibrated prior to the experiments. It is therefore normally sufficient to apply a phase function (Equation 2.1), which is subsequently converted into volts by the control software, and applied to each pixel.

$$P(p) = \alpha(p - \gamma)^2 + \delta \quad (2.1)$$

Where p stands for pixel (there are 640 pixels) and α the linear wanted chirp. γ is used to correct for the position of the beam, as it might not be centred on the pulse shaper. δ is a fine-tuning parameter for the temporal pulse shape. The pulse shaper, at 535 nm, cannot apply a phase difference greater than 7π . It is therefore necessary to wrap the phase. However, wrapping the phase induces abrupt discontinuities. Indeed, as there is always a small calibration error, the phase is no longer continuous. These jumps are also refractive index jumps, which can change the spectrum and spatial shape of the beam. Therefore, we should apply as little wrapping as possible to maintain the same spectrum to each pulse.

The pulse shaper can also uniformly reduce the spectral intensity, and therefore modify the energy between the different phase-conditions used. It is therefore necessary to correct for this modification, so that each pulse has the same energy. This is achieved by inserting a combination of a polarizer and a half-wave plate. The calibration of the half-wave plate for the correction is achieved prior to the experiment. The two seconds delay, necessary to avoid the bleaching of the photo-receptors between each excitation condition tested on the animal is used for changing the phase function and for correcting for energy differences.

2.4 Multipulse coherent control

The multipulse coherent control experiment is a pump-dump/re-pump scheme, where a first pulse excites the rhodopsin, and a second controls the isomerization depicted in the subsection 1.2.3 via stimulated emission or re-pumping. It is realized with pulses of both long and short duration.

2.4.1 50 fs-pulse pump probe set-up

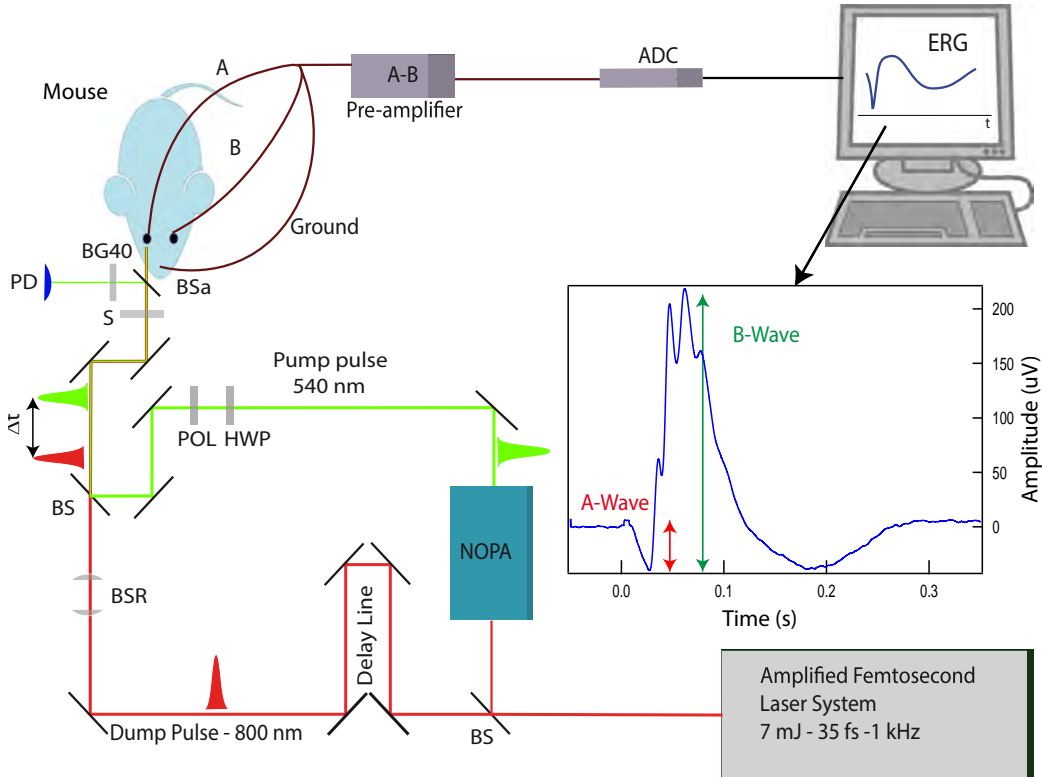


Figure 2.4: Experimental setup for long multipulse coherent control. BS: Beamsplitter, NOPA: Non Collinear Optical Parametric Amplification, HWP: Half Wave Plate, POL: Polarizer, BSa: Beam Sampler, BG40: Color glass bandpass filter (FGB37M - Thorlabs), BSR: Transmissive Beam Size Reducer ($f_1 = 50$ cm and $f_2 = -20$ cm), S: Shutter, PD: Photodiode, ADC: Analog to Digital Convertor, ERG: Electretoretinogram

The output from the Ti:Sa amplifier is split in two pulse trains: one pumps the NOPA and its 50 fs, 535 nm output is kept unchirped (pump pulse). It is attenuated to 3 nJ. The other (dump pulse: 800 nm, 1 μ J, 50 fs) is delayed by a computer-controlled motorized linear stage (PI model M-505.4DG). Finally, both beams are recombined with a temporal delay, measured by sum frequency generation in a BBO non-linear crystal.

The pulses are coupled onto the mouse eye in the same fashion as in the intra-pulse experiment: the fast shutter allows five pump-dump pulse pairs to illuminate one eye.

One should be careful to not induce any measurable signal with the 800 nm pulse. Indeed, even so the absorption of rhodopsin at 800 nm is low compared to the absorption at 535 nm, the energy of the dump pulse is magnitude higher than the energy of the pump pulse. At 1 μJ , no measurable signal was recorded with the 800 nm pulse only.

2.4.2 25 fs-pulse pump probe set-up

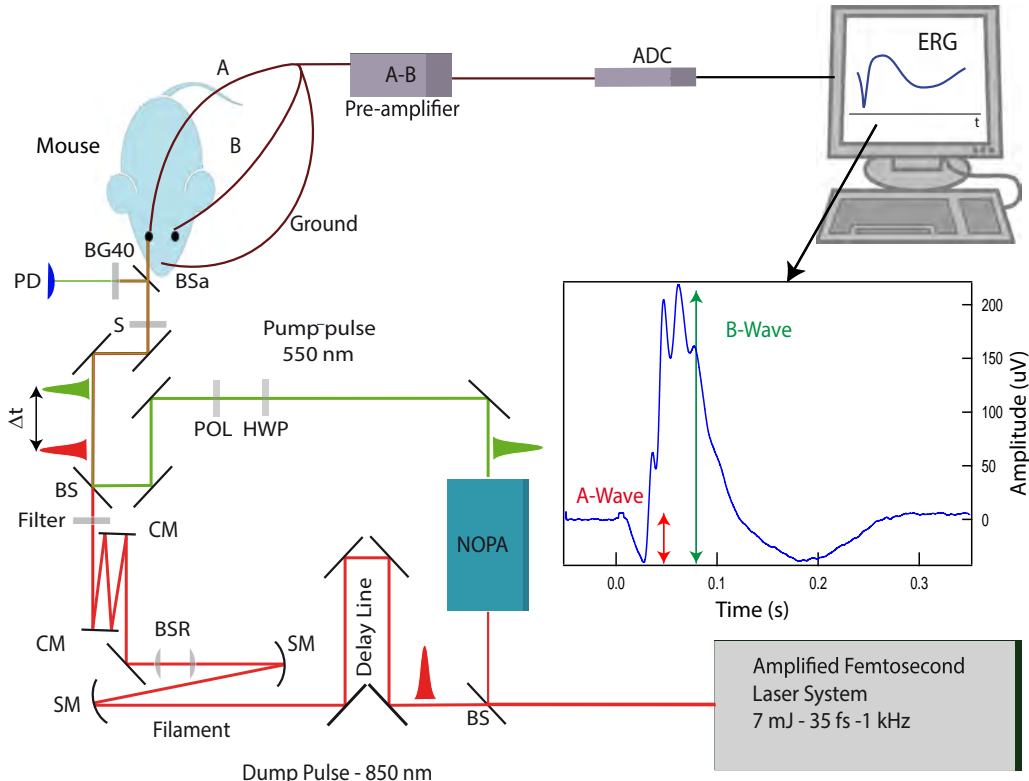


Figure 2.5: Experimental setup for long multipulse coherent control. BS: Beamsplitter, NOPA: Non Collinear Optical Parametric Amplification, SM: Spherical Mirror $f = 2m$, BSR: Transmissive Beam Size Reducer ($f_1 = 50 \text{ cm}$ and $f_2 = -20 \text{ cm}$), CM: Chirped Mirror (Layertech, -120 fs^2 , oscillation compensated), Filter: Bandpass 850-40 nm (FB850-40 - Thorlabs), HWP: Half Wave Plate, POL: Polarizer, S: Shutter, BSa: Beam Sampler, BG40: Color glass bandpass filter (FGB37M - Thorlabs), ADC: Analog to Digital Convertor, PD: Photodiode, ERG: Electrotoretinogram

Short pulses are key to observe details of the isomerization of rhodopsin, as the conical intersection is crossed in less than 80 fs⁵. An improvement of the experiment described in the subsection 2.4.1 is therefore useful:

- The NOPA system was improved to output 25-30 fs, centred at 550 nm.
- To reduce the pulse duration, the bandwidth must be increased. We use the filament-based pulse compression technique to obtain 11 fs beam centred at 800 nm (Figure 2.6). However, the new bandwidth overlaps more with the absorption spectrum of rhodopsin. A pulse energy of 1μJ now induces a measurable signal. A compromise must therefore be found between pulse duration, bandwidth and energy.

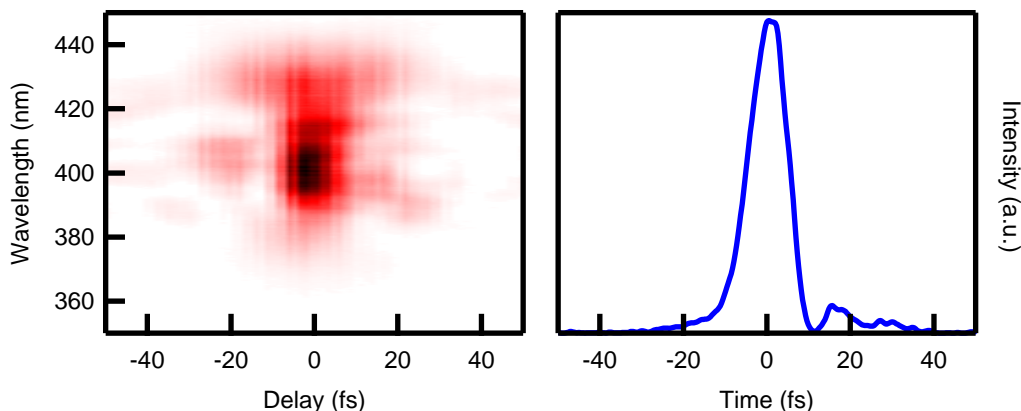


Figure 2.6: Left: measured FROG after pulse duration reduction by filamentation. Right: retrieved pulse of 11 fs, centred at 800 nm

To avoid this issue, we added a color filter (FB850-40 - Thorlabs) 850-40 nm. This optical component solves the problem but it entails an increase of pulse duration from 11 fs to 30 fs due to the decrease of bandwidth as seen in the Figure 2.7.

The rest of the setup is similar to the long pulse pump-dump/re-pump. (subsection 2.4.1).

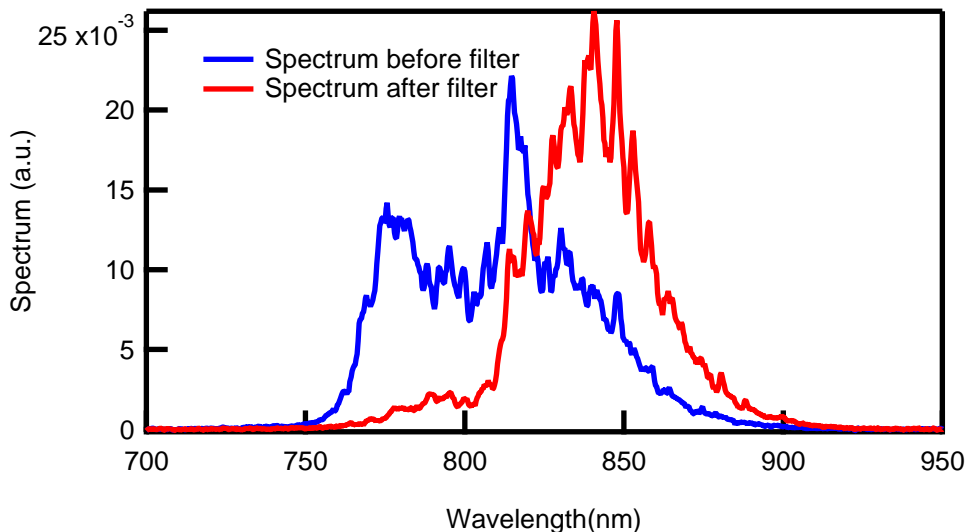


Figure 2.7: Blue: Spectrum of the pulse after filament, without filter. Red: Spectrum of the pulse after filament and the color filter.

2.5 Detection System

2.5.1 Illumination method

A standard ERG, as displayed in the Figure 1.19, requires a short illumination time compared to the length of the ERG signal, typically around 300 ms.

A fast electronic shutter (Newport model 76992) allows five pulses each to illuminate one eye of the mouse under study with a two seconds full cycle. A triggering software controls both the illumination event and the ERG acquisition: the differential bio-electric signal from the two retinas is amplified by 5000 and bandpass-filtered with a pre-amplifier (SR560 by Stanford Research System, inc., between 0.3 and 3000 Hz) working on battery power. The *ex-vivo* system/anaesthetized mouse and the pre-amplifier are enclosed in a custom-made Faraday cage to reduce the 50 Hz noise pickup. The analog signal is digitized by an analog to digital converter (ADC- PCI-6220 by National Instruments) with a sampling frequency of 25 kHz connected to a computer and controlled by a dedicated acquisition software. During a data acquisition run, the ERG signal is typically sampled a few milliseconds before and after a single illumination event.

2.5.2 Animal handling techniques

For both *ex-vivo* and *in-vivo* experiments, mice are dark-adapted for two hours prior to experiments. They are anaesthetized with an intraperitoneal injection of ketamine (90 mg/kg) and xylazine (10 mg/kg) solution under dim red light (PF712 Dr FISCHER).

2.5.2.1 *Ex-vivo* acquisition of electroretinogram

During a part of this work, the ERG was acquired directly on mouse retinas, in an *ex-vivo* setup, purchased from Ocuscence (USA). In this configuration, after the sacrifice of the mouse, the eye is gently detached from the optical nerve, and dissected, to extract the retina. The use of pentobarbital to euthanize the animal is not advised in this case, as it is reported that this drug strongly perturbs the ERG traces⁴⁴. The whole procedure is realized in the dark, using only a dim red light. The eye is detached in Ames' medium (Sigma Aldrich) mixed in distilled water, suitable for maintaining the cell alive. The retina is afterwards attached to the holder, in Figure 2.8. Note that the holder is designed to acquire the signal from two retinas, although in this work we limited the acquisition to a single retina at a time.

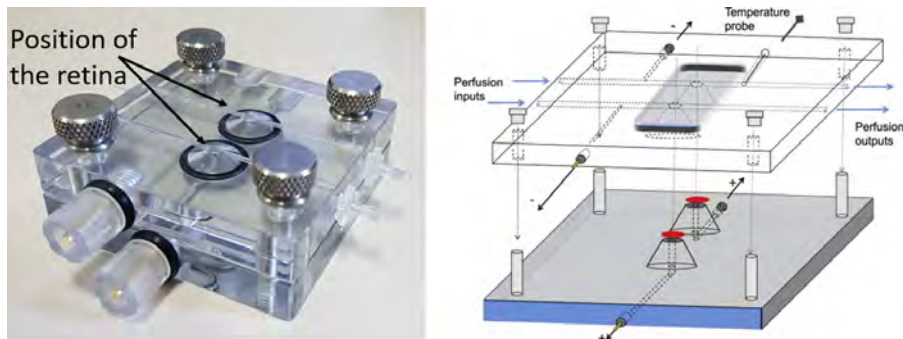


Figure 2.8: Left: Picture of the holder. One can see the two retinas position. Each retina is deposited on a 0.45 μm nitrocellulose filter. The electrolyte solutions lies between the electrode and the retina. The perfusion, filled with Ames' medium, flows on the top of the retina.⁴⁵ Right:Schematic of the holder. Figure adapted from Vinberg et al.⁴⁵

The signal is acquired via an electrode embedded in a bath of electrolyte solution (NaCl 140 mM, KCl 3.6 mM, MgCl₂ 2.4 mM, CaCl₂ 1.2 mM, HEPES 3.0 mM and EDTA 0.01 mM) in contact with the bottom of the retina. The other electrode is connected to the perfusion, which flows on the retina at a

low flux (around 50 mL/hour). The two electrodes are connected to a differential amplifier. The perfusion itself consists in an heated Ames' medium (37° , oxygenated using a 95%5% CO₂/ O₂).

Prior to the experiment, to insure the electrolyte solution is correctly set, the perfusion and the electrolyte channel are both filled with electrolyte solution, and the resistance between the two is measured. A value below 200 kΩ is sufficient for performing the acquisition, but a typical working value is approximately 40 kΩ.

This approach presents several differences compared to the *in-vivo* measurements:

- The physiological noise (respiratory rate, heart rate) is not present, increasing the signal over noise ratio.
- The signal can be measured for up to 10 hours.
- The retina can be stored at 4° C in an Ames medium and used up to 12 hours.
- The cornea and the crystalline lens are no longer part of the beam path. Indeed, their presence can have an effect on the pulses' characteristics, such as divergence or pulse duration.
- The signal is approximately 10 times smaller, and therefore the 50 Hz noise signal must be filtered out more efficiently to keep the same signal over noise ratio.
- As the retinal pigment epithelium is no longer attached to the retina, the recycling from the all-trans to the 11-cis of the retina is lowered⁴⁶, and the signal decreases over time.

2.5.2.2 *In-vivo* acquisition of electroretinogram

45 min after the primary injection and every 40 min, a solution of ketamine (15 mg/kg) and xylazine (3 mg/kg) is injected to maintain anesthesia, for a total duration of 2h30 of anesthesia. The temperature of the mice is maintained using a hand warmer and a cover. After the initial anesthesia, one drop of mydriatic (Mydriaticum Dispersa 5 mg/ml, Omnivision) is deposited on each eye. Electrodes are then applied on both eyes. To improve the conductance of the signal between the eyes and the electrodes, and to maintain moisture, drops of 2% hydroxypropyl-methylcellulose (Methocel 2%, Omnivision) are regularly casted.

To detect the ERG response we followed different approaches depending on the specific experiment.

52CHAPTER 2. EXPERIMENTAL TECHNIQUES AND DATA ANALYSIS

- In the case of intra-pulse coherent control experiment, a small tube filled with methylcellulose is apposed to the stimulated eye (Figure 2.9), with a flat glass window on the laser side of the tube. This arrangement prevented focusing of the beam on the retina, since the methylcellulose solution has the same refraction index as the cornea, and since the entrance pupil was flat. A tinned copper ring (3 mm diameter) connected to an electrical wire is centered and put in contact with each of the eyes of the animal.

We show in Figure 2.10 the effect of the index matcher on the spot size of an eye. For this control experiment, the cornea, crystallines lens and vitreous humour are detached from the rest of the eye, and put on a microscope. The focus of the microscope is set at the retina's level, and a camera record the images, with and without index matcher. Similarly, we perform ray tracing (Figure 2.11a and Figure 2.11b) of the beam in the eye using the ray-tracing software Code V. The results are similar, the index matcher greatly reduces the focussing of the beam.

- In the case of the multipulse and two photon coherent control experiments, small contact lenses (Figure 2.9 - OcuScience), with a 3 mm diameter, attached to a small silver lead, are affixed on both eyes. This arrangement allows for a better signal acquisition, and an increased intensity at the retina level. This is fundamental to obtain a two-photon absorption ERG.



Figure 2.9: Left: Silver-embedded lens - OcuScience, of 1.5 mm radius of curvature, in Aclar, a Polychlorotrifluoroethylene homopolymer film. Right: Silver-embedded lens - OcuScience, of 1.5 mm radius of curvature, in Aclar, a Polychlorotrifluoroethylene homopolymer film.

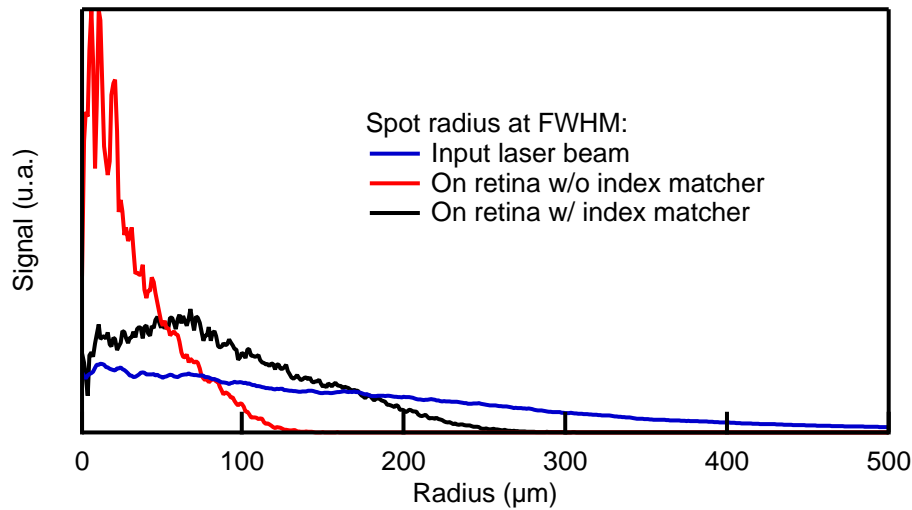
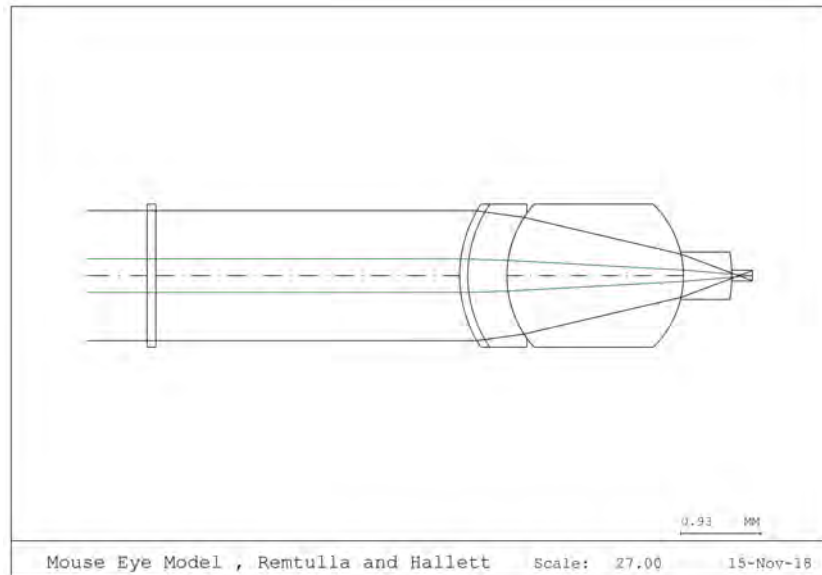
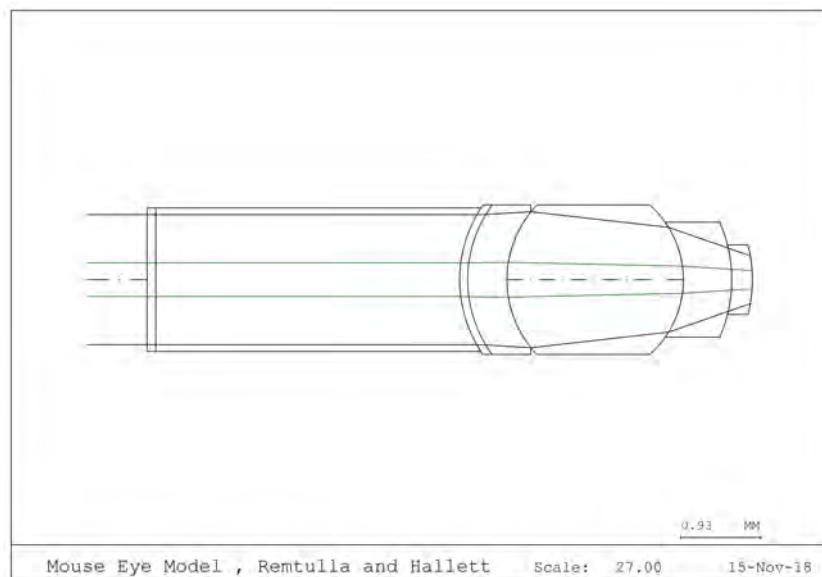


Figure 2.10: Measured beam size at the retina with (black curve - 130 μm radius) and without (red curve - 33 μm radius) the index-matcher. The blue line corresponds to the beam profile before entering the eye (207 μm radius). For these ex vivo measurements, the retina and the retinal pigment epithelium were delicately detached from the rest of the eye, leaving intact cornea, crystalline lens, and vitreous humour. Not actually performed by the main laser.



(a) Ray tracing of a 450 μm input beam propagating through the mouse eye in absence of an index-matcher layer



(b) Ray tracing of a 450 μm input beam propagating through the mouse eye in presence of an index-matcher layer

Figure 2.11: Ray tracing of a 450 μm input beam propagating through the mouse eye in absence (a) or presence (b) of an index-matcher layer. The calculated spot size on the retina is 250 μm , and 5 μm , with and without index matcher, respectively. Values for the radii of curvature, indices of refraction, and thicknesses of the various eye components (cornea, crystalline lens and retina) are taken from Remtulla et al.⁴⁷

2.6 Data analysis

For each experiment carried out during this work, a series of ERGs is measured after a light excitation. For each ERG, a linear regression is performed on the first 100 sampled points collected before each illumination event to determine the differential baseline. The signal is subsequently Fourier-filtered (Low pass at 50 Hz, finite order response of order 1501). This way, the amplitudes of the A- and B-waves are directly measured from the minimum and maximum values of the ERG. For each datasets, outliers are removed following the ChauvenetâŽs criterion⁴⁸. An example of Fourier analysis is shown in Figure 2.12.

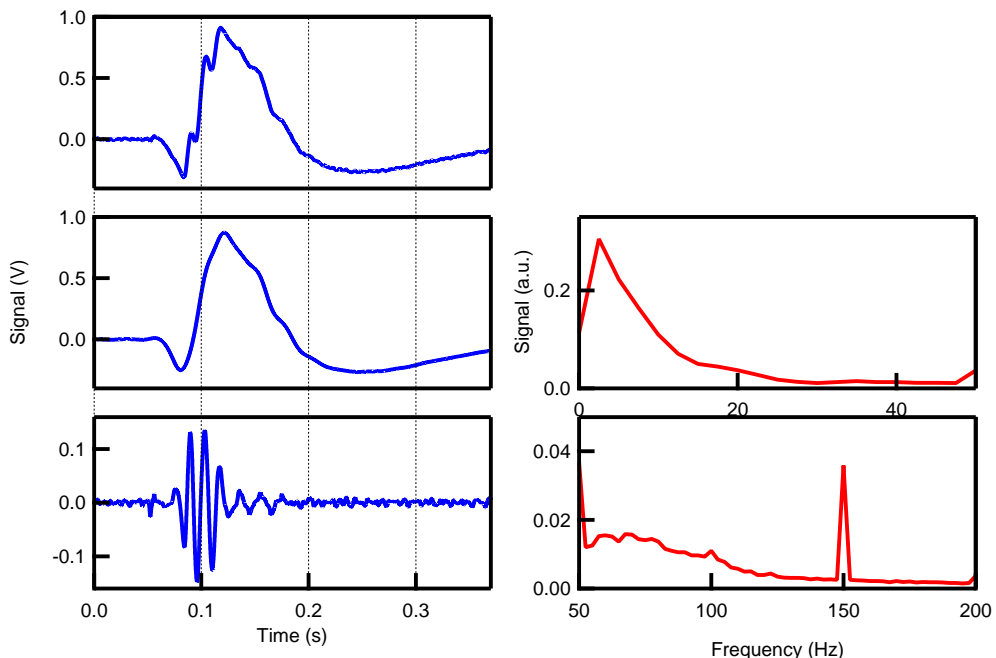


Figure 2.12: Fourier Analysis of the ERG. Left (top to bottom): top: average of 200 traces of ERG, middle: average of the filtered traces (between 0 and 50 Hz), bottom: average of the filtered traces between 50 Hz to 12500 Hz. Right: average of FFT of the same traces, between 0 and 50 Hz, and between 50 and 200 Hz).

The high frequency components are called the oscillatory potentials (OP). Although commonly observed in ERGs, their origin is not clearly identified⁴⁹, and is probably not linked to a single type of cell. They likely originate from the cells located between the photoreceptors and the ganglion cells⁵⁰.

56 *CHAPTER 2. EXPERIMENTAL TECHNIQUES AND DATA ANALYSIS*

The appearance of a frequency peak at 50Hz is due to poor contact between the electrodes and the retina, which changes the impedance of the electrodes. Removing this spurious component is one of the major advantages of Fourier analysis for this signal.

Chapter 3

Ex-vivo experiments

This chapter focuses on the experiments carried out *ex-vivo*, *i.e.*, the characteristics of the two-photon absorption in retina. This assessment was essential to perfect the ERG detection for the following experiments *in-vivo* (at one and two photons) and to investigate the excitation of the retina with femtosecond pulses.

3.1 Characterization of two-photon vision

Visual response upon two-photon absorption (TPA) on human volunteers was demonstrated in 2014 by Palczewska et al.⁵¹. In the same work, it was also confirmed on *ex-vivo* mice retinas. In our study, the *ex-vivo* approach was applied to perform a complete characterization of the effect of pulse duration, focal spot size and energy dependence upon excitation by infrared femtosecond pulses.

In this assessment of the two-photon absorption, we use an infrared pulse (960 nm) generated within the set-up described in section 2.2. The first part of the experiment consists in verifying that the response observed is actually compatible with a two-photon process, and therefore by definition, on the energy, the pulse duration and the diameter of the beam. For this study, the *ex-vivo* system is ideal, as it presents the advantage of working without the crystalline lens in the beam path. In the near infrared, the optical and spectroscopic characteristics of the mouse eye are not well established. It is also useful to prevent any chromatic dispersion, which temporally stretches the pulse, and therefore decreases the two-photon absorption.

We proceed to three experiments:

- Energy dependence: the pulse energy is freely adjusted by a combination of a motorized half wave plate and a polariser, for both a 960 nm and a 480 nm (obtained using the SHG of the infrared pulse). Results are shown in Figure 3.1.
- Pulse duration dependence: we applied a negative chirp using a commercial prism compressor (BOA - Swamp Optics), and measured the ERG as a function of the pulse duration of the infrared pulse. In the successive analysis, we renormalized the B-wave amplitudes with the energy used to generate them. Results are shown in Figure 3.1.B.
- Beam diameter dependence: we focused the infrared light using a f=35 mm lens, and measured the ERG as a function of the position of the lens. The size of the beam is measured using a beam profiler. Results are shown in Figure 3.1.C and D.

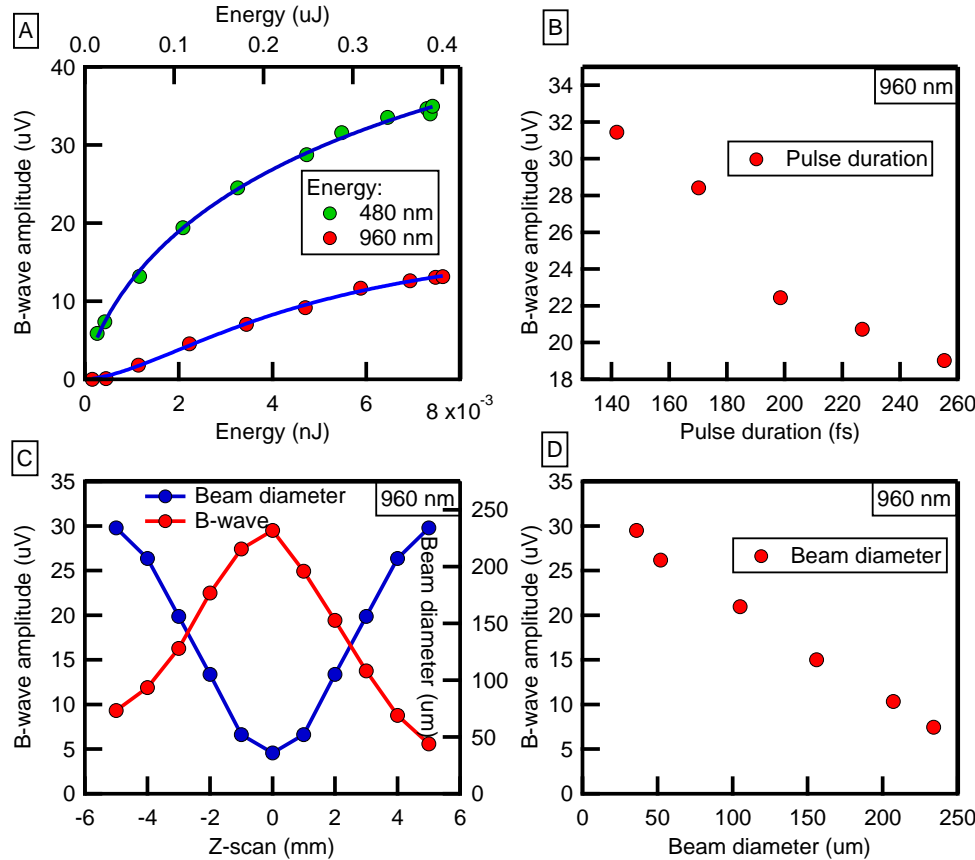


Figure 3.1: *Ex-vivo* characterization of the retinal response upon 960 nm femtosecond pulses. A: B-wave response upon 480 nm (green dots) and upon 960 nm (red dots) excitation. Blue lines: spline interpolation. B: B-wave amplitude as a function of the pulse duration. C: B-wave amplitude (red) and beam diameter (blue) as a function of the lens position (Z-scan). D: B-wave amplitude as a function of the beam diameter.

We clearly observe the following trends:

- In Figure 3.1.A, an ERG can easily be measured upon 960 nm excitation. We also notice that substantially more energy is needed to measure a B-wave at 960 nm (uJ) than at 480 nm (pJ). This is consistent with a response produced by an infrared pulse outside the linear absorption band of rhodopsin.
- In Figure 3.1.B, the B-wave decreases as the pulse duration increases at 960 nm, as would be expected from a two-photon process.

- In Figure 3.1.C and D, the B-wave also decreases as the beam diameter increases at 960 nm, which is also expected from a two-photon process. Note that the beam diameter was kept below 250 μm throughout the experiment. This was done to ensure that the density of the receptors in the region probed was sufficiently homogeneous to perform the comparison.

The different dependencies of the B-wave on the different variables (energy, pulse duration and size of the beam) show that the retinal response does not come from a linear absorption (*e.g.*, from the tail of the rhodopsin absorption spectrum), but rather a two-photon process.

In the next paragraphs, we will consider in detail the dependencies of the B-wave with respect to each of the experimental variable.

3.2 ERG energy, pulse duration and beam diameter dependence upon two-photon absorption

The response of the B-wave can always be splitted into two parts: a photo-molecular part, allowing the isomerization of rhodopsin, and a physiological part, which allows the transition from isomerization to the B-wave, which is the response of the system. In the case of single-photon absorption, the number of isomerization is linearly dependent on energy, and not dependent on pulse duration or beam size. However, at two-photon, the number of isomerized rhodopsin increases quadratically with energy, but decreases with pulse width and beam diameter. The response of the system, due to the physiological response, remains independent from the excitation mechanism part (*i.e.*, single-photon or two-photon absorption, wavelength), and depends only on the number of isomerization.

We first detail the photo-molecular part.

The simple rate equations model (*i.e.*, not taking in account stimulated emission) for single and two-photon absorption, for a two-state model is as follows:

$$\frac{dN_2}{dt} = \sigma_1 N_1(A) I(A, t) \quad (3.1)$$

$$\frac{dN_2}{dt} = \sigma_2 N_1(A) I(A, t)^2 \quad (3.2)$$

3.2. ERG ENERGY, PULSE DURATION AND BEAM DIAMETER DEPENDENCE UPON TWO-PHOTON ABSORPTION

Therefore, the number of molecules excited state, in the case of two photon absorption, becomes:

$$N_2 = \sigma_2 \int_t N_1(A) I(A, t)^2 dt \quad (3.3)$$

To perform this integral, we used a Monte-Carlo code to simulate the response of an array of 500x500 i.d. (intermolecular distance) of equally spaced rhodopsin proteins molecule for two-photon absorption. Each square represents one rhodopsin, which has a probability $\sigma_2 I^2$ to be excited. We designed a 2D Gaussian beam of varying pulse duration ΔT , diameter σ and energy, centered at $x_0 = y_0 = 250$.

$$f(x, y, t) = A_0 \cdot e^{-\left(\frac{(x-x_0)^2}{2\sigma^2} + \frac{(y-y_0)^2}{2\sigma^2}\right)} \cdot e^{-4 \ln 2 \left(\frac{t}{\Delta T}\right)^2}$$

Note that for these calculations, the value of σ_2 is chosen as to not saturate the response (*i.e.*, less than 1% of rhodopsin are excited).

The simulation is repeated multiple times for various sizes of the Gaussian beam, pulse duration and energy and the results are shown in Figure 3.2.

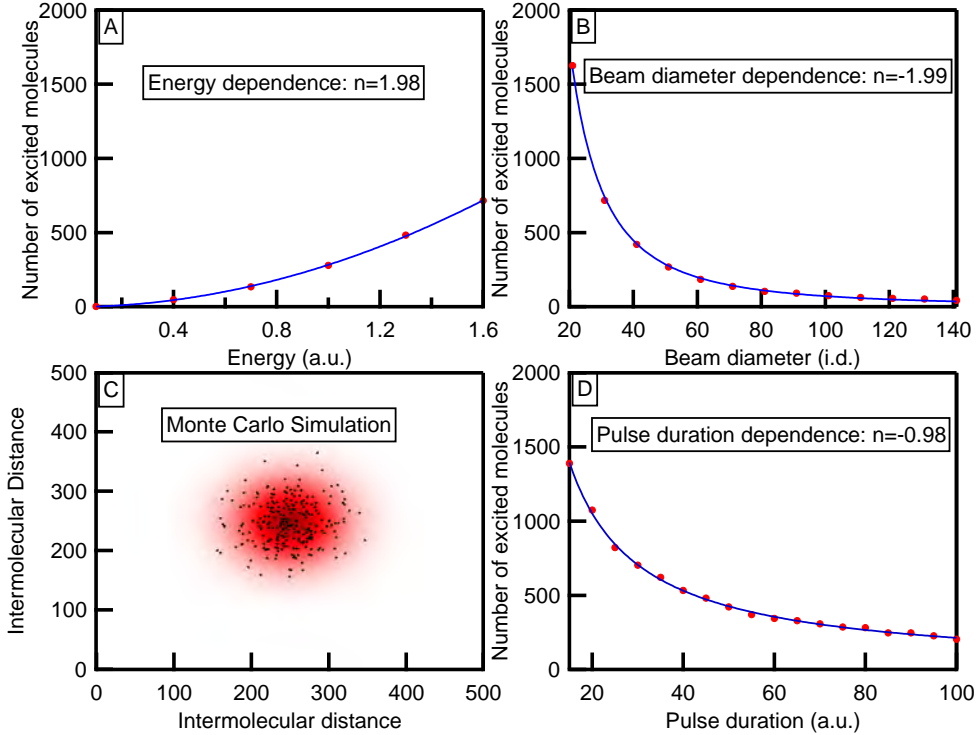


Figure 3.2: Simulation of two-photon absorption in molecules. In every figures, the blue curves represents the best fit using the function $f(x) = ax^n + y_0$. A: Simulated number of excited molecules as a function of the energy, $n = 1.98$. B: Simulated number of excited molecules as a function of the beam diameter, $n = -1.99$. C. Slice of the Monte-Carlo simulation at $t = 0$, using a Gaussian beam, with diameter $\sigma = 50\text{i.d.}$ (intermolecular distance). Black dots represent the excited molecules. D: Simulated number of excited molecules as a function of the pulse duration, $n = -0.98$.

Using the fit function $f(x) = ax^n + y_0$, we see that the number of excited molecules increases with the energy ($n = 1.98$), decreases with the beam diameter ($n = -1.99$), and decreases with the pulse duration ($n = -0.98$).

We now discuss in more details the mechanism leading from molecular isomerization to the ERG. The response of the system is first measured upon visible excitation (Figure 3.1.A). Indeed, as the dependence of the single-photon absorption on the pulse energy is linear, we directly obtain the response of the system.

3.2. ERG ENERGY, PULSE DURATION AND BEAM DIAMETER DEPENDENCE UPON TWO-PHOTON ABSORPTION

One should however note the different saturation levels of the B-wave of one and two photons. Indeed, in Figure 3.1.A, we see that the B-wave amplitude upon 960 nm excitation saturates at $13 \mu\text{V}$, without reaching the level of the B-wave upon 480 nm, at $34 \mu\text{V}$. This is because, in this *ex-vivo* system, the retinal inside the rhodopsin is not recycled to the cis-ground state fast enough, as it would be in the eye. Indeed, the RPE (retinal pigment epithelium) is the primary way of recycling rhodopsin, and it is removed from the eye for this system⁵². As the time delay between each experiment realized on this retina is different, the bleaching level of the retina is also different. It is therefore very complicated to compare a calculated B-wave using the dependencies of two-photon absorption and the response system of the retina and the measured B-wave upon two-photon absorption.

However, it is possible to compare the rates of Equation 3.1 and Equation 3.2, using the values found in the literature. The single-photon absorption cross-section σ_1 for the cis-ground state can be calculated from the molar extinction coefficient ($\epsilon = 40200 \text{ cm}^{-1}\text{M}^{-1}$)⁵³.

$$\sigma = \ln(10) \frac{10^3}{N_A} \epsilon \quad (3.4)$$

And we find $\sigma_1 = 1.5 \cdot 10^{-16} \text{ cm}^2$ at 500 nm.

The two-photon absorption cross-section σ_2 was calculated by Palczewska *et al.*⁵¹: $\sigma_2 = 10^{-50} \text{ cm}^4\text{s}$. The pulses characteristics are detailed in Table 3.1.

The intensity is calculated as $I = \frac{\text{Number of Photons}}{A \cdot \Delta T}$. Note that this equa-

	Single Photon	Two Photon
Pulse Duration $\Delta T(\text{s})$	10^{-13}	10^{-13}
Diameter (μm)	100	100
Area $A(\text{cm}^2)$	$7.85 \cdot 10^{-5}$	$7.85 \cdot 10^{-5}$
Energy (J)	$8 \cdot 10^{-12}$	$4 \cdot 10^{-7}$
Number of Photons	$1.9 \cdot 10^7$	$1.9 \cdot 10^{12}$
$\sigma_1 I \sigma_2 I^2$	$3.7 \cdot 10^8$	$6.06 \cdot 10^8$

Table 3.1: Pulses characteristics used in *ex-vivo* experiment.

tion assumes that the pulse is squared, instead of Gaussian. We found $\sigma_1 I = 3.7 \cdot 10^8$ and $\sigma_2 I^2 = 6.06 \cdot 10^8$ for single and two-photon absorption respectively. Therefore, the pulses used for each experiment isomerizes almost the same number of molecules, considering they illuminates the same number of rhodopsin, inducing therefore the same B-wave amplitude. Note

that this simplified approach does not take in account that the process could be single photon absorption from the tail of the rhodopsin absorption spectrum. This direct infrared absorption was ruled out by Palczewska *et al.*⁵¹, where they determined that, using *ex-vivo* system, the ERG upon infrared femtosecond light (from 800 nm) is generated from two-photon absorption processes.

In conclusion, we used infrared femtosecond light to generate an ERG in *ex-vivo* system. All the evidence tends to show that this is a two-photon process. In fact, all the dependence on the parameters (energy, pulse duration and beam diameter) are consistent with such an excitation mechanism. Moreover, the simple calculation of excitation probability using cross-section from the literature is fully consistent with the ERG we observed. Finally, this assessment allows us to conclude that the excitation settings are compatible with the maintain of the physiological response over long term.

Chapter 4

In-vivo experiments

This chapter focuses on the experiments carried out *in-vivo*, *i.e.*, in living anaesthetized mice. In a first part, we measured the energy response of cones and rods combining visible excitation light and genetically modified mice. We also replicated the energy response upon two-photon absorption already measured *ex-vivo* and went one step further, using shaped infrared pulses (π -step in the spectral phase). In a second part, we carried out intra-pulse and multi-pulse coherent control in living mice.

4.1 Light energy response of the retina using an ERG

In the series of measurements described in this section, first we characterized the response of the retina as a function of the energy for different photoreceptors. These measurements relied on the use of genetically modified mice, as explained in subsection 1.2.5. The aim was to identify which energy level is necessary to excite the rods without saturating the response and without having any contribution from the cones. A measurement consists in sequentially increasing and decreasing the energy, and compare the two curves, to obtain information regarding bleaching and damage to the retina. In these traces, both curves were similar. In Figure 4.1, we show the A-wave (top) and B-wave (bottom) amplitude as a function of pulse energy at 535 nm. We can see the following characteristic:

- The A-wave in the trace of the genetically modified mice $\text{Rho}^{\text{del/del}}$ is negligibly small over the entire energy range, while the B-wave starts rising after 3 nJ per pulse.
- The response curve of the genetically modified mice $\text{Rho}^{\text{del/wt}}, \text{Opn1mw}^{\text{del/Y}}$

and $\text{Opn1mw}^{wt/Y}$ are similar, as they all possess the rods. Note that $\text{Opn1mw}^{delt/Y}$ exhibits the same signal, even so it does not possess cone, indicating a response dominated by the rods.

- At 3 nJ (the limit at which the cones' response is measurable in our setup), the B-wave is saturated. The A-wave saturates above 20 nJ.

4.1. LIGHT ENERGY RESPONSE OF THE RETINA USING AN ERG67

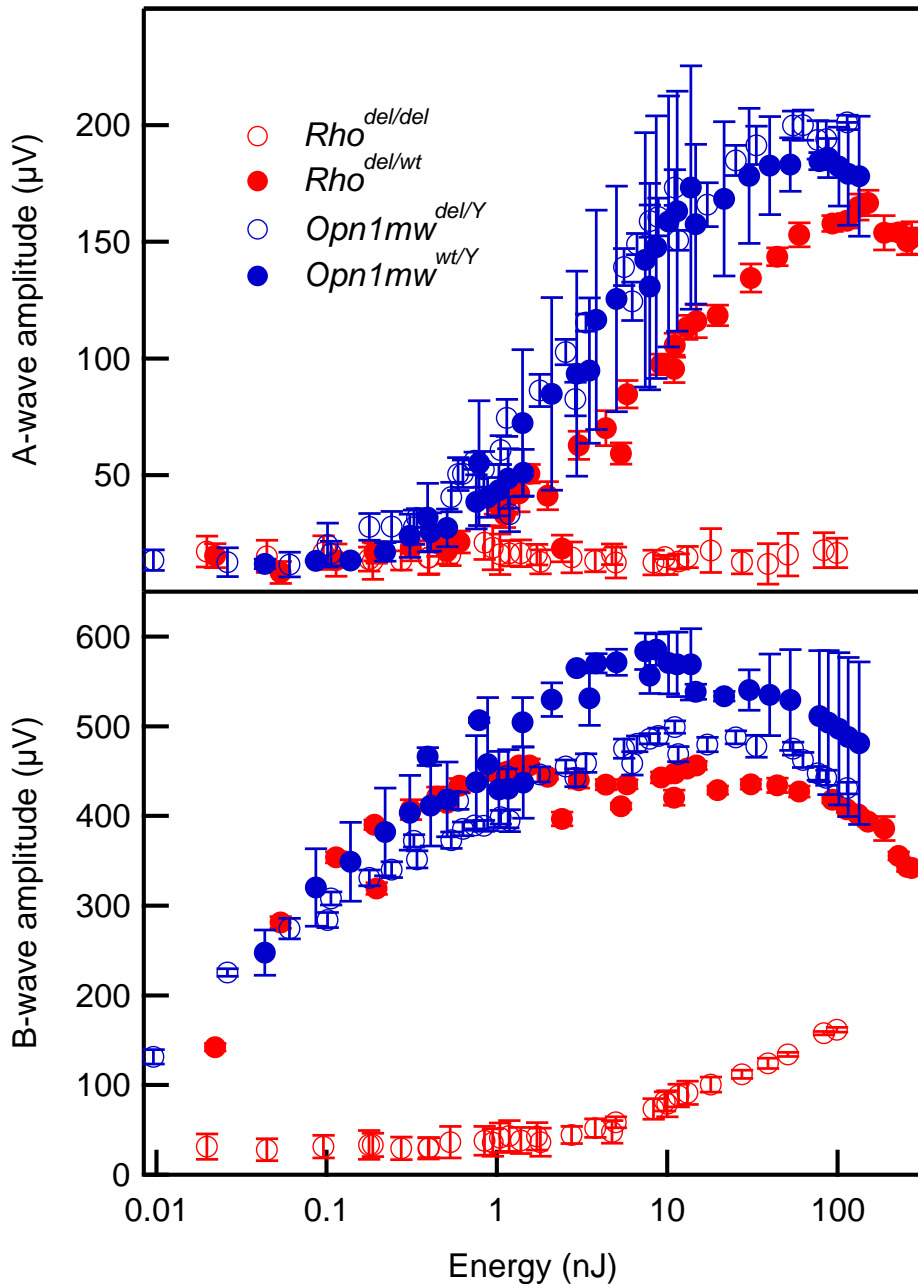


Figure 4.1: Top: A-wave amplitude as a function of the energy per pulse for different mice's genome. Bottom: B-wave amplitude as a function of the energy per pulse for different mice's genome. The number of animals used is $n=2$ for all genome, except $Opn1mw^{del/Y}$, where $n=1$. The contact lens electrode was used for this measurement.

These results ensure that wild type mice can be used to probe the response of rhodopsin as long as the energy per pulse is kept below 3nJ. Indeed, only signal coming from rhodopsin is measured below this threshold, and the A-wave is not saturated. On the other hand, any measurement related to the B-wave becomes more complicated, as the response curve is already saturated at 3 nJ.

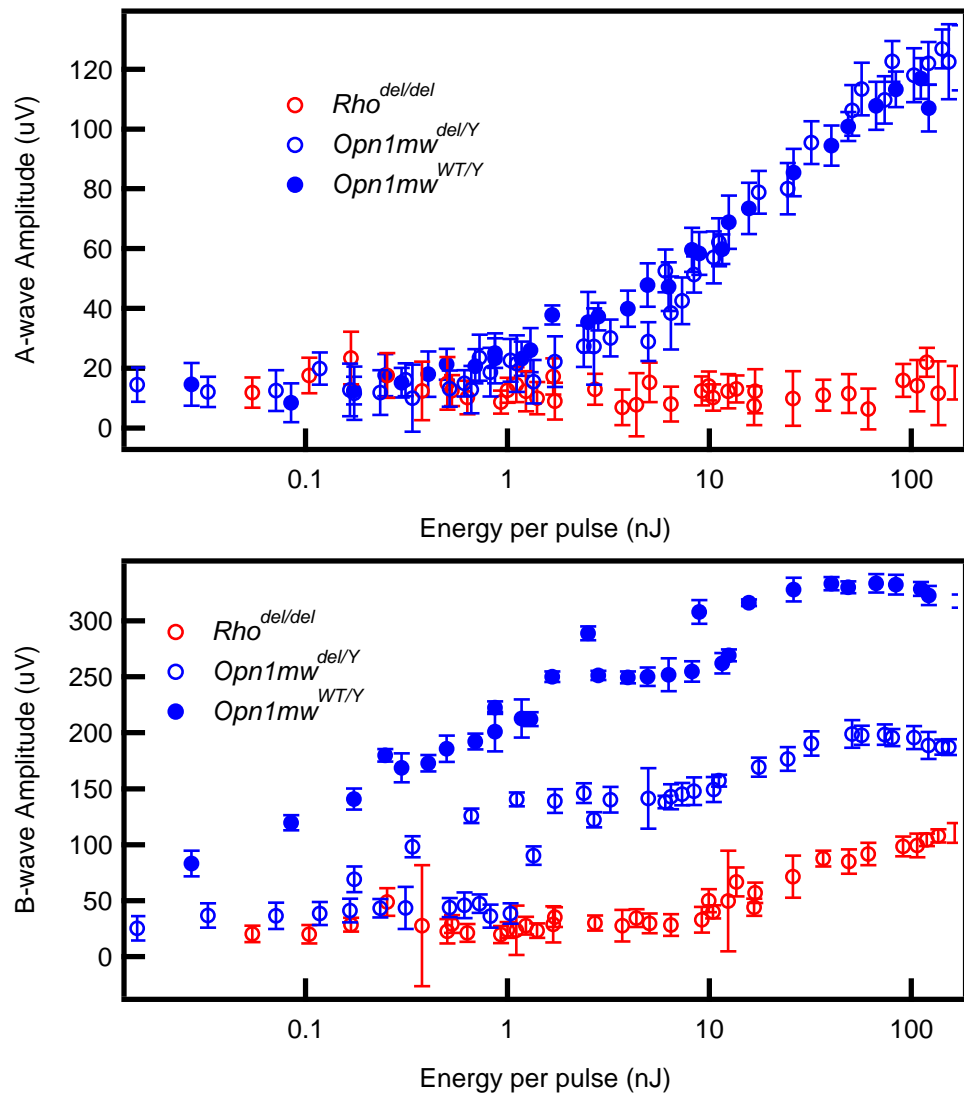


Figure 4.2: Top: A-wave amplitude as a function of the energy per pulse for different mice's genome. Bottom: B-wave amplitude as a function of the energy per pulse for different mice's genome. $n=1$ for all genome. Copper ring electrodes was used for this measurement.

These results obtained with contact lens electrodes were also confirmed using copper wire ring electrodes, as displayed in Figure 4.1. The signal measured with the copper ring is lower, even in absence of index matcher (not shown). This is due to the position of the electrode: the electrode lens features a thin silver lead at the apex of the eye, where the measurable signal is stronger compared to the periphery of the eye.

We explain the difference between $\text{Opn1mw}^{del/Y}$ and $\text{Opn1mw}^{WT/Y}$ by variations associated to the small number of independent measurements. Indeed, the anaesthesia influences greatly the absolute value of the signal⁵⁴, as well as the contact between the electrode and the cornea (change of impedance). As the anaesthesia is deepened, the B-wave disappear first, then the A-wave. This explains why the A-wave amplitude is similar in both genome, but the B-wave is smaller in the first one. This is also a good argument in favour of the choice of the A-wave as observable.

We notice that the signal measured with the lens electrode is also more stable shot-to-shot than the signal measured with the copper ring electrode. Changing the copper electrode to platinum electrode did not improve the signal value nor its stability.

4.2 Two-photon absorption control

In this section, we replicate the measurement upon two-photon absorption already performed *ex-vivo*. Successively, we use spectrally shaped pulses (π -step in the spectral phase) to modify the two-photon absorption.

4.2.1 Two-photon energy dependence

The pulse energy is freely adjusted by a combination of a motorized half wave plate and a polariser. A typical one-photon (at 480 nm, obtained using the SHG of the infrared pulse) and two-photon ERG curves are shown in Figure 4.3.

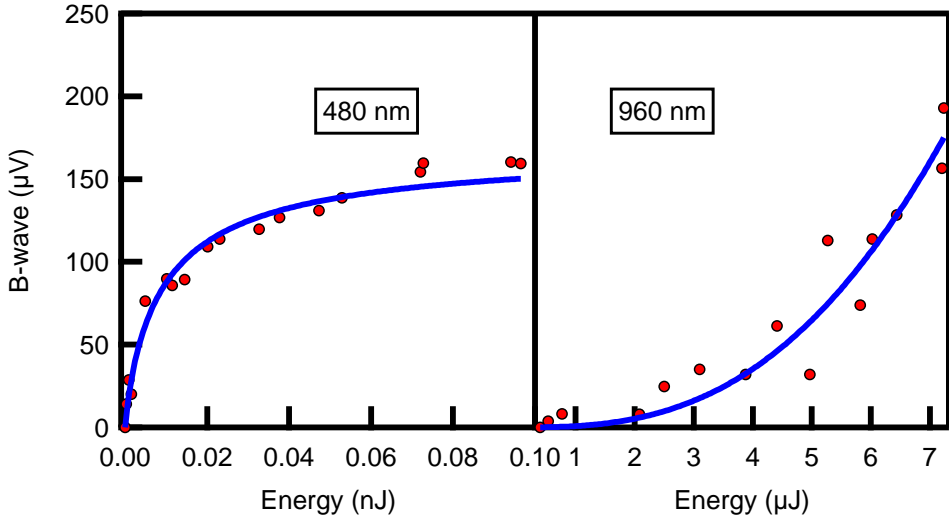


Figure 4.3: Left: one-photon B-wave response *in-vivo* upon 480 nm excitation. Right: two-photon B-wave response *in-vivo* upon 960 nm excitation. Blue line: spline interpolation.

Note that the saturation levels of the B-wave are not the same under the two excitation. The B-wave in the two-photon response does not even come to a saturation for the energy levels tested. Unlike the *ex-vivo* system, this cannot be ascribed to the absence of RPE, not recycling rhodopsin. However, the amount of anesthesia^{55;56} and the temperature of the mice⁵⁷ are both known to affect the values of the A and B-waves.

The energy required to obtain a signal is on average ten times greater *in-vivo* than *ex-vivo*. This is due to better signal to noise ratio (no hindrance by the electro-physiological response from the mouse itself, as the signal background induced by the respiratory motion). However, because the retina is not in its natural environment, the *ex-vivo* response is drastically reduced as compared to the *in-vivo*, leading to an an approximately ten-fold weaker signal.

The rate $\sigma_1 I$ and $\sigma_2 I^2$ (from Equation 3.1 and Equation 3.2) should now be re-calculated, as the energy is increased, and as the absorption of the eye component itself in the infrared should be taken in account. As previously, we use the literature values $\sigma_1 = 1.5 \cdot 10^{-16} \text{ cm}^2$ and $\sigma_2 = 10^{-50} \text{ cm}^4 \text{s}$ for one and two-photon absorption (see section 3.2). We consider the absorption coefficient of water, measured by Hale *et al.*⁵⁸ at 475 nm and 960 nm are respectively 0.000247 and 0.42 cm^{-1} . Considering the size of the eye of a mouse (3mm in diameter⁵⁹), and using the Beer-Lambert Law, the transmis-

sion of the eye (assuming the absorption coefficient of water) is $T = 1.0$ and $T = 0.88$, for 475 and 960 nm respectively. All the parameters are resumed in the Table 4.1.

	Single Photon	Two Photon
Pulse Duration $\Delta T(\text{s})$	10^{-13}	10^{-13}
Diameter (μm)	100	100
Area $A(\text{cm}^2)$	$7.85 \cdot 10^{-5}$	$7.85 \cdot 10^{-5}$
Energy (J)	$8 \cdot 10^{-11}$	$4 \cdot 10^{-6}$
Number of Photons	$1.9 \cdot 10^8$	$1.9 \cdot 10^{13}$
Transmittance	1.0	0.88
$\sigma_1 I \mid \sigma_2 I^2$	$3.7 \cdot 10^9$	$4.71 \cdot 10^{10}$

Table 4.1: Pulses characteristics used in two-photon absorption *in-vivo* experiment.

We found $\sigma_1 I = 3.7 \cdot 10^9$ and $\sigma_2 I^2 = 4.71 \cdot 10^{10}$ for single and two-photon absorption respectively. The one order of magnitude difference may come from the dispersion and the influence of the various physiological parameters on the ERG.

4.2.2 Influence of a π -phase step in the spectral phase on the response of rhodopsin

In this part, we would like to probe the effect of the spectral phase on the two-photon retinal response. In order to modify the spectral phase of an infrared pulse, we use the set-up described in section 2.2.

The experiment is carried out in two steps on rhodamine 6G and on living mice:

1. Reduce the pulse duration using a genetic algorithm.
2. Scan the π -phase step jumps along the spectrum, and measure the response.

We use a genetic algorithm⁴³ to reduce the pulse duration, as the dispersion is not only of second order, due to the generation process. Briefly, sixteen phase functions are applied to the pulse, and the fluorescence of the rhodamine is measured for each of them. By optimally mixing the phase functions (using the genetic algorithm), we can reduce the pulse duration to its minimum. In the second part, we apply a pi phase-step: the phase of the blue part of

the spectrum is unchanged, while the phase of the red part of the spectrum is set at π . We then scan the position of the step. The result of this scan on rhodamine 6G with a temporally compressed pulse and an unoptimized pulse is shown in Figure 4.4.

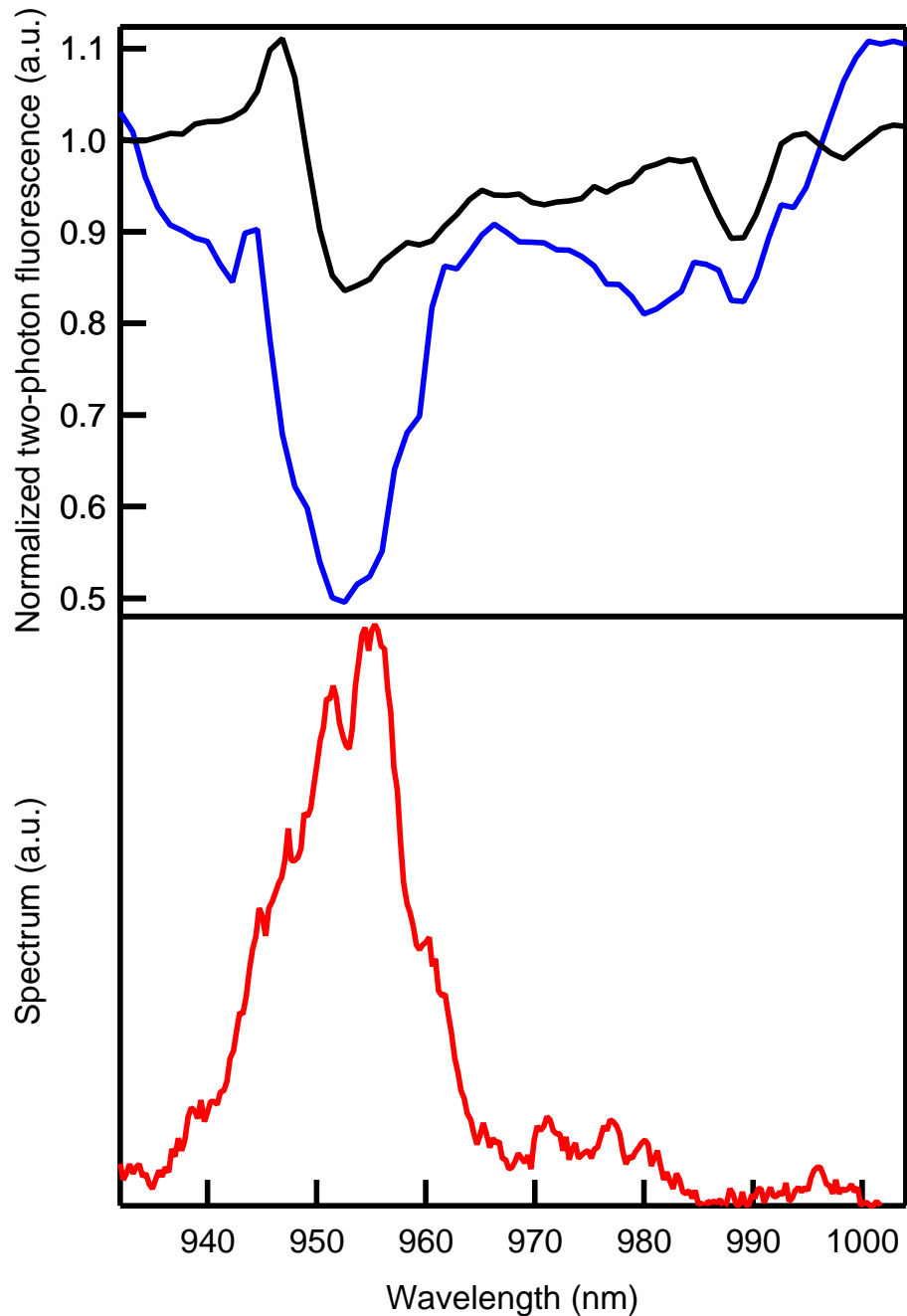


Figure 4.4: Top: Effect of a pi-step phase on the rhodamine fluorescence, with uncompressed beam (black) and optimized beam (blue). Bottom: laser spectrum (red).

The normalized two-photon excited fluorescence presents the lowest intensity

value when the π -step is located at the center of the laser spectrum. When a compressed pulse is used, the difference in fluorescence with or without steps is even greater (Figure 4.4, black and blue curve). Note that fluorescence is normalized to the average fluorescence acquired when the π -step is located before 936 nm.

These observations are consistent with what was previously observed for π -step scans on molecules with large absorption bands (Coumarin 6H⁶⁰), and the physics will be discussed more in details in the subsection 4.2.3.

The same procedure is now performed on mice.

An ERG is measured every 2 seconds from 5 pulses. Every 2 ERGs, the π -phase step is moved by a few pixels (10 pixels, 2.3 nm for mouse 1, 15 pixels, 3.4 nm for mouse 2) on the pulse shaper. The amplitude of the B-wave is averaged for the two ERGs, then on the total number of scans performed (Between 9 and 15). This procedure takes approximately 45 minutes, and is repeated 3 times, with an anaesthesia between each measurement. The total average for each mouse is shown in Figure 4.5.

Note that here we decided to use the B-wave as observable, as the A-wave is now almost non-existent, while the B-wave is not saturated. Indeed, as shown in Figure 4.3, the energy involved *in-vivo* is not sufficient to saturate the B-wave. Moreover, as shown in Figure 4.1 using visible excitation, at energies where the B-wave is not saturated, the A-wave is relatively small.

We observe the same trend as rhodamine. When the π phase-step is located at the center of the pulse spectrum, the response is weaker. However, while the response decreased by about 50% for rhodamine, it only decreased by 10 to 15% in the eye of the mouse. The comparison with the theory is done in the next paragraph.

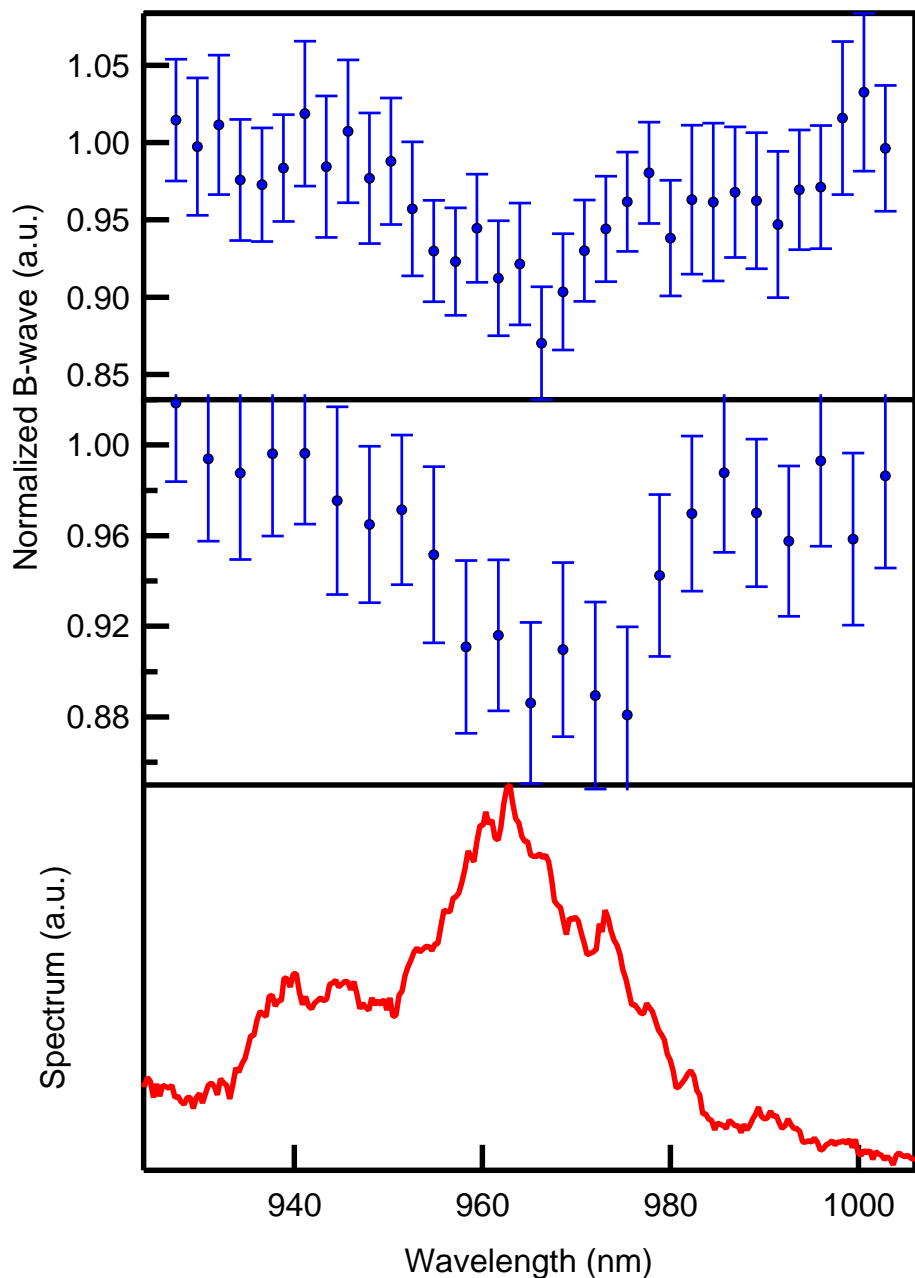


Figure 4.5: Top: Pi-phase step experiment on one mouse. Middle: Pi-phase step experiment on another mouse. Bottom: spectrum of the infrared beam. The error bars represents the standard error of the mean.

4.2.3 Calculation of the influence of the π -phase step upon two-photon absorption

The phenomenon observed in subsection 4.2.2 can be explained by calculating the intensity profile $I(t)$ of a pulse depending on the location of the step. In a first step, we can generate a pulse centred at 960 nm, with a 20 nm bandwidth with a step-phase of π in the center. The time profile of such a pulse is shown in red in the Figure 4.6, top part, while the time profile of a Fourier-limited pulse is shown in blue. We observe that the center of the pulse disappears, because of destructive interference.

Because our measurement involve a two-photon absorption process, we proceed in calculating the squared intensity of the pulse, and then integrating it over the time (800 fs). By repeating this procedure for π phase-steps located between 920 and 1000 nm, every 4 nm, and by normalizing with respect to a Fourier limited pulse, we obtain the trace in the Figure 4.6, bottom part.

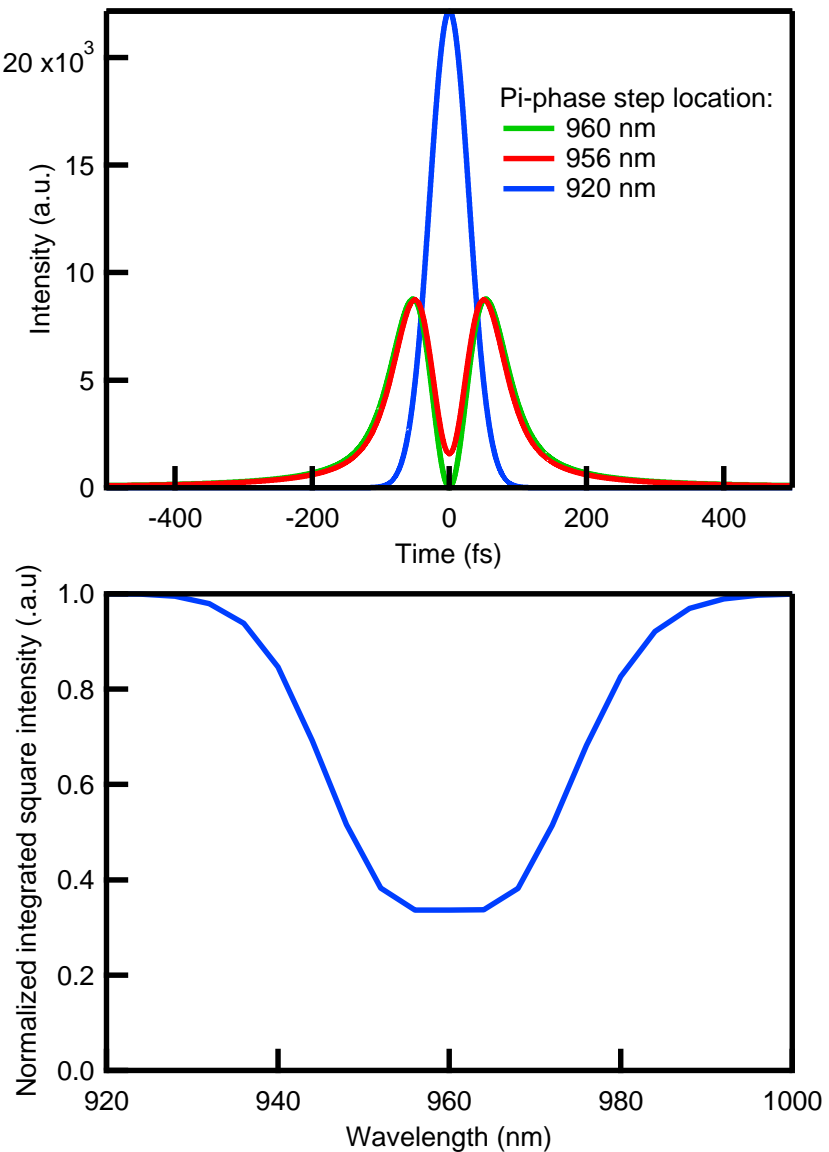


Figure 4.6: Top: Simulated temporal profile of gaussian beam with a pi-phase step at various location. Bottom: Normalized integrated squared intensity of Gaussian pulses as a function of the pi phase-step location.

As expected, the two-photon absorption decreases drastically when the location of the pi phase-step is at the center of the pulse. The spectral phase modulation therefore corresponds in this case to an intensity modulation. We can thus reduce the absorption with two photons by 70% this way. We see in the Figure 4.4 that only 50% of the fluorescence was suppressed. This

is due to the non-Gaussian, asymmetric shape of the spectrum.

The effect is different if the system used has broad or narrow absorption bands compared to the pulse spectrum, as demonstrated by Meshulach et al.^{60;61}. For a narrow-band absorption spectrum (comparatively to the pulse bandwidth), the fluorescence can be completely cancelled, except when the pi phase-step is located exactly at the center, and the fluorescence is at maximum again, even though the pulse intensity is lower, and the pulse duration longer than the Fourier-limited pulse. This is due to the self-interference between the pulses during the absorption. Indeed, even though the spectrum of the electric field remain constant over the whole scan (as it should, because the pulse shaping is phase-only), the Fourier transform of the squared electric field is greatly modified, as shown in Figure 4.7. The interference is constructive at twice the central wavelength of the pulse, and destructive in the rest of the spectrum. This leads to the same two-photon absorption efficiency as an unshaped pulse, as shown in the Figure 4.8, in which Meshulach et al.⁶⁰ performed the experiment in Cesium gas. Indeed, as the pi-phase step is closer to the central wavelength, the central wavelength is depleted. Only the wings of the spectrum can therefore be absorbed by two-photon absorption. However, very close to the center, the central wavelength is now constructive, and the fluorescence increases again.

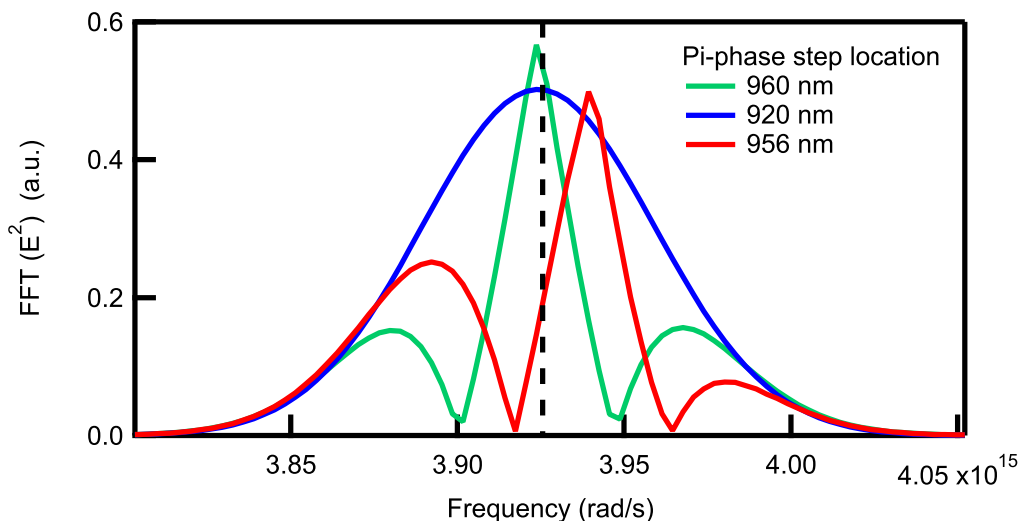


Figure 4.7: Simulated FFT of E^2 for various pi-phase step location, demonstrating the constructive interference for the central wavelength $\lambda_0 = 960$ nm, $\Delta\lambda = 20$ nm. The vertical dash bar is located at the frequency corresponding to $\lambda = 480$ nm.

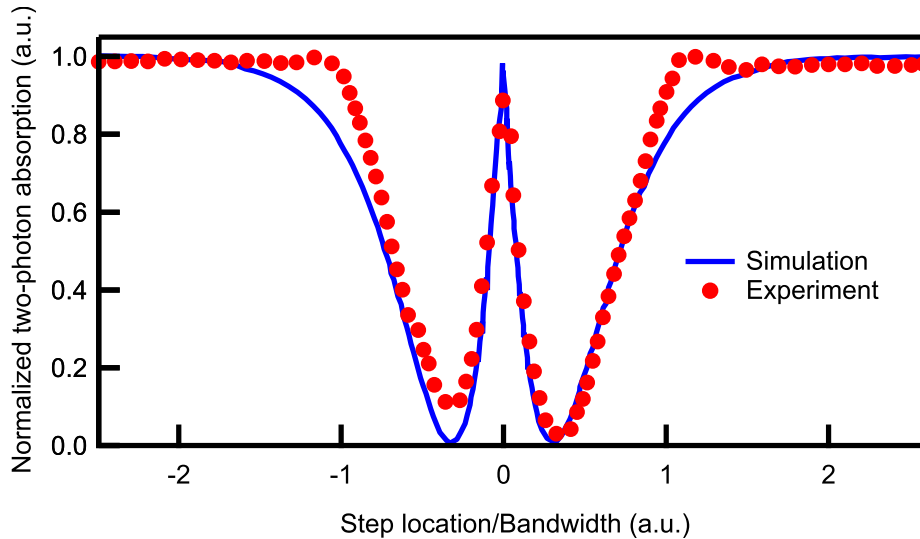


Figure 4.8: Two photon absorption as a function of the pi-phase step location for a narrowband absorption. Blue: simulated data. Red: Experimental data in Cesium. Figure adapted from Silberberg.⁶¹

This effect is obviously not applicable in system with broad absorption bands, because all the spectrum can efficiently absorb two-photon. Therefore, only the intensity of the pulse is needed to explain the observed process here, and not the phase. Regarding the experiment on mice, we see that the decrease is only 10 to 15%, compared to the experiment in rhodamine, where a 50% decreased was observed. This question remains unanswered.

4.3 Intra-pulse coherent control of vision

In this section, we will show that the spectral phase allows us to modulate the response of the retina. The experimental results are supported by rate equations and ab initio calculations.

The retina is commonly known to respond only to the energy of light, *i.e.*, the number of photons^{62;63} and to the frequency of the said photons. However, previous experiments in solution demonstrated that the rhodopsin's response can be controlled by femtosecond laser (see subsection 1.2.3). These experiments demonstrate that the phase of light plays a role in the isomerization, and that coherence is maintained in this protein in solution. In our experiment, we applied, on the retina, positive and negative chirped laser pulses with 535 nm central wavelength as described in (section 2.3, and we measured the response of the retina.

4.3.1 Measurement of the pulses used in the experiment

We show in Figure 4.9 the spectra corresponding to the 5 phase functions tested in this experiment (FWHM = 30 nm). The corresponding linear chirps are: -2800, -1400, 300, 1300 and 3100 fs^2 . The autocorrelations are shown in Figure 4.10. The experiment is carried out at two different energies.

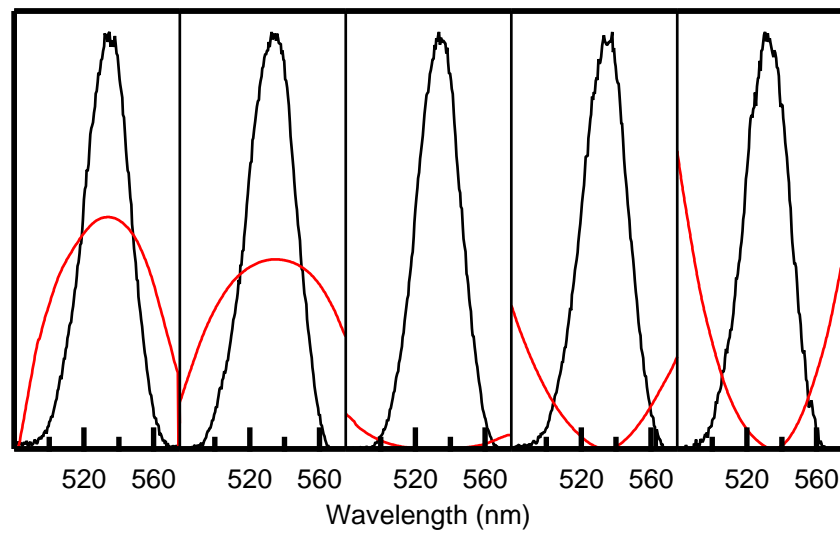


Figure 4.9: Spectrum integrated (black) and phase retrieved (red) from the FROG measurement for each phase function.

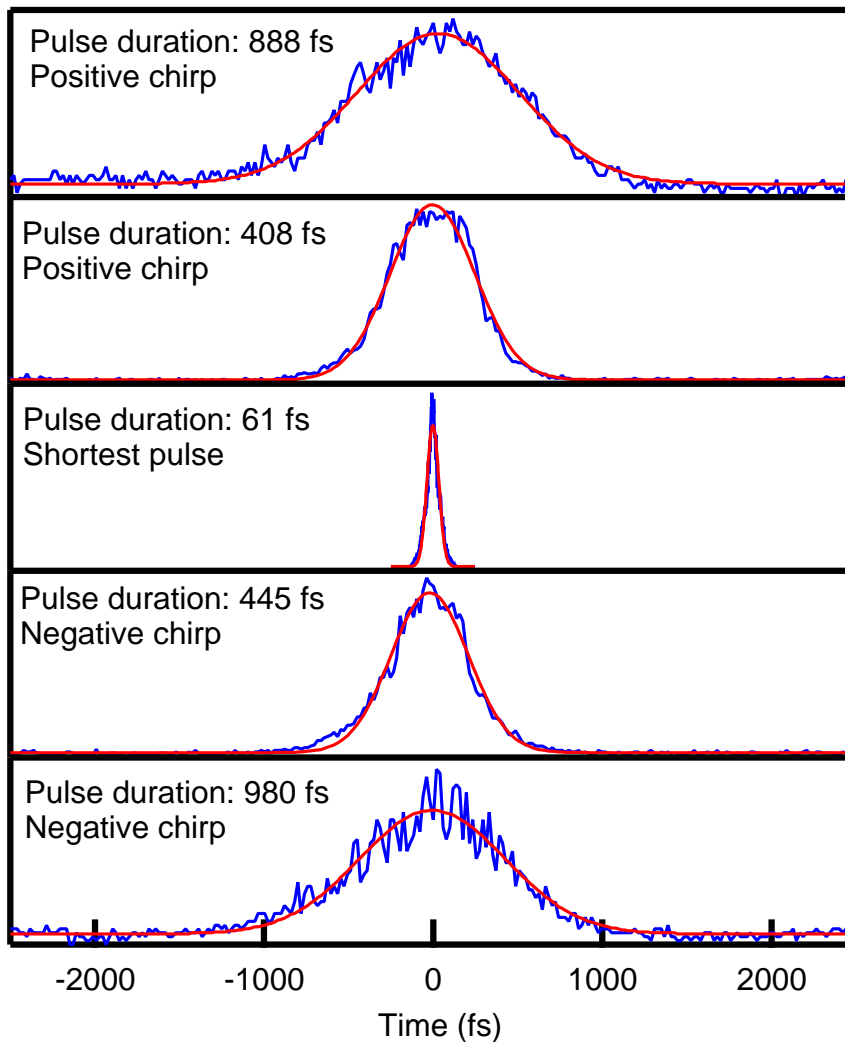


Figure 4.10: Autocorrelation of the five pulses used in the experiment.

4.3.2 Pulse duration dependence

The datasets presented here were obtained under the following conditions. Each experimental session corresponds to 45 minutes corresponding to the duration of the effect of anaesthesia on the animal (see subsection 2.5.2). Since we acquire a curve every two seconds, each dataset comprises 1000 to 1400 ERG. Since there are 5 different phase functions, there are therefore between 200 and 280 ERG per phase function.

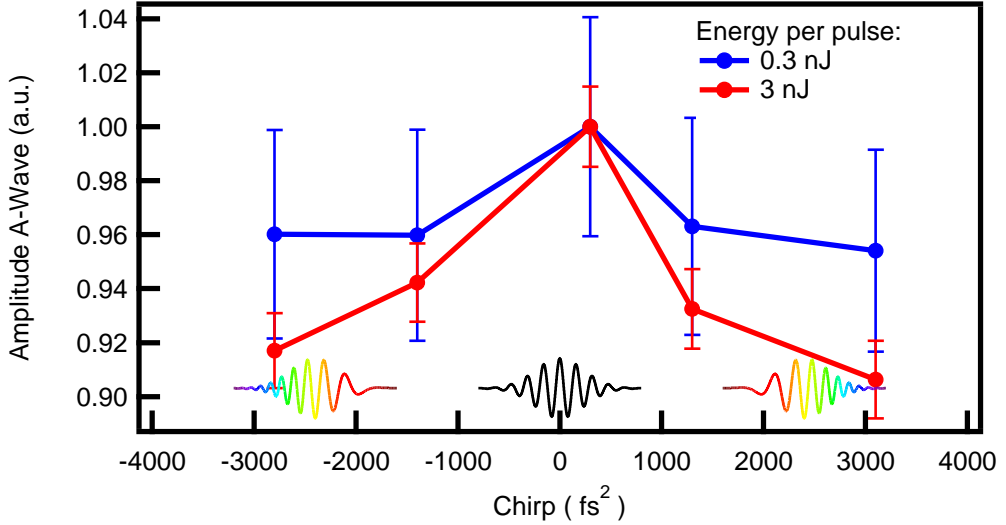


Figure 4.11: Intra-pulse control of the first step of the vision process. Measured normalized A-wave amplitude extracted from the ERG signal for five values of the pulse chirp (with $\frac{d^2\phi}{d\omega^2} = -2800, -1400, 300, + 1300, \text{ and } + 3100 \text{ fs}^2/\text{rad}$), modulating the ordering and delays of the frequencies in the pulse (linear chirp) and for two pulses energies (0.3 and 3 nJ).

Figure 4.11 shows the dependence of the A-wave in living mice on the phase function, and accordingly on the pulse duration.

Data are normalized to the maximum values corresponding to the shortest pulse. The results shown for the 3 nJ case is the average over 7 animals (11 data sets of 45 min), while the experiment at 0.3 nJ is the average over the results on 4 animals (7 data sets of 45 min). The error bars in all experimental plots correspond to the standard error of the mean.

For the high energy measurements, the p-value calculated between the shortest pulse and the other conditions is always below 10^{-10} . For the low energy measurements, the p-value between the shortest pulse and the other conditions is always below 0.09, except for the point at $+1300 \text{ fs}^2$. ($p=0.21$). All the p-value calculated by a T-test are displayed in Table 4.2 and Table 4.3.

Chirp (fs ² /rad)	-2800	-1400	300	1300	3100
-2800	0	0.0415	1.7437e-17	0.2721	0.0936
-1400	0.0415	0	1.0678e-10	0.3242	2.7077e-04
300	1.7437e-17	1.0678e-10	0	1.3132e-13	1.2607e-22
1300	0.2721	0.3242	1.3132e-13	0	0.0074
3100	0.0936	2.7077e-04	1.2607e-22	0.0074	0

Table 4.2: Ttest Wave A High Energy

Chirp (fs ² /rad)	-2800	-1400	300	1300	3100
-2800	0	0.7659	0.0985	0.6806	0.7677
-1400	0.7659	0	0.0567	0.4700	0.9738
300	0.0985	0.0567	0	0.2128	0.0360
1300	0.6806	0.4700	0.2128	0	0.4603
3100	0.7677	0.9738	0.0360	0.4603	0

Table 4.3: Ttest Wave A Low Energy

The A-wave amplitude, which is related to the number of isomerized rhodopsin, is clearly maximized for the flat phase, *i.e.*, $\frac{d^2\phi}{d\omega^2} = 300$ fs²/rad, while both negative and positive chirp functions reduce the eye response.

These results reveal that the rhodopsin-mediated retina response is sensitive to the spectral phase of light pulses as short as 50 fs. In particular, the eye sensitivity is highest when the wavelength all are ordered such that the pulse is the shortest. Unexpectedly, the associated higher instantaneous intensity does not produce a decrease of the retina response, as expected for non-linear effects such as saturation or excited state absorption in a higher lying state S_n^{6;64}. On the contrary, short pulses yield the maximal photo-isomerization. We will try first to provide an intuitive explanation of our results, which will be further supported by numerical studies.

In subsection 1.2.3, and particularly in connection to Figure 1.15, we explained that, *in vitro*, Smitienko et al.³³ demonstrated a scheme for reversing the isomerization of rhodopsin. They used two lasers, one delayed with respect to the other by 5 ps, and showed that it is possible to reverse the rhodopsin isomerization to its cis-ground state. In this experiment, we show that it is possible, by the same mechanism, to reverse the isomerization using a single pulse. In fact, the longer the pulse duration, the easier it let the rhodopsin switch back to its 11-cis configuration. This can be achieved by two

pathways: stimulated emission before the conical intersection of re-excitation after the conical intersection. The following conditions are necessary for this phenomenon to occur:

1. The probability that the all-trans rhodopsin absorbs another photon and the probability that the wavepacket returns to the 11-cis configuration must be higher than the probability of 11-cis rhodopsin to absorb a photon.
2. The stimulated emission from the excited 11-cis to the ground state of 11-cis and the absorption of from the all-trans ground state to the all-trans excited state have to be demonstrated *in vivo*, as it is not obvious such effects around a conical intersection could happen in a biological system as complex as the eye.

We also observe that this effect is more pronounced at 3 nJ than at 0.3 nJ. However, we could not increase the energy further as this would lead to a signal coming from the cones, as demonstrated in Figure 4.1.

In the following we will show using rate equations that this interpretation is plausible. It is then confirmed by *ab initio* simulations using the multi-configurational time-dependant Hartree approach performed by the group of Prof. U. Roethlisberger at EPFL.

4.3.3 Rate equations

We first define the states involved in the dynamics, as well as their dynamics, in Figure 4.12. This is an extended version of the rate equations defined by Yan et al.⁶⁵.

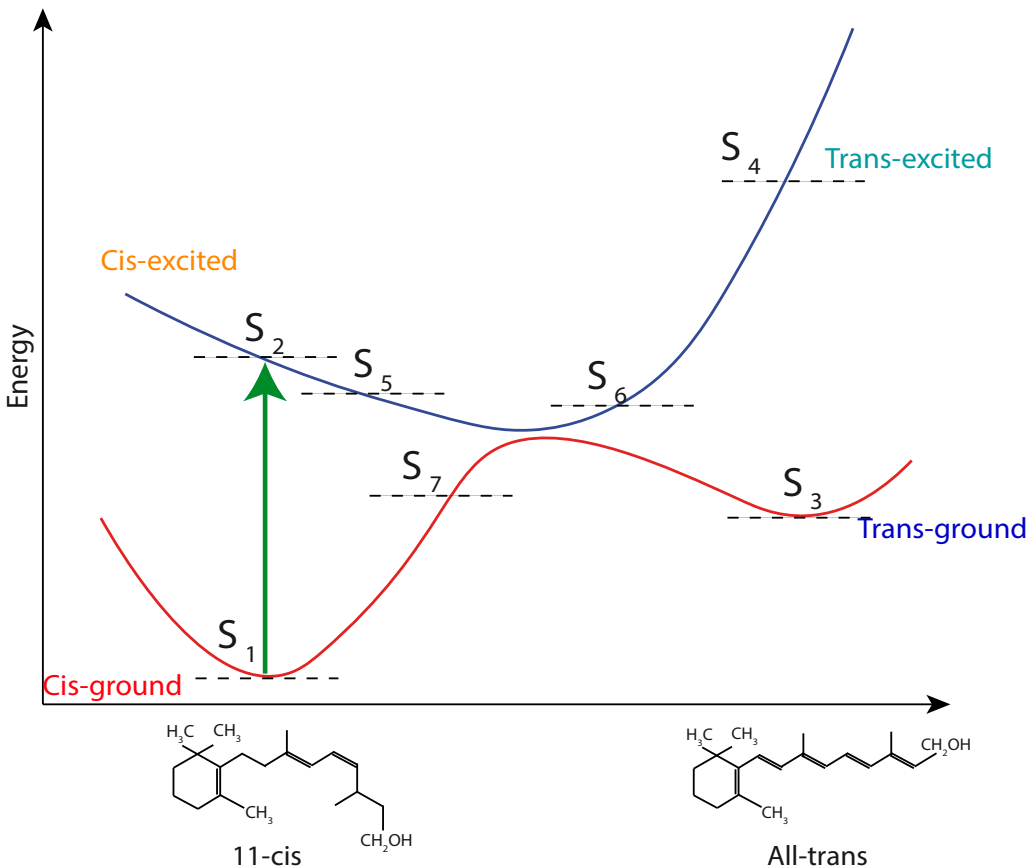


Figure 4.12: Definition of the different step in the dynamics of the rhodopsin intra-pulse control.

The states S_i respectively have a population N_i . S_1 , S_2 , S_3 , and S_4 correspond respectively to the cis-ground, cis-excited, trans-ground, and trans-excited. The processes included in this calculation are:

- the absorption from S_1 to S_2 ,
- the stimulated emission from S_2 to S_1 ,
- the absorption from S_3 to S_4 ,
- the stimulated emission from S_4 to S_3 .

Note that our definition of states here as S_i should not be confused with the

different singlet excited state potential sheets. The rate equations are:

$$\begin{aligned}
 \frac{dN_1}{dt} &= -\sigma_1 N_1 I + \sigma_1 N_2 I + \frac{N_7}{\tau_3} \\
 \frac{dN_2}{dt} &= \sigma_1 N_1 I - \sigma_1 N_2 I - \frac{N_2}{\tau_1} \\
 \frac{dN_3}{dt} &= \eta_1 \frac{N_5}{\tau_2} - \sigma_2 N_3 I + \sigma_2 N_4 I + (1 - \eta_2) \frac{N_6}{\tau_2} \\
 \frac{dN_4}{dt} &= \sigma_2 N_3 I - \sigma_2 N_4 I - \frac{N_4}{\tau_1} \\
 \frac{dN_5}{dt} &= \frac{N_2}{\tau_1} - \frac{N_5}{\tau_2} \\
 \frac{dN_6}{dt} &= \frac{N_4}{\tau_1} - \frac{N_6}{\tau_2} \\
 \frac{dN_7}{dt} &= \eta_2 \frac{N_6}{\tau_2} + (1 - \eta_1) \frac{N_5}{\tau_2} - \frac{N_7}{\tau_3}
 \end{aligned} \tag{4.1}$$

With:

- $\tau_1 = 8$ fs
- $\tau_2 = 192$ fs
- $\tau_3 = 3000$ fs
- $\eta_1 = 0.67$
- $\eta_2 = 0.5$

We assume the population in the state S_2 relaxes in the S_5 location in $\tau_1 = 8$ fs. This fast dynamics was necessary to prevent the stimulated emission after a time τ_1 . Indeed, the pulses used in this experiment are not broadband enough to induce a stimulated emission on a longer time scale, as the wave packet evolves from the cis-excited to the conical intersection. The wavepacket reaches the conical intersection in 80 fs^{5;32}. At t_0 , the more efficient wavelength to dump it down is 500 nm. At 80 fs, it is superior than 800 nm. We therefore make the assumption that there is a stokes shift of 300 nm in 80 fs. As the spectrum of the laser is 30 nm, this corresponds to $\tau_1 = \frac{80 \text{ fs} \cdot 30 \text{ nm}}{300 \text{ nm}} = 8$ fs.

At the conical intersection, the wavepacket splits between S_7 and S_3 . The S_7 state holds the wavepacket for 3 ps, before returning to the cis-ground state S_1 ^{31;65}.

Finally the wavepacket in the trans-excited state (S_4) is first transmitted

to a S_6 state because the pulses used in this experiment are not broadband enough to induce a stimulated emission on a longer time scale, as S_2 decays in S_5 . The time decay is also fixed as τ_1 .

The states S_5 and S_6 could have been joined together if the quantum yield was the same whether the wavepacket originates from the cis-excited or the trans-excited. Because this value cannot be fixed, as the literature value measured/calculated span from 0.15 to 0.5^{66;67;33}, we decided to test the rate equation with a reverse quantum yield $\eta_2 = 0.5$.

The direct quantum yield is known $\eta_1 = 0.63^{5;29}$.

The absorption cross-section for the cis-ground state can be calculated from the molar extinction coefficient ($\epsilon = 40200 \text{ cm}^{-1}\text{M}^{-1}$)⁵³.

$$\sigma = \ln(10) \frac{10^3}{N_A} \epsilon \quad (4.2)$$

And we find $\sigma_1 = 1.5 \cdot 10^{-16} \text{ cm}^2$ at 500 nm.

We now take into account the wavelength dependence of the cross-section, as well as the Gaussian temporal shape of the pulse.

We first generate the Wigner-Ville distribution for each pulse. The Wigner-Ville distribution is a signal analysis method to generate a time-frequency matrix. The Wigner-Ville distribution is calculated from the theoretical electric field. Examples are shown in Figure 4.13 and Figure 4.14.

We then normalize this matrix by the number of photons per cm^2 (for Figure 4.13 and Figure 4.14, $I = 4.4 \cdot 10^{15} \text{ photons/cm}^2$), to which we multiply the absorption spectrum of rhodopsin or photorhodopsin. This produces a vector $A(t) = \sigma(\omega)I(\omega, t)$, which is used in the Equation 4.1. It also has the advantage of taking into account the sign of chirp. This method can also simulate any phase, and therefore any temporal pulse shape.

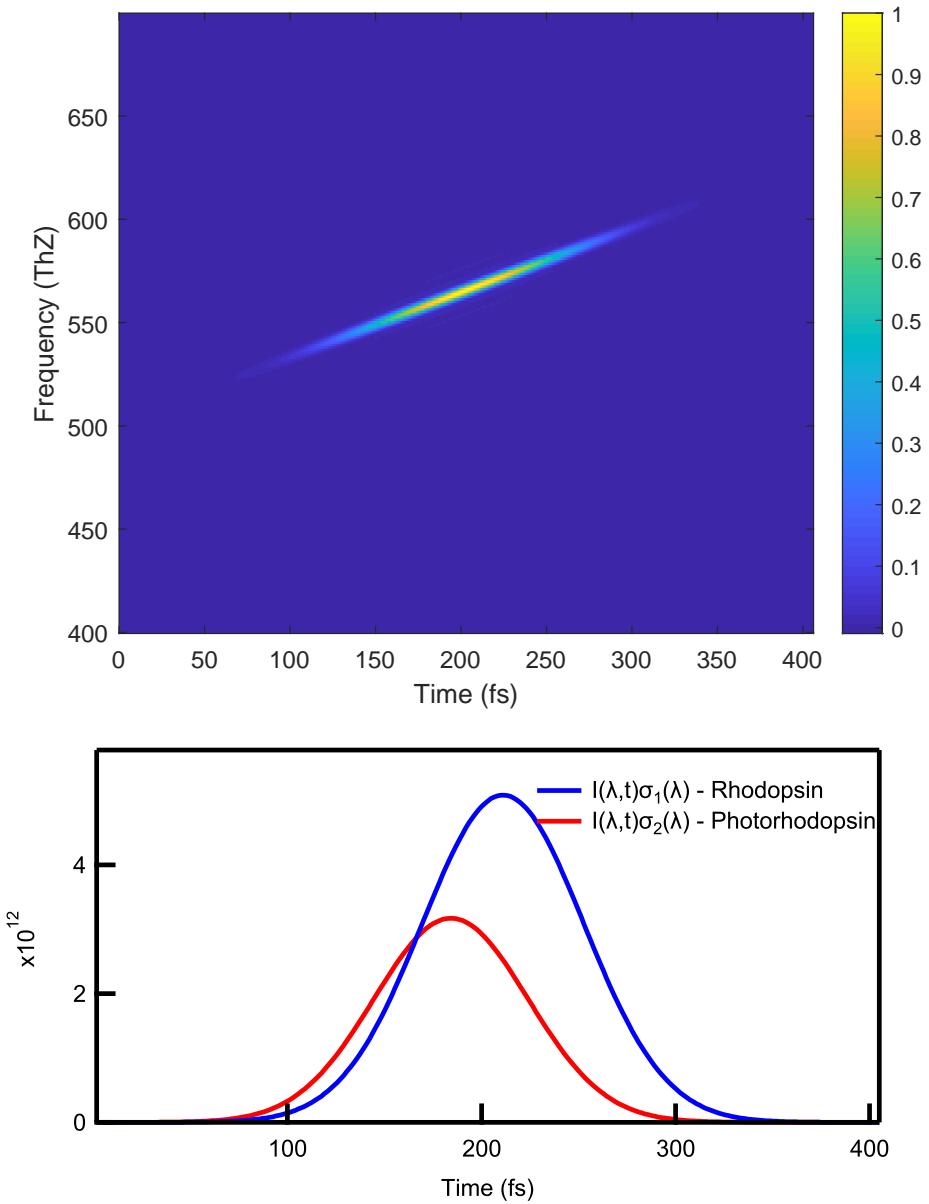


Figure 4.13: Top: Wigner-Ville matrix for a chirp $\frac{d^2\phi}{d\omega^2} = 500 \text{ fs}^2$, $\lambda = 540 \text{ nm}$ and $\Delta\lambda = 30 \text{ nm}$. Bottom: Product of $\sigma(\omega)$ and $I(\omega, t)$ for rhodopsin and photorhodopsin

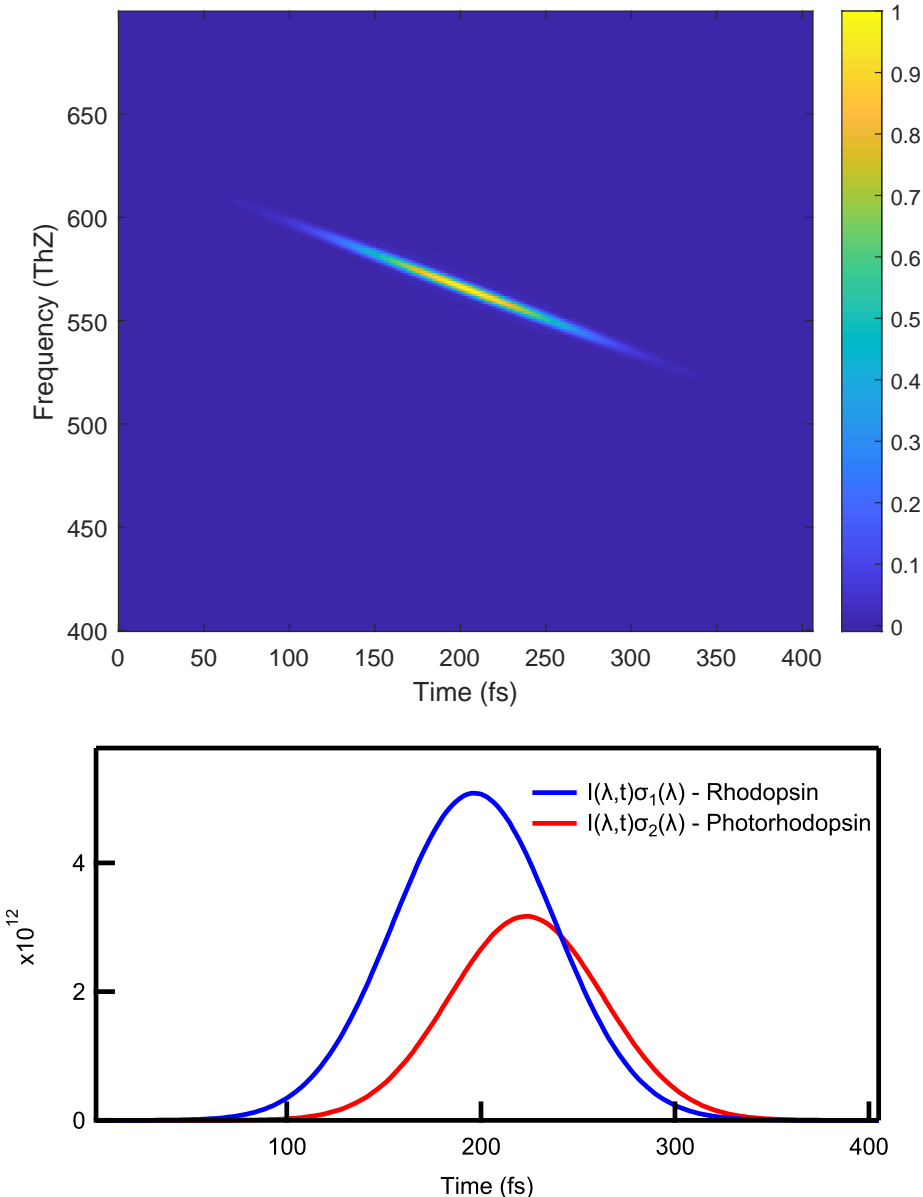


Figure 4.14: Top: Wigner-Ville matrix for a chirp $\frac{d^2\phi}{d\omega^2} = -500 \text{ fs}^2$, $\lambda = 540 \text{ nm}$ and $\Delta\lambda = 30 \text{ nm}$. Bottom: Product of $\sigma(\omega)$ and $I(\omega, t)$ for rhodopsin and photorhodopsin

We already see from these figures that positive and negative chirps produces different effects: with the positive chirp, the maximum probability for rhodopsin to be excited from the cis-ground state to the cis-excited state occurs after the maximum of the probability of transition from the trans-

ground state to the trans-excited state. This is the opposite of what happens with the negative chirp, which should further decrease the number of final rhodopsins in the trans-ground state.

We solve the Equation 4.1 system numerically for pulse durations ranging from 50 to 1000 fs, with a positive or negative chirp. We then perform a parametric study with the following parameters independently: the number of photons (Figure 4.15), the reverse quantum yield η_2 (Figure 4.16) and the allowed stimulated emission time τ_1 (Figure 4.17).

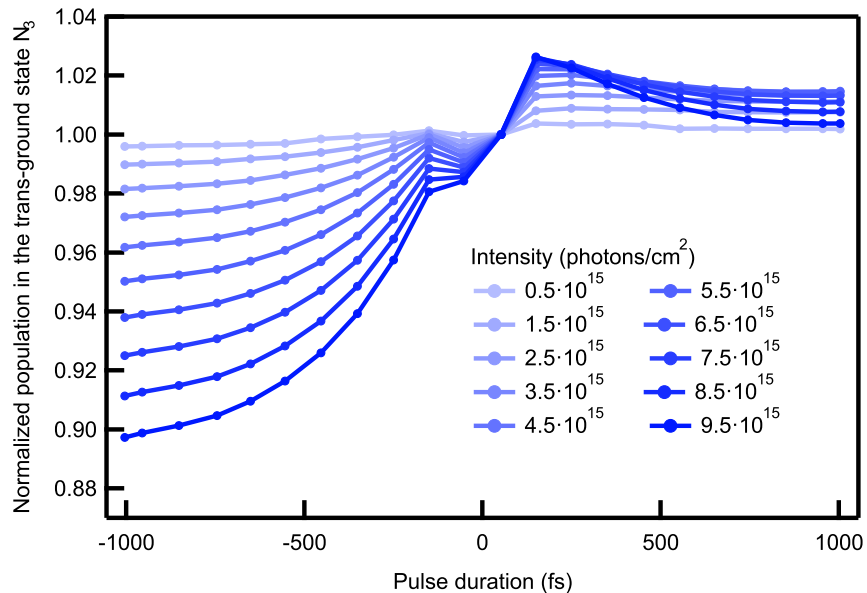


Figure 4.15: Normalized population of the trans-ground state N_3 after 20 ps, while varying the number of photons/cm².

The number of photons/cm² in the eye is calculated as:

$$\frac{N}{A} = \frac{hc}{\lambda A} = 2.5 \cdot 10^{13} \text{ photons/cm}^2 \quad (4.3)$$

Where the spot radius on the eye was set to 100 μm (FWHM approximation from Figure 2.10). If the radius is decreased to 20 μm (i.e. without index matcher), then the number of photons/cm² increases to $6.4 \cdot 10^{14}$ photons/cm².

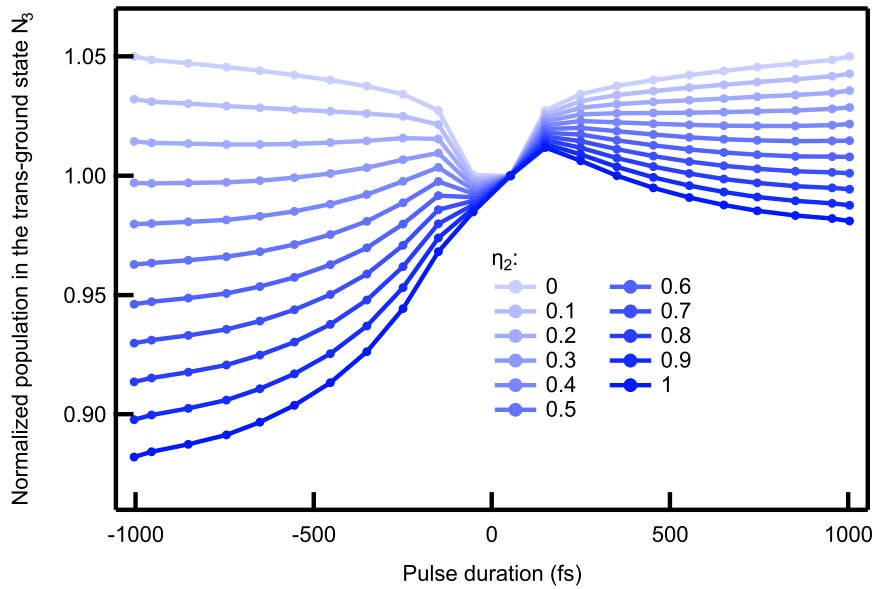


Figure 4.16: Normalized population of the trans-ground state N_3 after 20 ps, while varying the reverse quantum yield η_2 .

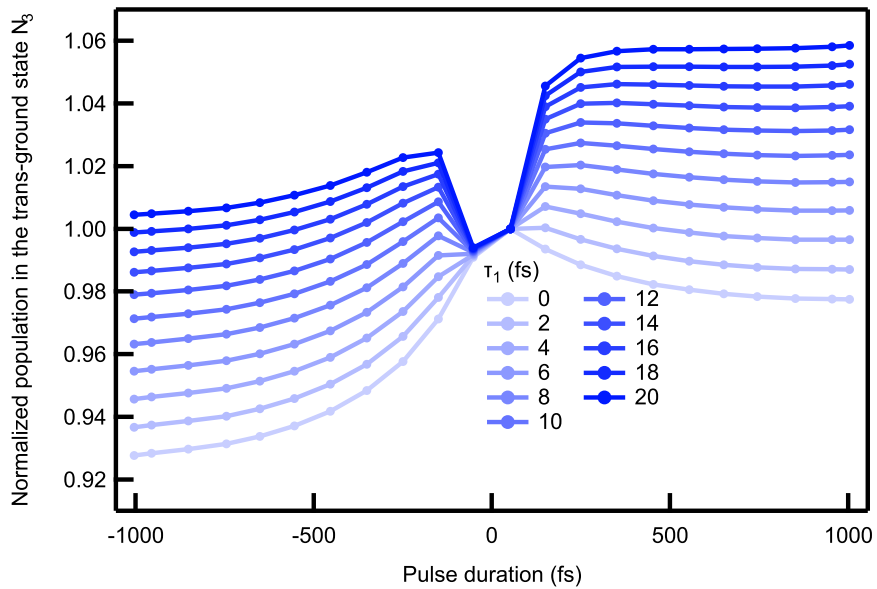


Figure 4.17: Normalized population of the trans-ground state N_3 after 20 ps, while varying the allowed stimulated emission time τ_1 .

From the Figure 4.15, we can say that increasing the number of photons/cm²

accentuates the difference between a short pulse and a long pulse.

From the Figure 4.16, we can say that if the reverse quantum yield increases, then the difference between a long pulse and a short pulse is also accentuated. However, the longer pulse becomes more effective if $\eta_2 < 0.8$ for positive chirp and $\eta_2 < 0.5$ for negative chirp. From the Figure 4.17, we see that if it is possible to induce stimulated emission from the cis-excited to cis-ground state (and to a lesser extent from the trans-excited to trans-ground state) for longer times, then the difference between shorter and longer pulses decreases. If τ_1 increases even more, then the difference changes sign, and a long pulse becomes more effective than a short pulse.

There is therefore a competition between two effects: the stimulated emission, which decreases the signal for short pulse durations, and the reverse photoisomerization, which decreases the signal for long pulses.

The results of the rate equations confirms thus the same trend as the experiment (Figure 4.11), especially the difference between short pulses and long pulses is increased when the number of photons/cm² increases.

For the same pulse duration, a positively chirped pulse induces a smaller difference than a negatively chirped pulse. This is explained by the wavelength shift of the absorption spectrum between rhodopsin and photorhodopsin. This is not observed in the experiment.

Note that the central wavelength for this experiment (535nm) was selected to maximize the absorption of both rhodopsin and photorhodopsin (see Figure 1.16). This seemed the most reasonable choice to exert an effect on the photo-dynamics by single pulse excitation.

However, it would appear that the number of photons/cm² required to produce a significant difference between a short pulse and a long pulse is one to two orders of magnitude higher than the approximate value in Equation 4.3. These figures confirm the results obtained in Figure 4.11 under the following conditions: the real number of photons/cm² is sufficiently high, the reverse quantum yield η_2 is greater than 0.5, and the stimulated emission is no longer possible after $\tau_1 = 4 - 8$ fs.

4.3.4 Results of ab initio simulation

Ab initio simulations were performed by the Laboratory of Computational Chemistry and Biochemistry at Ecole Polytechnique FÃ©dÃ©rale de Lausanne, using the multi-configurational time-dependant Hartree approach. We thus explain here only briefly the Hartree-Fock approximation, extending to the multi-configuration time-dependent Hartree.

The time-dependent Schrödinger equation writes:

$$i\hbar \frac{d}{dt} |\psi(t)\rangle = \hat{H}(t) |\psi(t)\rangle \quad (4.4)$$

and the time-independent Schrödinger equation is:

$$\hat{H} |\psi\rangle = E |\psi\rangle \quad (4.5)$$

By the very essence of the problem we want to solve, i.e. applying an external electromagnetic field, we have to find a way to solve the time-dependent equation. It is a question of solving the Schrödinger equation for a system with several atoms and several electrons. The first approximation is the Born-Oppenheimer approximation. This defines that, since atoms are much heavier than electrons, then the motion of electrons and the motion of atoms can be decoupled. These are motions on different time scales.

Despite this approximation, the motion of the electrons still depends parametrically on the motion of each of the other electrons around it. And it is still not possible to solve analytically the Schrödinger equation for more than a single electron.

We now consider the known wave functions of each electron independently. They satisfy Schrodinger's equation. The Hartree-Fock method⁶⁸ uses an ansatz consisting in the product of the wave functions of each independent electron (the Hartree product) as an approximation of the wave function. By using variational method on the Schrödinger equation (Equation 4.4), it is possible to generate an approximate wavefunction. During the propagation, one could find that solving the Schrodinger equation in this way is equivalent to taking into account, for each electron, only the average Coulomb repulsive force from all the others electrons.

The accuracy of the approach can be increased by taking in account multiple levels of freedom, decreasing at the same time the numerical efficiency. This is the multi-configuration time-dependent Hartree.

For this work, the time dependent Schrödinger equation was solved for the time dependent Hamiltonian including the light matter interaction term in the dipole approximation. The model Hamiltonian includes two electronic states and two vibrational modes within a linear vibronic coupling scheme⁶⁹. The light pulses used in the simulations have been assumed to have a Gaussian envelope with central wavelength of 530 nm and a spectral bandwidth of 100 nm. This is relatively more than the bandwidth used in the experiment, because in the model used for this simulation, the absorption bandwidth of both 11-cis and all-trans ground state are quite narrow. Chirps have been introduced within -1000 to 1000 fs²/rad which effectively provides pulse du-

rations similar to the experiments. The EPFL performed two sets of simulations differing in the amplitudes of the chirped pulses used. The lower amplitude ones have a maximum amplitude of 0.005 au, while the higher ones are three times larger, giving rise to approximately the experimental condition of increasing the energy by one order of magnitude.

The wave packet was positioned in the cis-excited state at the beginning of the dynamics, to amplify the effect of stimulated emission and photo-induced absorption.

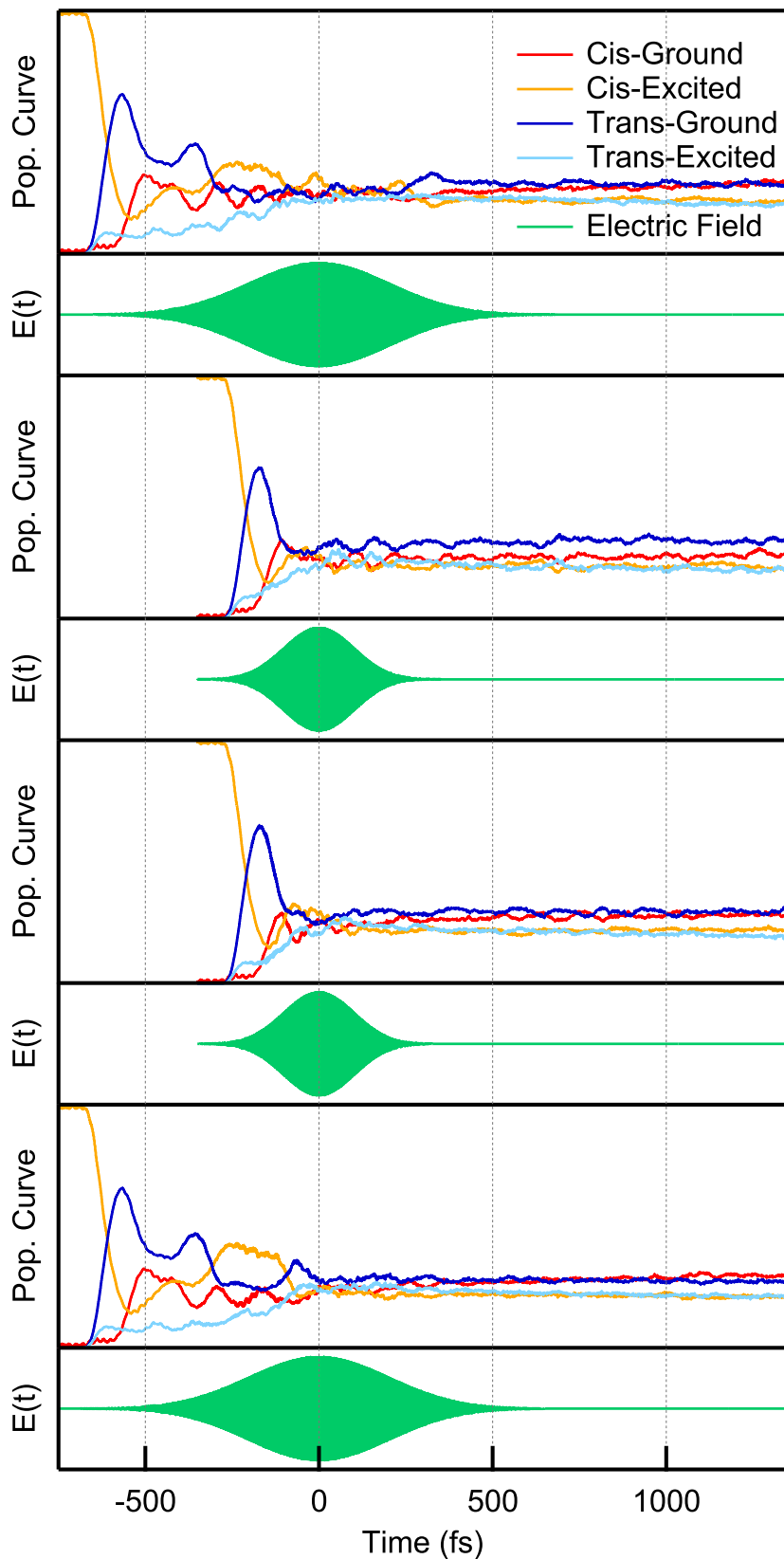


Figure 4.18: Normalized population of the cis-ground, cis-excited, trans-ground and trans-excited state over 4 ps. From top to bottom: linear chirp of -500, -250, 250 and 500 fs²/rad.

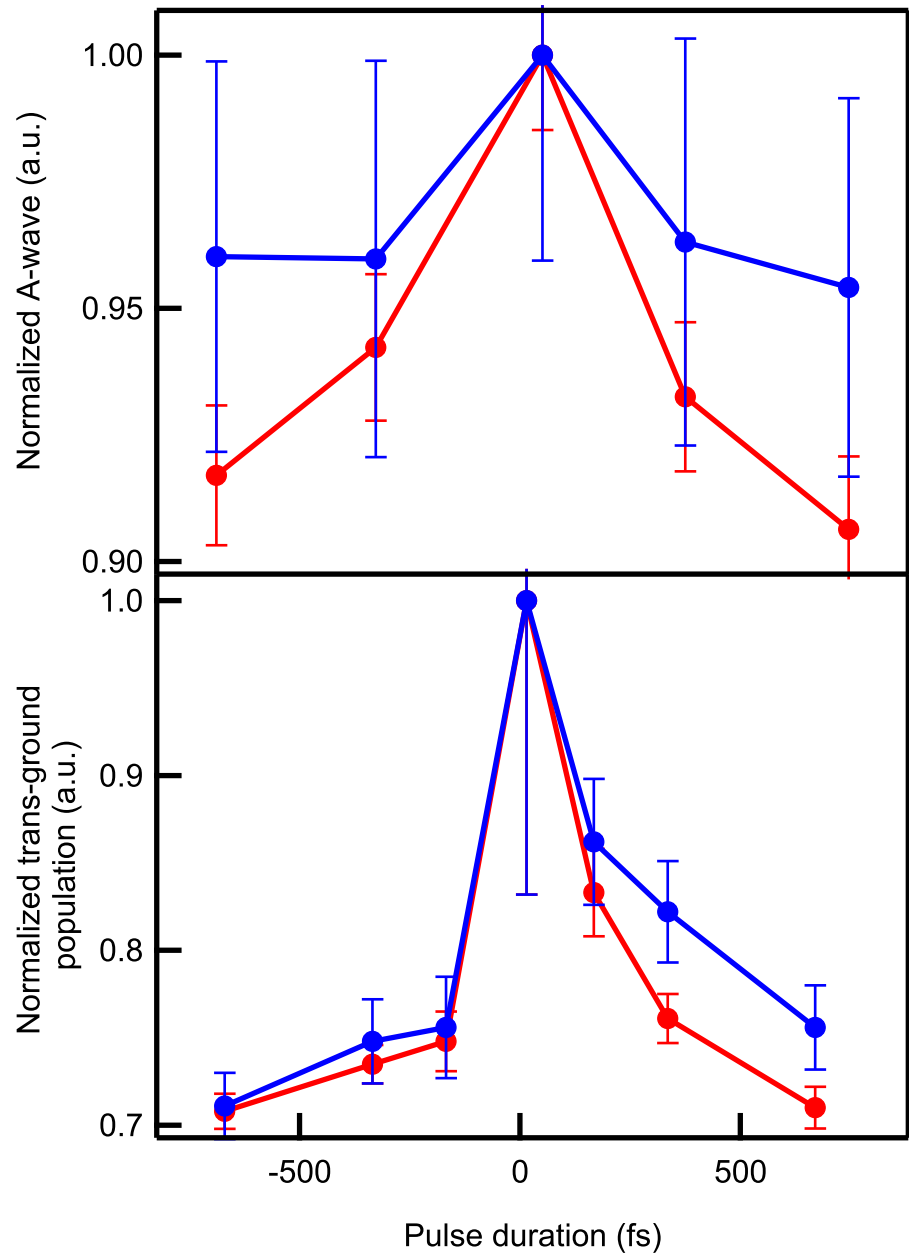


Figure 4.19: Top: Experimental results from Figure 4.11. Bottom: Calculated normalized population of the trans-ground state after 4 ps for different pulse duration and pulse energy (red: 0.015 a.u., blue: 0.005 a.u.). A negative pulse duration actually corresponds to a pulse with a negative chirp. For the simulation, error bars represents the standard error over the last 0.5 ps.

We observe in Figure 4.19 the same trend as in Figure 4.11, that is to say that a long pulse leads to less rhodopsin in the trans-ground state than a short pulse, thus leading to a decrease in the electrical signal from the retina. This difference is explained by the reverse photo-isomerization.

However, the signal difference between the experiment and the simulation is relatively large (8% maximum for the experiment, compared to 30% for the simulation). This is because the simulation initially places all wavepackets in the cis-excited state, rather than in the cis-ground state. All photons are therefore used for stimulated emission and photo-induced absorption, and no longer for absorption from the cis-ground state to the cis-excited state. This approach therefore only shows that the stimulated emission, which should increase the transfer from the cis-excited to the cis-ground while decreasing the pulse duration, is not strong enough compared to the photo-induced absorption and the return to the cis-ground state.

This is therefore not sufficient in itself to prove that the effect observed in Figure 4.11 actually comes from the reverse photo-isomerization.

It is however not possible to put the system in the cis-ground state at the start. The absorption spectrum of the molecule in the calculations is here relatively narrow, centred around 500 nm for the transition from the cis-ground to cis-excited state. Using a positive chirp, the red part (low energy) is therefore completely ineffective.

Finally, as expected, the number of rhodopsins in the trans-ground state is lower for a negatively chirped pulse than for a positively chirped pulse, because of the stimulated emission. This effect is not observed in the experiment, as the signal to noise ratio may be too small to detect it.

4.4 Multi-pulse coherent control of rhodopsin

In this section we will focus on multi-pulse control of the dynamics.

The two approaches are pump-probe experiments, as pioneered by Tannor Kosloff and Rice⁷⁰, with a pump in the visible range and a probe in the near infrared range. We tested two conditions of pulse duration. In the first case, the pulse duration of each pulse is relatively long (50 fs for the two pulses) compared to the time necessary to reach the conical intersection upon visible excitation (80 fs). In the second case, the pulse durations are reduced (pump: 25 fs, probe: 30 fs) with the goal of better discriminating between the stimulated emission from the photo-induced absorption.

4.4.1 ERG power dependence

To set the optimal conditions for the pump-probe experiments, we initially performed a power-dependence of the excitation pulses monitoring their effect on the ERG traces. In particular, we wanted to avoid direct excitation, by the 800 nm pulse, which was meant to interact only after the dynamics was triggered by the 535 nm pulses.

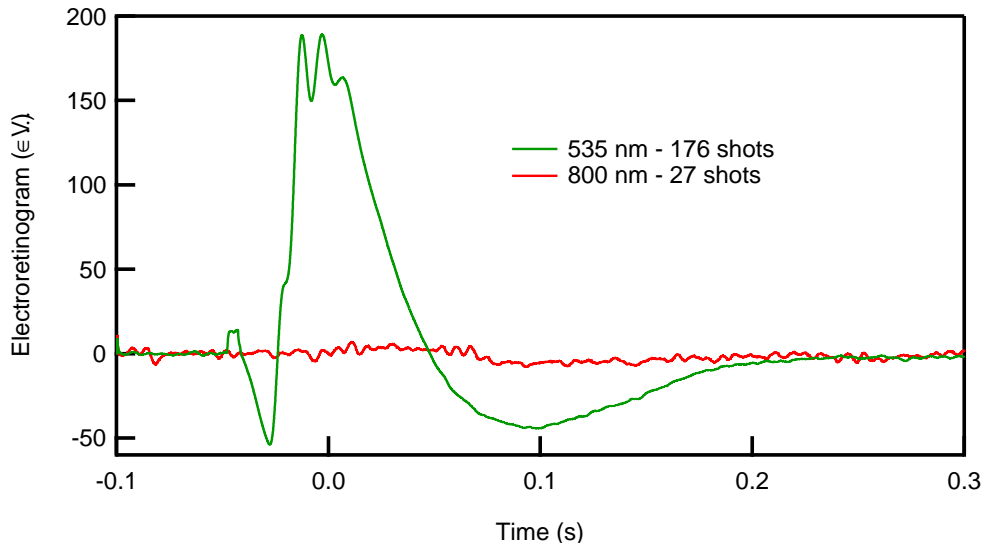


Figure 4.20: Electroretinograms obtained upon 3 nJ excitation at 535 nm (green) and 1 μ J at 800 nm (red). The curves correspond to the average of 176 and 27 ERG traces, obtained at 535 and 800 nm excitation respectively.

The upper limit value of 1 μ J was selected to increase the stimulated emission while preventing direct excitation of the ERG response by 800 nm, which can occur by two photon absorption or by one-photon excitation by the blue tail of the pulse spectrum. As reported in the Figure 4.20, which compares on the same scale the ERG induced by the green pulse at 3 nJ and that of 800 nm at 1 μ J, the 800 nm pulse induces only a weak response visible as a tiny bump between 0 and 0.1 s. This 800 nm-only contribution, for stronger 800 nm excitations, would count as an increase in the visual efficiency in the pump-dump/re-pump trace, decreasing the overall stimulated emission effect. The value of 1 μ J for 800 nm was the best trade-off we found under our experimental conditions between these two opposing effects.

4.4.2 Multi-pulse coherent control using long pulse on rhodopsin

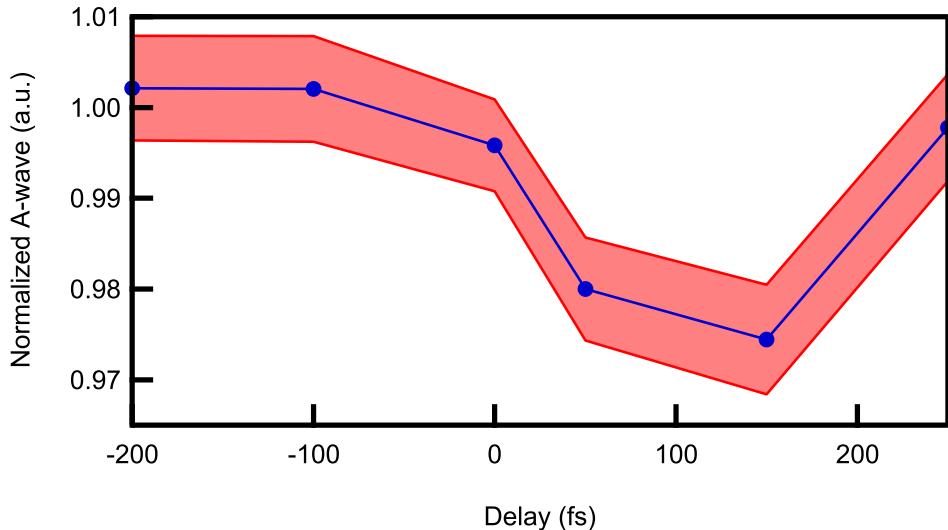


Figure 4.21: Measured normalized A-wave amplitude at different delays.

Positive delays refer to green pulse preceding NIR pulse. The p-value associated with this measurement is 0.04 (one-sided ANOVA). The shaded area represents the standard error of the mean. Data are normalized to a reference taken as the average over the negative pump dump delays (infrared pulse preceding the green pump). Average of 6 data sets conducted on 3 mice

As observed in Figure 4.21, no difference in the ERG signal is observed when the NIR pulse precedes the visible pulse (negative delays), confirming that the 800 nm pulse has no effect on the rhodopsin molecules in their ground state. Conversely, when the 535 nm pulse first generates a vibro-torsional wavepacket in the S1 excited state, the visual response is found to be modulated by the interaction with the NIR probe pulse. More precisely, a first decrease of the A-wave occurs for a delay around 50-100 fs. This decrease is attributed to the dumping of the wavepacket down to the 11-cis-ground state by the 800 nm pulse, before it reaches the conical intersection, which reduces the 11-cis to all-trans photo-isomerization in the retinal moiety. Previous transient absorption measurements on solvated bovine rhodopsin showed that the time required to cross the conical intersection is approximately 80 fs^{5;32}, which is in good agreement with our measurement *in-vivo*. Interestingly, a further decrease occurs at longer time delays, around 150 fs. At the conical

intersection, the wavepacket splits between the different potential surfaces and a fraction of it propagates towards the all-trans ground state. We attribute the decrease around 150 fs to the re-pumping of molecules from the transient all-trans ground state to the all-trans excited state, which leads to reverse isomerization by re-crossing the conical intersection in the opposite direction. After 200 fs delay, the molecule relaxes in the all-trans ground-state, and re-pumping by the 800 nm laser pulses is not possible anymore. Consequently, the retina response efficiency returns to its nominal value.

However, in the Figure 4.21, we cannot distinguish between stimulated emission before and absorption after the conical intersection, as, contrary to the transient absorption experiment from Polli et al.⁵, both effects are associated to the same signs. There are two explanations. The most straightforward one related to the relatively long pulse duration used for this measurement (pump and probe: 50 fs), contrary to the transient absorption's pump and probe (pump: 10 fs, probe: 13 fs). The second one is related to the sign of absorption and stimulated emission in transient absorption. Having a null value at 80 fs does not necessarily mean that none of the processes takes place, but it can also mean that the two contributions compensate for each other.

It is therefore necessary to use shorter pulse durations, to show that the two effects are well separated in time (see subsection 4.4.4).

4.4.3 Results of *ab initio* simulation

In the following, we describe the application of the computational approach detailed in subsection 4.3.4 to the pump-dump/re-pump experiment described in subsection 4.4.2.

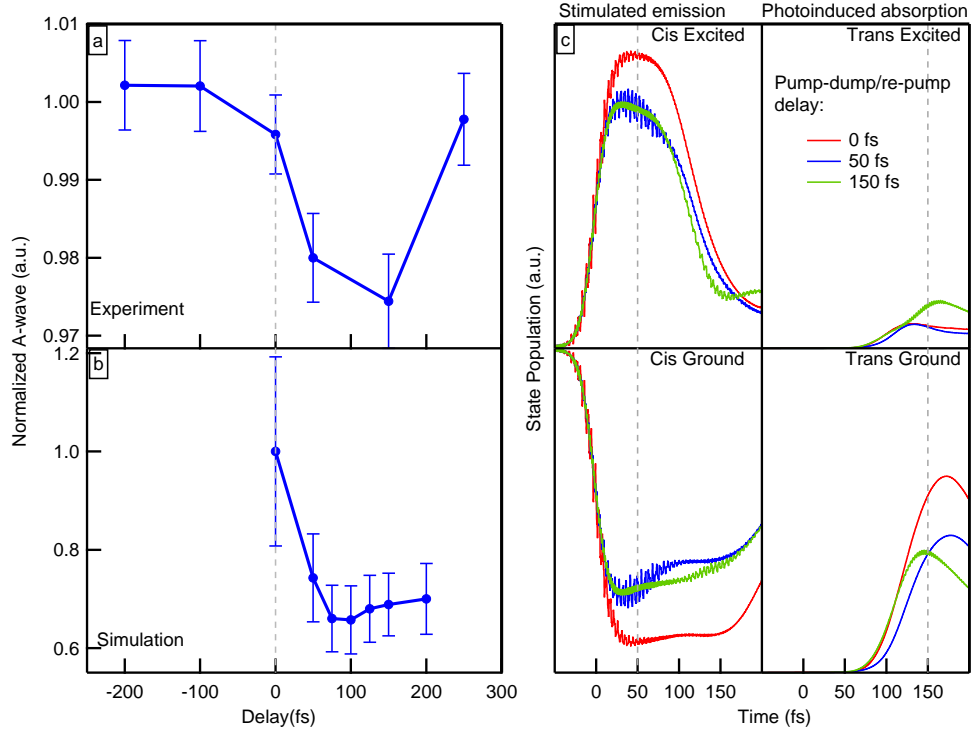


Figure 4.22: *Ab initio* simulation of the pump-dump/re-pump experiment.
 a: Normalized A-wave amplitude measured in the pump-dump/re-pump experiment. - b: Corresponding results obtained by quantum dynamics simulations. The shaded region represents the standard deviation of the mean of the all trans ground population calculated in the time span defined from 0.5 to 4 ps. - c: Transient populations of the rhodopsin states as a function of pump-dump/repump delay.

In our model, the pump is parametrized to have a central wavelength of 500 nm and spectral bandwidth of 10 nm. The dump/re-pump pulse, on the other hand, has a central wavelength of 800 nm with a spectral bandwidth of 20 nm.

Figure 4.22.b depicts the trans-ground state population as a function of pump-dump/re-pump delay normalized to one at zero delay. The trans-ground state population as a function of pump-dump/re-pump delay follows qualitatively the experimental trend shown in Figure 4.22.a with an initial decrease, a minimum around 100 fs and a subsequent increase at longer time delays. The characteristics of the underlying quantum dynamics in these different regimes are illustrated for selected pump-dump/re-pump delays of 0, 50 and 150 fs in Figure 4.22.c. When the dump/re-pump pulse overlaps with

the pump pulse (Figure 4.22.c, red line), the dump/re-pump pulse does not have any significant effect on the overall dynamics since, right after photoexcitation, the wavepacket is still close to the Franck-Condon zone. When the delay between pump and dump/re-pump is 50 fs (Figure 4.22.c, blue line), we observe a dump/re-pump pulse-induced resonant dumping of the wave packet from the cis-excited to the cis-ground state occurring after 40 fs once the dynamics started. As mentioned above, it is well known that the excited wavepacket in rhodopsin takes approximately 80 fs^{5;32} to reach the conical intersection. Therefore, the simulation is consistent with the cis-excited state and the cis-ground state being resonant with an 800 nm photon shortly before the wavepacket crosses the conical intersection thereby lowering the overall trans-ground population. After 100 fs, a significant portion of the wavepacket moves through the conical intersection to the trans-ground state. Shortly after the crossing through the intersection, the wavepacket can resonantly absorb an 800 nm photon to be re-excited to the trans-excited state. This is illustrated by the 150 fs pump-probe delay simulations in Figure 4.22.c, green line.

It should be mentioned that in this model potential, the wavepacket continues to remain highly delocalized. That is why both dumping and re-absorption are observed for time delays beyond 100 fs. The overall trend of the trans-ground population, which correlates with the experimental A-wave amplitudes in the ERG signal, matches qualitatively. However, the regaining of the trans-ground population obtained in the simulations for longer delays is lower compared to the experimental results.

4.4.4 Multi-pulse coherent control using short pulse on rhodopsin

We performed the experiment described in subsection 2.4.2, with a pump centred at 550 nm, 25 fs and a probe centred at 850 nm, 30 fs.

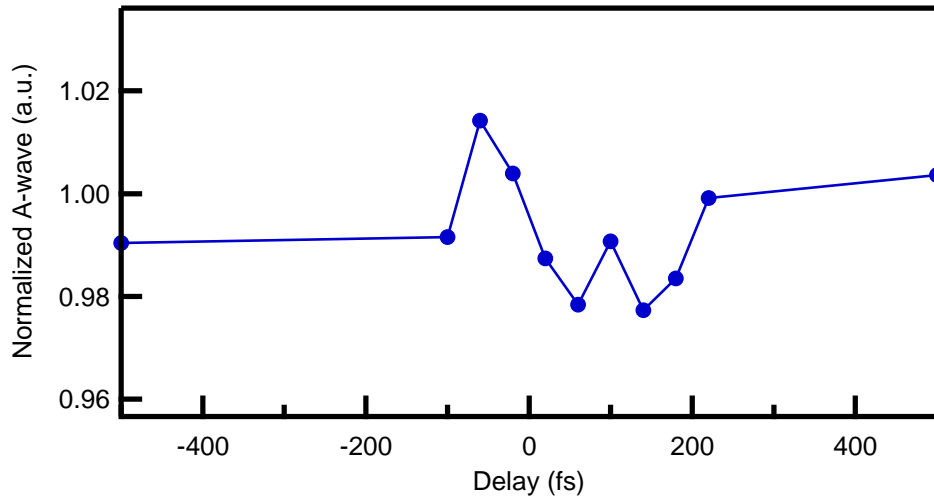


Figure 4.23: Measured normalized A wave amplitude at different delays. Positive delays refer to green pulse preceding NIR pulse. P-value associated with this measurement is 0.03 (one-sided anova). The results shown consist in an average of 5 data sets conducted on 2 mice. Standard error of the mean (not shown) is approximately 0.02 for every delay.

We expect to have, for negative delays, a stable signal, then a decrease around 50 fs, a return to the nominal value around 80 fs, then a decrease around 150 fs to end by a rise to the nominal value for longer periods.

We effectively distinguish two features, corresponding to stimulated emission and photo-induced absorption. However we notice that the signal over noise ratio is poor. This is due to lower number of statistical samples, compared to the experiment performed in the subsection 4.4.2. The stability of the dump/repump pulse is also decreased, as a filament process is involved, to decrease its pulse duration.

Another interesting feature is the increase of signal at -50 fs. This may be due to the coherent artifact, which is often observed in pump probe experiments in which the polarizations are parallel^{71;72}. Indeed, as soon as the beams are superimposed spatially and temporally, it is then difficult to speak of a pump and a probe. The interference created by the superposition of the two beams generates a network of refractive index because of the Kerr effect (Equation 1.15). The pulses (and in particular the 550nm pulse) can be deflected. The number of rhodopsins exposed to the signal is then no longer constant, and the signal increases. This effect would only appear in this experiment because the intensity is higher than previously, due to short pulse duration. This experiment may demonstrate that the stimulated emission and the

photo-induced absorption are well separated in time, but the signal to noise ratio has to be increased to provide stronger evidence.

4.5 Coherent control of medium opsin

4.5.1 Intra-pulse coherent control

We demonstrated the coherent control of rhodopsin in living mice as described in section 4.3. Our results are in agreement with already published experiment in bovine rhodopsin in solution^{32;5}. A biochemical procedure, for extracting cones, similar to what done for rods⁷³, is not available to our best knowledge. Therefore, we used knock-out mice, where the rhodopsin is not expressed in the retina, allowing the control the cones only. We used the same setup as described in section 2.3. The analysis is identical to the one used for the rhodopsin (section 4.3). The main difference comes from the energy, as the cones requires higher energy to exhibit an electroretinogram. The energy used was $1 \mu\text{J}$, at 535 nm, to control the medium green opsin (see Figure 1.11).

Note that the signal is much smaller in cones than in rods, due to their smaller number in the mouse's retina. The A-wave is also noticeably smaller, therefore cannot be used as a good observable. We decided to focus on the B-wave, as it is not saturated in this intensity regime (see Figure 4.1).

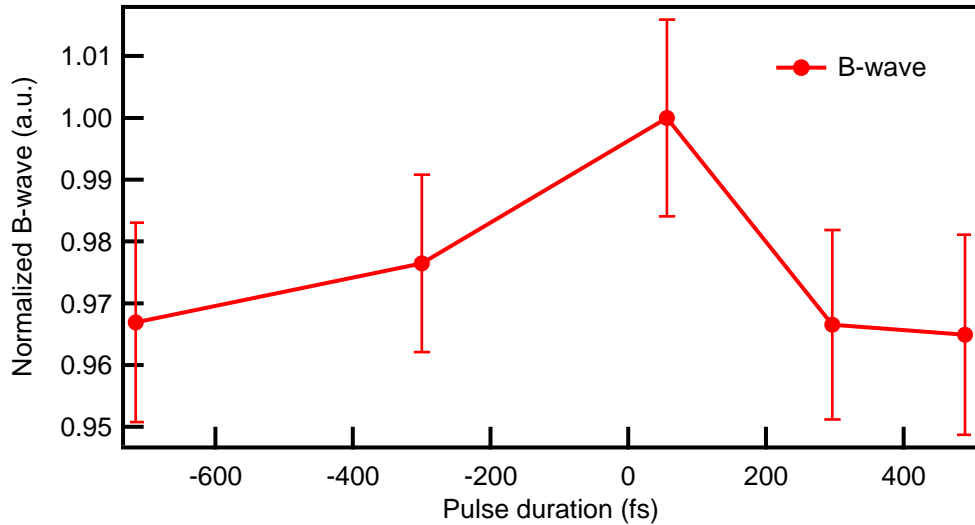


Figure 4.24: Intra-pulse control of the first step of the vision process in rhodopsin knock out mice (3 animals - 1412 ERG traces). Datapoints correspond to normalized B-wave amplitude extracted from the ERG signals obtained from fives values of the pulse chirp (pulse duration respectively: -715, -300, 56, 296, 489 fs).

In Figure 4.24, we observe that, as for the case of rhodopsin, the B-wave amplitude decreases as the pulse duration increases. We do not observe any asymmetry between positive and negative chirps, because the small number of datapoints, which is limited by the experiment duration set by the effect of the anaesthesia on the animal.

Conclusion

The work reported in this thesis manuscript describes a series of optical experiments aiming at the control of the efficiency of the vision process in living animals by manipulation of femtosecond light combined with the detection of low voltage physiological signals. All the experiments take advantage of the measurement of the electroretinogram, a non-invasive way used to monitor the vision process, as described in the section 2.5. I first investigated the vision process upon infrared excitation in *ex-vivo* mice retinas to assess the overall approach and perfect the detection. In a second part, I studied the influence of the spectral phase on the visual perception in living mice. The spectral phase is usually assumed to have no effect on vision, as opposed to the energy or the spectrum of the light. In this work, I also demonstrated that, similarly to molecules in solution, the vision can be coherently controlled using femtosecond pulses.

The first experiment I designed to probe the ultrafast properties of the photo-cycle was a two-photon absorption experiment. Even though the possibility of seeing infrared light has been evoqued since 1976⁷⁴, it was only recently that it was proven to originate from two-photon absorption⁵¹. I characterized the retinal response to 960 nm femtosecond excitation, in *ex-vivo* retinas. The first experiment on living mice was based on scanning a π -step function through the infrared pulse spectrum while measuring the electroretinogram. I demonstrated that the retina's response upon infrared femtosecond pulses is directly dependant of their intensit, even though the energy of each pulses is kept constant.

I successively showed that the retinal response can be controlled using an intra-pulse coherent control based on chirped pulse, and using a two-color pump-dump/re-pump experiment in a living animal.

As detailed in the section 4.3, the spectral phase, and as such, the pulse duration, plays an important role in the ultrafast dynamics at the beginning of the visual process. Indeed, I show that pulses shorter than the isomerization time

scale of rhodopsin generate a greater signal in the electroretinogram, compared to longer pulses. This is due to the interplay of two effects. After the passage through the conical intersection, in its all-trans state, the rhodopsin can absorb a photon, and be switched back to the original *11-cis* conformation. However, this effect is counterbalanced by the stimulated emission which happens at short delay (<80 fs) after the photo-excitation. This effect is more efficient for short pulses, and reduces the number of isomerized rhodopsins, compared to long pulses with the same energy. Therefore, I developed a rate equation model, based on the cross-section and dynamics constants measured.

To further strengthen this interpretation, I designed, as detailed in the section 4.4, a pump-dump (535-800nm) experiment which would tackle this effect, and bring additional evidence. After measuring the retina's response at different pulse delays, I established that the 800 nm pulse reverts the isomerization process of the rhodopsin by two effects. Before the conical intersection, for delay shorter than 80 fs, a Franck-Condon transient window opens, and the dump pulse stimulates the rhodopsin back onto its fundamental state. The second effect is the reverse isomerization upon absorption of the 800 nm pulse after the conical intersection (for delay longer than 80 fs), similar to the process which leads to a decrease in the the vision process observed in the intra-pulse coherent control experiment.

Our interpretation of both intra-pulse and two-color experiment was confirmed by *ab-initio* calculations in collaboration with Prof. U. Roethlisberger's group at Ecole Polytechnique FÃ¢lÃ¢rale de Lausanne.

I also applied the intra-pulse coherent control to the medium opsin, demonstrating that pulse duration also matters in the isomerization of the opsin, used for daylight vision.

In the future, it would be interesting to measure the response of the retina as a function of the pulse duration (as in the intra-pulse experiment) on much longer timescales, up to the millisecond range. Indeed, the decrease we observed here is mainly due to the absorption spectrum of photorhodopsin, partially overlaying in some part the absorption spectrum of rhodopsin. Afterwards, the photorhodopsin relaxes into bathorhodopsin until the Metarhodopsin II, allowing the visual process. As it relaxes, the absorption spectrum changes, most likely reducing the effect.

On the other hand, the dynamics of the cones as not been measured yet. I provided some insight regarding their response, using the intra-pulse coherent control, but a *ad hoc* pump-dump/re-pump experiment would provide a more complete understanding.

Finally, in the intra-pulse coherent control experiment, I observed that it

was only possible to reduce the retinal signal. However, I only tried the pulses whose temporal form was predefined (linear chirp). Using a genetic algorithm, and relying onto the *ex-vivo* system, allowing more stable and longer acquisitions, it is certainly possible to investigate pulses temporal shape which could improve vision⁷⁵.

Appendix

Optical Parametric Amplification

The optical parametric amplification is a $\chi^{(2)}$ process in which an input pulse energy is amplified. A high energy pump (with frequency ω_p) amplifies a low energy signal beam (with frequency ω_s). To fulfil the energy conservation (Equation 4.6) , an idler beam is generated in the process (with frequency ω_i).

$$\omega_p = \omega_s + \omega_i \quad (4.6)$$

In this section, we derive some fundamental properties of the optical parametric amplification, such as the exponential amplification of the input signal and phase matching.

We start with the Maxwell's law:

$$\nabla \cdot \vec{\mathbf{D}} = \rho \quad (4.7)$$

$$\nabla \cdot \vec{\mathbf{B}} = 0 \quad (4.8)$$

$$\nabla \times \vec{\mathbf{E}} = -\frac{\partial \vec{\mathbf{B}}}{\partial t} \quad (4.9)$$

$$\nabla \times \vec{\mathbf{H}} = \frac{\partial \vec{\mathbf{D}}}{\partial t} + \vec{\mathbf{J}} \quad (4.10)$$

With

- $\vec{\mathbf{E}}$ the electric field.
- $\vec{\mathbf{D}}$ the displacement vector, defined as $\vec{\mathbf{D}} = \epsilon_0 \vec{\mathbf{E}} + \vec{\mathbf{P}}$.
- $\vec{\mathbf{B}}$ the magnetic field.
- $\vec{\mathbf{H}}$ the magnetic field strength, defined as $\vec{\mathbf{B}} = \mu_0 \vec{\mathbf{H}}$.
- $\vec{\mathbf{P}}$ the polarization of the medium.

We set the conditions such as there is no free charges and no free currents. Therefore, $\rho = 0$ and $\vec{\mathbf{J}} = 0$.

We first derive the wave equation. The first step is to calculate the curl of the curl of the electric field, by using the Equation 4.9.

$$\nabla \times (\nabla \times \vec{\mathbf{E}}) = -\frac{\partial(\nabla \times \vec{\mathbf{B}})}{\partial t} \quad (4.11)$$

We now use the Equation 4.10.

$$\nabla \times (\nabla \times \vec{\mathbf{E}}) = -\mu_0 \frac{\partial^2 \vec{\mathbf{D}}}{\partial t^2} \quad (4.12)$$

We can also use the vectorial identity:

$$\nabla \times (\nabla \times \vec{\mathbf{E}}) = \nabla(\nabla \cdot \vec{\mathbf{E}}) - \nabla^2 \vec{\mathbf{E}} \quad (4.13)$$

As there is no free charge, we also have $\nabla \cdot \vec{\mathbf{D}} = \nabla \cdot \vec{\mathbf{E}} = 0$, and we can equalize the Equation 4.12 and Equation 4.13, to obtain the following equation:

$$\nabla^2 \vec{\mathbf{E}} = \mu_0 \frac{\partial^2 \vec{\mathbf{D}}}{\partial t^2} \quad (4.14)$$

By replacing the displacement vector by its definition, the equation becomes:

$$\nabla^2 \vec{\mathbf{E}} - \epsilon_0 \mu_0 \frac{\partial^2 \vec{\mathbf{E}}}{\partial t^2} = \mu_0 \frac{\partial^2 \vec{\mathbf{P}}}{\partial t^2} \quad (4.15)$$

As the speed of light in vacuum is defined as $c = \frac{1}{\sqrt{\epsilon_0 \mu_0}}$, the wave Equation 4.15 becomes:

$$\nabla^2 \vec{\mathbf{E}} - \frac{1}{c^2} \frac{\partial^2 \vec{\mathbf{E}}}{\partial t^2} = \frac{1}{\epsilon_0 c^2} \frac{\partial^2 \vec{\mathbf{P}}}{\partial t^2} \quad (4.16)$$

As we are interested in non-linear processes, we introduce here the non-linear polarization part: $\vec{\mathbf{P}} = \vec{\mathbf{P}}_1 + \vec{\mathbf{P}}_{NL}$, where $\vec{\mathbf{P}}_1$ is the linear part of the polarization and $\vec{\mathbf{P}}_{NL}$ the non-linear one. This is now introduced into the Equation 4.16:

$$\nabla^2 \vec{\mathbf{E}} - \frac{1}{c^2} \frac{\partial^2 \vec{\mathbf{E}}}{\partial t^2} = \frac{1}{\epsilon_0 c^2} \frac{\partial^2 \vec{\mathbf{P}}_1}{\partial t^2} + \frac{1}{\epsilon_0 c^2} \frac{\partial^2 \vec{\mathbf{P}}_{NL}}{\partial t^2} \quad (4.17)$$

The linear part of the polarization $\vec{\mathbf{P}}_1$ can be rewritten as $\vec{\mathbf{P}}_1 = \epsilon_0 \chi \vec{\mathbf{E}}$, with χ the electric susceptibility of the material. Therefore, the Equation 4.17 can be reduced as:

$$\nabla^2 \vec{\mathbf{E}} - \frac{(1 + \chi)}{c^2} \frac{\partial^2 \vec{\mathbf{E}}}{\partial t^2} = \frac{1}{\epsilon_0 c^2} \frac{\partial^2 \vec{\mathbf{P}}_{\text{NL}}}{\partial t^2} \quad (4.18)$$

The factor $(1 + \chi)$ can be rewritten as ϵ_r , the relative permittivity:

$$\nabla^2 \vec{\mathbf{E}} - \frac{\epsilon_r}{c^2} \frac{\partial^2 \vec{\mathbf{E}}}{\partial t^2} = \frac{1}{\epsilon_0 c^2} \frac{\partial^2 \vec{\mathbf{P}}_{\text{NL}}}{\partial t^2} \quad (4.19)$$

In the same way the polarization $\vec{\mathbf{P}}_1$ is proportional to $\vec{\mathbf{E}}$, we can write $\vec{\mathbf{P}}_{\text{NL}} = \epsilon_0 \chi^{(2)} \vec{\mathbf{E}}^2$, where $\chi^{(2)}$ is the second order electric susceptibility. The final wave equation in media, taking in account the non-linear polarization becomes:

$$\nabla^2 \vec{\mathbf{E}} - \frac{\epsilon_r}{c^2} \frac{\partial^2 \vec{\mathbf{E}}}{\partial t^2} = \frac{\chi^{(2)}}{c^2} \frac{\partial^2 \vec{\mathbf{E}}^2}{\partial t^2} \quad (4.20)$$

As we are interested in the propagation of three waves into the z direction (the pump, the signal and the idler), the electric field is:

$$\vec{\mathbf{E}} = \frac{1}{2} (A_p e^{i(\omega_p t - k_p z)} + A_s e^{i(\omega_s t - k_s z)} + A_i e^{i(\omega_i t - k_i z)}) + c.c \quad (4.21)$$

$$\begin{aligned} 4\vec{\mathbf{E}}^2 = & A_p^2 e^{i(2\omega_p t - 2k_p z)} + A_s^2 e^{i(2\omega_s t - 2k_s z)} + A_i^2 e^{i(2\omega_i t - 2k_i z)} + \\ & 2A_p A_s e^{i((\omega_p + \omega_s)t - (k_p + k_s)z)} + 2A_p A_i e^{i((\omega_p + \omega_i)t - (k_p + k_i)z)} + 2A_s A_i e^{i((\omega_s + \omega_i)t - (k_s + k_i)z)} + \\ & 2A_p A_s^* e^{i((\omega_p - \omega_s)t - (k_p - k_s)z)} + 2A_p A_i^* e^{i((\omega_p - \omega_i)t - (k_p - k_i)z)} + 2A_s A_i^* e^{i((\omega_s - \omega_i)t - (k_s - k_i)z)} + \\ & |A_p|^2 + |A_s|^2 + |A_i|^2 + c.c. \end{aligned} \quad (4.22)$$

This term induces all the second order non-linear effects. Indeed, the first line corresponds to second harmonic generation (SHG), the second line to sum frequency generation (SFG) and the third line to DFG (difference frequency generation). However, they cannot all happen at the same time, as the phase matching condition (see Equation 4.30) cannot be matched for all of them in non-linear crystal. We will now concentrate on the term that generates the three frequencies we are interested in the optical parametric amplification, which satisfy the Equation 4.6. Therefore:

$$\begin{aligned}
\vec{\mathbf{E}}^2 = & \frac{1}{2} A_s A_i e^{i(\omega_p t - (k_s + k_i)z)} + \\
& \frac{1}{2} A_p A_s^* e^{i(\omega_i t - (k_p - k_s)z)} + \\
& \frac{1}{2} A_p A_i^* e^{i(\omega_s t - (k_p - k_i)z)} + c.c.
\end{aligned} \tag{4.23}$$

We start by calculating the different parts of the wave Equation 4.20. We will only concentrate on the direction of propagation z, therefore $\nabla^2 \vec{\mathbf{E}}$ becomes $\frac{\partial^2 \vec{\mathbf{E}}}{\partial z^2}$.

$$\begin{aligned}
\frac{\partial^2 \vec{\mathbf{E}}^2}{\partial t^2} = & -\frac{1}{2} A_s A_i \omega_p^2 e^{i(\omega_p t - (k_s + k_i)z)} + \\
& -\frac{1}{2} A_p A_s^* \omega_i^2 e^{i(\omega_i t - (k_p - k_s)z)} + \\
& -\frac{1}{2} A_p A_i^* \omega_s^2 e^{i(\omega_s t - (k_p - k_i)z)} + c.c.
\end{aligned} \tag{4.24}$$

$$\begin{aligned}
\frac{\partial^2 \vec{\mathbf{E}}}{\partial z^2} = & -ik_p \frac{\partial A_p}{\partial z} e^{i(\omega_p t - k_p z)} - \frac{1}{2} A_p k_p^2 e^{i(\omega_p t - k_p z)} + \frac{1}{2} \frac{\partial^2 A_p}{\partial z^2} e^{i(\omega_p t - k_p z)} + \\
& -ik_s \frac{\partial A_s}{\partial z} e^{i(\omega_s t - k_s z)} - \frac{1}{2} A_s k_s^2 e^{i(\omega_s t - k_s z)} + \frac{1}{2} \frac{\partial^2 A_s}{\partial z^2} e^{i(\omega_s t - k_s z)} + \\
& -ik_s \frac{\partial A_i}{\partial z} e^{i(\omega_i t - k_i z)} - \frac{1}{2} A_i k_i^2 e^{i(\omega_i t - k_i z)} + \frac{1}{2} \frac{\partial^2 A_i}{\partial z^2} e^{i(\omega_i t - k_i z)} + c.c
\end{aligned} \tag{4.25}$$

$$\begin{aligned}
\frac{\partial^2 \vec{\mathbf{E}}}{\partial t^2} = & -\frac{1}{2} A_p \omega_p^2 e^{i(\omega_p t - k_p z)} + \\
& -\frac{1}{2} A_s \omega_s^2 e^{i(\omega_s t - k_s z)} + \\
& -\frac{1}{2} A_i \omega_i^2 e^{i(\omega_i t - k_i z)} + c.c
\end{aligned} \tag{4.26}$$

We replace the Equation 4.24, Equation 4.25 and Equation 4.26 in the Equation 4.20. As the equation needs to be fulfilled at any time, we can split it into three equations, where the term $e^{i\omega_n t}$ is factorized.

$$\begin{aligned}
\frac{1}{2}e^{i(\omega_p t - k_p z)} \left(-2ik_p \frac{\partial A_p}{\partial z} - A_p k_p^2 + \frac{\partial^2 A_p}{\partial^2 z} + \frac{\epsilon_r}{c^2} A_p \omega_p^2 \right) &= -\frac{\chi^{(2)}}{2c^2} A_s A_i \omega_p^2 e^{i(\omega_p t - (k_s + k_i)z)} \\
\frac{1}{2}e^{i(\omega_s t - k_s z)} \left(-2ik_s \frac{\partial A_s}{\partial z} - A_s k_s^2 + \frac{\partial^2 A_s}{\partial^2 z} + \frac{\epsilon_r}{c^2} A_s \omega_s^2 \right) &= -\frac{\chi^{(2)}}{2c^2} A_p A_i^* \omega_s^2 e^{i(\omega_s t - (k_p - k_i)z)} \\
\frac{1}{2}e^{i(\omega_i t - k_i z)} \left(-2ik_s \frac{\partial A_i}{\partial z} - A_i k_i^2 + \frac{\partial^2 A_i}{\partial^2 z} + \frac{\epsilon_r}{c^2} A_i \omega_i^2 \right) &= -\frac{\chi^{(2)}}{2c^2} A_p A_s^* \omega_i^2 e^{i(\omega_i t - (k_p - k_s)z)}
\end{aligned} \tag{4.27}$$

We drop here the complex conjugate, as they are no longer useful for the resolution of the wave equation.

These equations can be simplified. Indeed, $k_p^2 = \frac{n^2 \omega^2}{c^2} = \frac{\epsilon_r \omega^2}{c^2}$ with $n = \sqrt{\epsilon_r}$ the refractive index. Therefore, the second and fourth terms of left side of each equations are cancelled. By passing the exponential from the left side to the right side we obtain:

$$\begin{aligned}
-2ik_p \frac{\partial A_p}{\partial z} + \frac{\partial^2 A_p}{\partial^2 z} &= -\frac{\chi^{(2)}}{c^2} A_s A_i \omega_p^2 e^{i(k_p - k_s - k_i)z} \\
-2ik_s \frac{\partial A_s}{\partial z} + \frac{\partial^2 A_s}{\partial^2 z} &= -\frac{\chi^{(2)}}{c^2} A_p A_i^* \omega_s^2 e^{i(k_s - k_p + k_i)z} \\
-2ik_s \frac{\partial A_i}{\partial z} + \frac{\partial^2 A_i}{\partial^2 z} &= -\frac{\chi^{(2)}}{c^2} A_p A_s^* \omega_i^2 e^{i(k_i - k_p + k_s)z}
\end{aligned} \tag{4.28}$$

To get rid of the second term of the left side, we invoke the slowly varying envelope approximation. It states that if the envelope of a wave varies slowly compared to the optical cycle time, then

$$\left| \frac{\partial^2 A}{\partial z^2} \right| \ll 2k \left| \frac{\partial A}{\partial z} \right| \tag{4.29}$$

Therefore, the equation is simplified as follow:

$$\begin{aligned}
\frac{\partial A_p}{\partial z} &= -\frac{i\chi^{(2)}\omega_p^2}{2c^2 k_p} A_s A_i e^{i(k_p - k_s - k_i)z} \\
\frac{\partial A_s}{\partial z} &= -\frac{i\chi^{(2)}\omega_s^2}{2c^2 k_s} A_p A_i^* e^{i(k_s - k_p + k_i)z} \\
\frac{\partial A_i}{\partial z} &= -\frac{i\chi^{(2)}\omega_i^2}{2c^2 k_i} A_p A_s^* e^{i(k_i - k_p + k_s)z}
\end{aligned} \tag{4.30}$$

From the Equation 4.30 it is clear that the amplification of the signal is dependant of the phase matching. By misplacing the crystal, SFG with

the signal and idler could occur (first equation), increasing the amplitude of the electric field's pump. The second and the first equation have the same phase matching, and therefore an amplification of the signal results in the amplification of the idler, as energy conservation requires.

We now solve the Equation 4.30 for optical parametric amplification, i.e. the case where the energy of the pump is transferred in the idler and the signal. Let's consider that the energy of the pump pulse is high compared to the energy of the signal. Therefore $\frac{\partial A_p}{\partial z} = 0$. We also define $\Delta k = k_s - k_p + k_i$. To resolve the system, we derive the second equation from the Equation 4.30.

$$\frac{\partial^2 A_s}{\partial z^2} = - \frac{i\chi^{(2)}\omega_s^2}{2c^2k_s} \frac{\partial}{\partial z} (A_p A_i^* e^{i\Delta kz}) \quad (4.31)$$

$$\frac{\partial^2 A_s}{\partial z^2} = - \frac{i\chi^{(2)}\omega_s^2}{2c^2k_s} \left(\frac{\partial A_p}{\partial z} A_i^* e^{i\Delta kz} + A_p \frac{\partial A_i^* e^{i\Delta kz}}{\partial z} \right) \quad (4.32)$$

$$\frac{\partial^2 A_s}{\partial z^2} = - \frac{i\chi^{(2)}\omega_s^2}{2c^2k_s} \left(A_p \frac{\partial A_i^*}{\partial z} e^{i\Delta kz} + i\Delta k A_p A_i^* e^{i\Delta kz} \right) \quad (4.33)$$

Where we cancelled the derivative of A_p in the Equation 4.32.

We now include the complex conjugate of the third equation of the Equation 4.30:

$$\frac{\partial^2 A_s}{\partial z^2} = - \frac{i\chi^{(2)}\omega_s^2}{2c^2k_s} \left(A_p \frac{i\chi^{(2)}\omega_i^2}{2c^2k_i} A_p^* A_s e^{-i\Delta kz} e^{i\Delta kz} + i\Delta k A_p A_i^* e^{i\Delta kz} \right) \quad (4.34)$$

We simplify:

$$\frac{\partial^2 A_s}{\partial z^2} = \frac{\chi^{(2)}\omega_s^2}{2c^2k_s} \left(|A_p|^2 \frac{\chi^{(2)}\omega_i^2}{2c^2k_i} A_s + \Delta k A_p A_i^* e^{i\Delta kz} \right) \quad (4.35)$$

We replace A_i^* in the second equation of the Equation 4.30 to obtain:

$$\frac{\partial^2 A_s}{\partial z^2} = \frac{\chi^{(2)}\omega_s^2\omega_i^2}{4c^4k_s k_i} |A_p|^2 A_s - i\Delta k \frac{\partial A_s}{\partial z} \quad (4.36)$$

This is the final differential equation for the optical parametric amplification.

We are going to solve the optical parametric amplification for the special case $\Delta k = 0$.

The general solution of this equation is in the form:

$$A_s(z) = A \cosh(\alpha z) + B \sinh(\beta z) \quad (4.37)$$

The parameters α and β can be found by inserting this solution in the Equation 4.36:

$$A\alpha^2 \cosh(\alpha z) + B\beta^2 \sinh(\beta z) = \frac{\chi^{(2)} \omega_s^2 \omega_i^2}{4c^4 k_s k_i} |A_p|^2 (A \cosh(\alpha z) + B \sinh(\beta z)) \quad (4.38)$$

To satisfy this equation for every position, we must have:

$$\beta^2 = \alpha^2 = \frac{\chi^{(2)} \omega_s^2 \omega_i^2}{4c^4 k_s k_i} |A_p|^2 \quad (4.39)$$

To find the constants A and B, we need to consider the boundary conditions and Equation 4.30. We also will consider the general solution for A_i :

$$A_i(z) = C \cosh(\delta z) + D \sinh(\gamma z) \quad (4.40)$$

At the beginning of optical parametric amplification, there is an input beam that is amplified, and no idler beam. The idler is generated by the process. Therefore:

$$\begin{aligned} A_s(0) &= \text{arbitrary} \\ A_i(0) &= 0 \end{aligned} \quad (4.41)$$

Therefore, it implies that $C = 0$, and $A = A_s(0)$. We replace these equations in the Equation 4.30, where we define $g^2 = \alpha^2$:

$$\begin{aligned} A_s(0)g \sinh(gz) + Bg \cosh(gz) &= -\frac{i\chi^{(2)} \omega_s^2}{4c^2 k_s} A_p D^* \sinh(\gamma z) \\ D\gamma \cosh(\gamma z) &= -\frac{i\chi^{(2)} \omega_i^2}{4c^2 k_i} A_p (A_s(0)^* \cosh(gz) + B^* \sinh(gz)) \end{aligned} \quad (4.42)$$

To satisfy both these equations, it is clear that $B = 0$ and $\gamma = g$. Therefore:

$$\begin{aligned} A_s(0)g &= -\frac{i\chi^{(2)}\omega_s^2}{4c^2k_s}A_pD^* \\ Dg &= -\frac{i\chi^{(2)}\omega_i^2}{4c^2k_i}A_pA_s(0)^* \end{aligned} \quad (4.43)$$

By replacing Equation 4.39 into the second equation, we obtain the solution for D:

$$D\frac{\chi^{(2)}\omega_s\omega_i}{2c^2\sqrt{k_sk_i}}|A_p| = -\frac{i\chi^{(2)}\omega_i^2}{4c^2k_i}A_pA_s^*(0) \quad (4.44)$$

By taking in account that $k_s = \frac{n_s\omega_s}{c}$ and $k_i = \frac{n_i\omega_i}{c}$, we obtain:

$$D = -2iA_s^*(0)\left(\frac{\omega_i n_s}{\omega_s n_i}\right)^{\frac{1}{2}}\frac{A_p}{|A_p|} \quad (4.45)$$

Therefore, the final amplitude for the signal and idler electric field in an optical parametric amplification process are:

$$\begin{aligned} A_s(z) &= A_s(0)\cosh(gz) \\ A_i(z) &= -2iA_s^*(0)\left(\frac{\omega_i n_s}{\omega_s n_i}\right)^{\frac{1}{2}}\frac{A_p}{|A_p|}\sinh(gz) \end{aligned} \quad (4.46)$$

And the electric field of each beam is now:

$$\begin{aligned} E_s(z, t) &= \frac{1}{2}A_s(0)\cosh(gz)e^{i(\omega_s t - k_s z)} + c.c \\ E_i(z, t) &= -iA_s^*(0)\left(\frac{\omega_i n_s}{\omega_s n_i}\right)^{\frac{1}{2}}\frac{A_p}{|A_p|}\sinh(gz)e^{i(\omega_i t - k_i z)} + c.c \end{aligned} \quad (4.47)$$

With $g = \frac{\chi^{(2)}\omega_s\omega_i}{2c^2\sqrt{k_sk_i}}|A_p| = \frac{\chi^{(2)}}{2c}\left(\frac{\omega_s\omega_i}{n_s n_i}\right)^{\frac{1}{2}}|A_p|$.

For a sufficiently long propagation length, $\cosh(gz) = \sinh(gz) = e^{gz}$, and there is an exponential amplification of the signal and the idler. Intuitively, there is an exponential growth because when w_i is amplified, it is also amplifying w_s , which amplifies w_i etc...

We also notice that the phase of the input signal beam is conserved.

Bibliography

- [1] Gérard Simon. On the theory of visual perception of kepler and descartes: reflections on the role of mechanism in the birth of modern science. *Vistas in Astronomy*, 18:825–832, 1975.
- [2] A Einstein. Kinetic equilibrium of absorption and emission of blackbody radiation by an atom. *Phys. Z.*, 18:121, 1917.
- [3] P Maine, D Strickland, P Bado, M Pessot, and G Mourou. Generation of ultrahigh peak power pulses by chirped pulse amplification. *IEEE Journal of Quantum electronics*, 24(2):398–403, 1988.
- [4] R. Schoenlein, L. Peteanu, R. Mathies, and C. Shank. The first step in vision: Femtosecond isomerization of rhodopsin. *Science*, 254(5030):412–415, October 1991.
- [5] Dario Polli, Piero Altoè, Oliver Weingart, Katelyn M. Spillane, Christian Manzoni, Daniele Brida, Gaia Tomasello, Giorgio Orlandi, Philipp Kukura, Richard A. Mathies, Marco Garavelli, and Giulio Cerullo. Conical intersection dynamics of the primary photoisomerization event in vision. *Nature*, 467(7314):440–443, September 2010.
- [6] A. C. Florean, D. Cardoza, J. L. White, J. K. Lanyi, R. J. Sension, and P. H. Bucksbaum. Control of retinal isomerization in bacteriorhodopsin in the high-intensity regime. *Proceedings of the National Academy of Sciences*, 106(27):10896–10900, July 2009.
- [7] Kush Paul, Parijat Sengupta, Eugene D. Ark, Haohua Tu, Youbo Zhao, and Stephen A. Boppart. Coherent control of an opsin in living brain tissue. *Nature Physics*, 13(11):1111–1116, November 2017.
- [8] Georg Nagel, Tanjef Szellas, Wolfram Huhn, Suneel Kateriya, Nona Adeishvili, Peter Berthold, Doris Ollig, Peter Hegemann, and Ernst Bamberg. Channelrhodopsin-2, a directly light-gated cation-selective

- membrane channel. *Proceedings of the National Academy of Sciences*, 100(24):13940–13945, 2003.
- [9] Andrew M Weiner. Ultrafast optical pulse shaping: A tutorial review. *Optics Communications*, 284(15):3669–3692, 2011.
 - [10] Stefan Weber, Luigi Bonacina, Wilfried Noell, Denis Kiselev, Jérôme Extermann, Fabio Jutzi, Sébastien Lani, Ondrej Nenadl, Jean-Pierre Wolf, and Nico F. de Rooij. Design, simulation, fabrication, packaging, and characterization of a MEMS-based mirror array for femtosecond pulse-shaping in phase and amplitude. *Review of Scientific Instruments*, 82(7):075106, 2011.
 - [11] S. Afonina, Ondrej Nenadl, Ariana Rondi, Luigi Bonacina, Jérôme Extermann, Denis Kiselev, Igor Dolamic, T. Burgi, and Jean-Pierre Wolf. Discriminability of tryptophan containing dipeptides using quantum control. *Applied Physics. B, Lasers and Optics*, 111(4):541, 2013.
 - [12] Antoine Monmayrant, Sébastien Weber, and Béatrice Chatel. A newcomer’s guide to ultrashort pulse shaping and characterization. *Journal of Physics B: Atomic, Molecular and Optical Physics*, 43(10):103001, May 2010.
 - [13] Rick Trebino. *Frequency-Resolved Optical Gating: The Measurement of Ultrashort Laser Pulses*. Springer Science & Business Media, December 2012.
 - [14] Rick Trebino. Measuring Ultrashort Laser Pulses II: FROG.
 - [15] Jérôme Kasparian and Jean-Pierre Wolf. Physics and applications of atmospheric nonlinear optics and filamentation. *Optics Express*, 16(1):466–493, January 2008.
 - [16] Sergey Mitryukovskiy. *Coherent secondary radiation from femtosecond laser filaments*. Thesis, 2014.
 - [17] Bruno E. Schmidt, Waldemar Unrau, Aldo Mirabal, Shaohui Li, Marcel Krenz, Ludger Wöste, and Torsten Siebert. Poor man’s source for sub 7 fs: A simple route to ultrashort laser pulses and their full characterization. *Optics Express*, 16(23):18910, November 2008.
 - [18] Michael Mauser. Experiencing Light’s Properties Within Your Own Eye. *The Physics Teacher*, 49:19, January 2011.

- [19] Russell N. Van Gelder and Kuldeep Kaur. Vision Science: Can Rhodopsin Cure Blindness? *Current Biology*, 25(16):R713–R715, August 2015.
- [20] Dale Purves, editor. *Neuroscience*. Sinauer Associates, Publishers, Sunderland, Mass, 3rd ed edition, 2004.
- [21] Dale Purves, George J. Augustine, David Fitzpatrick, Lawrence C. Katz, Anthony-Samuel LaMantia, James O. McNamara, and S. Mark Williams. Anatomical Distribution of Rods and Cones. *Neuroscience*. 2nd edition, 2001.
- [22] Yingbin Fu and King-Wai Yau. Phototransduction in mouse rods and cones. *Pflugers Archiv : European journal of physiology*, 454(5):805–819, August 2007.
- [23] Inessa Bekerman, Paul Gottlieb, and Michael Vaiman. Variations in Eyeball Diameters of the Healthy Adults. *Journal of ophthalmology*, 2014:503645, November 2014.
- [24] Jessica Skeie, Stephen Tsang, and Vinit Mahajan. Evisceration of Mouse Vitreous and Retina for Proteomic Analyses. *Journal of visualized experiments : JoVE*, 50, April 2011.
- [25] Andrew D. Huberman and Christopher M. Niell. What can mice tell us about how vision works? *Trends in Neurosciences*, 34(9):464–473, September 2011.
- [26] Daisuke Kojima, Suguru Mori, Masaki Torii, Akimori Wada, Rika Morishita, and Yoshitaka Fukada. Uv-sensitive photoreceptor protein opn5 in humans and mice. *PLoS one*, 6:e26388, 2011.
- [27] Vladimir J. Kefalov. Rod and Cone Visual Pigments and Phototransduction through Pharmacological, Genetic, and Physiological Approaches. *Journal of Biological Chemistry*, 287(3):1635–1641, January 2012.
- [28] Markus Meister and Marc Tessier-Lavigne. Low-Level Visual Processing: The Retina. In *Principles of Neural Science*. McGraw-Hill Companies, fifth edition, 2013.
- [29] C. Schnedermann, X. Yang, M. Liebel, K. M. Spillane, J. Lugtenburg, I. Fernández, A. Valentini, I. Schapiro, M. Olivucci, P. Kukura, and R. A. Mathies. Evidence for a vibrational phase-dependent isotope effect on the photochemistry of vision. *Nature Chemistry*, 10(4):449–455, April 2018.

- [30] Q Wang, R. Schoenlein, L. Peteanu, R. Mathies, and C. Shank. vibrationally coherent photochemistry in the femtosecond primary event of vision. *Science*, 266(5184):422–424, October 1994.
- [31] L. A. Peteanu, R. W. Schoenlein, Q. Wang, R. A. Mathies, and C. V. Shank. The first step in vision occurs in femtoseconds: Complete blue and red spectral studies. *Proceedings of the National Academy of Sciences*, 90(24):11762–11766, December 1993.
- [32] Christoph Schnedermann, Matz Liebel, and Philipp Kukura. Mode-Specificity of vibrationally coherent internal conversion in rhodopsin during the primary visual event. *Journal of the American Chemical Society*, 137(8):2886–2891, March 2015.
- [33] Olga Smitienko, Victor Nadtochenko, Tatiana Feldman, Maria Balatskaya, Ivan Shelaev, Fedor Gostev, Oleg Sarkisov, and Mikhail Ostrovsky. Femtosecond laser spectroscopy of the rhodopsin photochromic reaction: A concept for ultrafast optical molecular switch creation (Ultrafast reversible photoreaction of rhodopsin). *Molecules*, 19(11):18351–18366, November 2014.
- [34] Kristina Kirchberg, Tai-Yang Kim, Sebastian Haase, and Ulrike Alexiev. Functional interaction structures of the photochromic retinal protein rhodopsin. *Photochemical & Photobiological Sciences*, 9(2):226–233, 2010.
- [35] H Kandori, Y Shichida, and T Yoshizawa. Photoisomerization in rhodopsin. *Biochemistry (Moscow)*, 66(11):1197–1209, 2001.
- [36] Yoshinori Shichida and Takefumi Morizumi. Mechanism of G-protein Activation by Rhodopsin†. *Photochemistry and Photobiology*, 83(1):70–75, 2007. eprint: <https://onlinelibrary.wiley.com/doi/10.1562/2006-03-22-IR-854>.
- [37] Krzysztof Palczewski. G protein-Ã¢-coupled receptor rhodopsin. *Annu. Rev. Biochem.*, 75:743–767, 2006.
- [38] Tohru Yoshioka. Physical aspects of medical science. *The Kaohsiung journal of medical sciences*, 28:S26–32, February 2012.
- [39] Bin Shen, Jun Zhang, Hongya Wu, Jianying Wang, Ke Ma, Zheng Li, Xueguang Zhang, Pumin Zhang, and Xingxu Huang. Generation of gene-modified mice via Cas9/RNA-mediated gene targeting. *Cell Research*, 23(5):720–723, May 2013.

- [40] Woong Y. Hwang, Yanfang Fu, Deepak Reyon, Morgan L. Maeder, Shengdar Q. Tsai, Jeffry D. Sander, Randall T. Peterson, J.-R. Joanna Yeh, and J. Keith Joung. Efficient genome editing in zebrafish using a CRISPR-Cas system. *Nature Biotechnology*, 31(3):227–229, March 2013.
- [41] Giulio Cerullo and Sandro De Silvestri. Ultrafast optical parametric amplifiers. *Review of Scientific Instruments*, 74(1):1–18, January 2003.
- [42] Antoine Monmayrant. *Façonnage et caractérisation d’impulsions ultracourtes. Contrôle Cohérent de systèmes simples*. PhD thesis.
- [43] Luigi Bonacina, Jérôme Extermann, Ariana Rondi, Véronique Boutou, and Jean-Pierre Wolf. Multiobjective genetic approach for optimal control of photoinduced processes. *Physical Review A*, 76(2):023408, August 2007.
- [44] Natalia V Kapousta-Bruneau. Effects of sodium pentobarbital on the components of electroretinogram in the isolated rat retina. *Vision research*, 39(21):3498–3512, 1999.
- [45] Frans Vinberg, Alexander V Kolesnikov, and Vladimir J Kefalov. Ex vivo erg analysis of photoreceptors using an in vivo erg system. *Vision research*, 101:108–117, 2014.
- [46] T Michael Redmond, Shirley Yu, Eric Lee, Dean Bok, Duco Hamasaki, Ning Chen, Patrice Goletz, Jian-Xing Ma, Rosalie K Crouch, and Karl Pfeifer. Rpe65 is necessary for production of 11-cis-vitamin a in the retinal visual cycle. *Nature genetics*, 20(4):344–351, 1998.
- [47] S. Remtulla and P. E. Hallett. A schematic eye for the mouse, and comparisons with the rat. *Vision Research*, 25(1):21–31, January 1985.
- [48] Lily Lin and Paul D Sherman. Cleaning data the chauvenet way. *The Proceedings of the SouthEast SAS Users Group*, 2007.
- [49] Bo Lei, Gang Yao, Keqing Zhang, Kurt J Hofeldt, and Bo Chang. Study of rod-and cone-driven oscillatory potentials in mice. *Investigative ophthalmology & visual science*, 47(6):2732–2738, 2006.
- [50] Lillemor Wachtmeister. Oscillatory potentials in the retina: What do they reveal. *Progress in Retinal and Eye Research*, 17(4):485–521, October 1998.

- [51] Grazyna Palczewska, Frans Vinberg, Patrycjusz Stremplewski, Martin P. Bircher, David Salom, Katarzyna Komar, Jianye Zhang, Michele Cascella, Maciej Wojtkowski, Vladimir J. Kefalov, and Krzysztof Palczewski. Human infrared vision is triggered by two-photon chromophore isomerization. *Proceedings of the National Academy of Sciences*, 111(50):E5445–E5454, December 2014.
- [52] Olaf Strauss. *The retinal pigment epithelium, Webvision: The Organization of the Retina and Visual System [Internet]*. 2011.
- [53] Hiroo Imai, Vladimir Kefalov, Keisuke Sakurai, Osamu Chisaka, Yoshiki Ueda, Akishi Onishi, Takefumi Morizumi, Yingbin Fu, Kazuhisa Ichikawa, Kei Nakatani, Yoshihito Honda, Jeannie Chen, King-Wai Yau, and Yoshinori Shichida. Molecular Properties of Rhodopsin and Rod Function. *The Journal of biological chemistry*, 282(9):6677–6684, March 2007.
- [54] Ido Perlman. The Electroretinogram: ERG. In Helga Kolb, Eduardo Fernandez, and Ralph Nelson, editors, *Webvision: The Organization of the Retina and Visual System*. University of Utah Health Sciences Center, Salt Lake City (UT), 1995.
- [55] Govind Nair, Moon Kim, Tsukasa Nagaoka, Darin E Olson, Peter M ThulÀr, Machelle T Pardue, and Timothy Q Duong. Effects of common anesthetics on eye movement and electroretinogram. *Documenta ophthalmologica*, 122(3):163–176, 2011.
- [56] Charles H Brown and Daniel G Green. Rod saturation in b-wave of the rat electroretinogram under two different anesthetics. *Vision research*, 24(1):87–90, 1984.
- [57] Atsushi Mizota and Emiko Adachi-Usami. Effect of body temperature on electroretinogram of mice. *Investigative ophthalmology & visual science*, 43(12):3754–3757, 2002.
- [58] George M Hale and Marvin R Querry. Optical constants of water in the 200-nm to 200-Åm wavelength region. *Applied optics*, 12(3):555–563, 1973.
- [59] Han H na Park, Yureeda Qazi, Christopher Tan, Seema B Jabbar, Yang Cao, Gregor Schmid, and Machelle T Pardue. Assessment of axial length measurements in mouse eyes. *Optometry and Vision Science*, 89(3):296, 2012.

- [60] Doron Meshulach and Yaron Silberberg. Coherent quantum control of multiphoton transitions by shaped ultrashort optical pulses. *Physical Review A*, 60(2):1287–1292, August 1999.
- [61] Yaron Silberberg. Quantum Coherent Control for Nonlinear Spectroscopy and Microscopy. *Annual Review of Physical Chemistry*, 60(1):277–292, May 2009.
- [62] Oliver P. Ernst, David T. Lodowski, Marcus Elstner, Peter Hegemann, Leonid S. Brown, and Hideki Kandori. Microbial and Animal Rhodopsins: Structures, Functions, and Molecular Mechanisms. *Chemical Reviews*, 114(1):126–163, January 2014.
- [63] Keita Sato, Takahiro Yamashita, Hideyo Ohuchi, Atsuko Takeuchi, Hitoshi Gotoh, Katsuhiko Ono, Misao Mizuno, Yasuhisa Mizutani, Sayuri Tomonari, Kazumi Sakai, Yasushi Imamoto, Akimori Wada, and Yoshi-nori Shichida. Opn5L1 is a retinal receptor that behaves as a reverse and self-regenerating photoreceptor. *Nature Communications*, 9(1), December 2018.
- [64] Valentyn I. Prokhorenko, Alexei Halpin, Philip J. M. Johnson, R. J. Dwayne Miller, and Leonid S. Brown. Coherent control of the isomerization of retinal in bacteriorhodopsin in the high intensity regime. *The Journal of Chemical Physics*, 134(8):085105, February 2011.
- [65] MING YAN, D MANOR, G Weng, H CHAOt, L Rothberg, T M Jedju, and R R ALFANO. Ultrafast spectroscopy of the visual pigment rhodopsin. *Proc. Natl. Acad. Sci. USA*, page 4, 1991.
- [66] T Suzuki and R H Callender. Primary photochemistry and photoisomerization of retinal at 77 degrees K in cattle and squid rhodopsins. *Biophysical Journal*, 34(2):261–270, May 1981.
- [67] R R Birge and L M Hubbard. Molecular dynamics of trans-cis isomerization in bathorhodopsin. *Biophysical Journal*, 34(3):517–534, June 1981.
- [68] Hans-Dieter Meyer. INTRODUCTION TO MCTDH. Lecture Notes, 2010.
- [69] Susanne Hahn and Gerhard Stock. Femtosecond secondary emission arising from the nonadiabatic photoisomerization in rhodopsin. *Chemical Physics*, 259(2):297–312, September 2000.

- [70] David J Tannor, Ronnie Kosloff, and Stuart A Rice. Coherent pulse sequence induced control of selectivity of reactions: Exact quantum mechanical calculations. *The Journal of chemical physics*, 85(10):5805–5820, 1986.
- [71] S. L. Palfrey and T. F. Heinz. Coherent interactions in pump–probe absorption measurements: The effect of phase gratings. *Journal of the Optical Society of America B*, 2(4):674, April 1985.
- [72] M. V. Lebedev, O. V. Misochko, T. Dekorsy, and N. Georgiev. On the nature of “coherent artifact”. *Journal of Experimental and Theoretical Physics*, 100(2):272–282, February 2005.
- [73] Elise Blankenship and David T Lodowski. *Rhodopsin purification from dark-adapted bovine retina*, pages 21–38. Springer, 2015.
- [74] David H Sliney, Robert T Wangemann, James K Franks, and Myron L Wolbarsht. Visual sensitivity of the eye to infrared laser radiation. *JOSA*, 66(4):339–341, 1976.
- [75] Valentyn I. Prokhorenko, Andrea M. Nagy, Stephen A. Waschuk, Leonid S. Brown, Robert R. Birge, and R. J. Dwayne Miller. Coherent Control of Retinal Isomerization in Bacteriorhodopsin. *Science*, 313(5791):1257–1261, September 2006.